Devising New Biomedical Imaging Applications for Metallodrugs based on an Improved Understanding of their Electronic and Magnetic Properties



A Thesis submitted for the Degree of

Doctor of Philosophy

Katherine Rose Fisher

Linacre College

University of Oxford

Hilary Term 2020

Abstract

"Devising New Biomedical Imaging Applications for Metallodrugs based on an Improved Understanding of their Electronic and Magnetic Properties"

Katherine Rose Fisher, Linacre College, University of Oxford

DPhil. Thesis, Hilary Term 2020

Ligand field anisotropy plays a key role in defining the spectroscopic properties of lanthanide complexes. Changes to the local ligand field can have profound consequences for the NMR, luminescence and EPR properties of lanthanide ions with inherent anisotropy. In this project ligand field effects are shown to be significant for even Gd(III) complexes, where the ground state of the free ion has an isotropic electron distribution. In these systems, changes to the ligand field and the axial donor are shown to have dramatic effects on the form of the EPR spectrum. These can be rationalized through considering the donor set. A number of EPR techniques were used to characterize the systems: CW EPR and pulsed PEANUT measurements can be correlated with the splitting of the M_s states within the ^8S ground state of Gd(III).

These effects can also be seen for systems with broken symmetry and these variations, with relatively small changes to the local field, can provide useful information and aid in the development of new contrast media. There are also potential further applications for electron polarization agents for DNP MRI. This potential was explored using CW EPR of polymetallic lanthanide complexes and subsequent DNP NMR experiments. Whilst build-up of hyperpolarization could be observed, further development of these complexes is needed in order to surpass the current "gold-standard" and be translated for clinical practice.

Acknowledgements

I would firstly like to thank Stephen Faulkner for his kindness, encouragement and patience throughout this project. I could not have asked for a better supervisor. I will remember much of your wise advice for the rest of my life.

I would like to thank Alan Kenwright who originally embarked with me on this journey. Alan inspired the projects beginnings and it continued to grow until it became my DPhil. so I am very grateful.

A big thank you goes to Gabriel Moise, Alice Bowen, Will Myers and Chris Timmel for their assistance with the EPR and for the use of the CAESR facilities. I knew nothing about EPR and relatively little about MATLAB® when I started this project, so I am indebted for all their patient help and teaching.

I would like to thank Damian Tyler, Jack Miller and John Myers for aiding me with the DNP part of the project. Thank you for your persistence when things would not work and for encouraging me so much. I am so glad I actually got to do these experiments in the end!

Gratitude goes to Nick Rees for his help with the NMR and the amusing T-shirts. Also a big thank to Victor Mikhailov for his help with MALDI.

I would also like to thank the Faulkner group, both past and present, for putting up with me over the years. You are all legends and I consider you my friends as well as my colleagues. A particular thanks goes to Alex, Grace, Georgie, Laura and Debbie for

encouraging me when things have been difficult. Also, to Carlson and James for their contribution with the luminescence and Dynafit®.

I want to thank Catherine Walter and Jane Hoverd at Linacre College for their support throughout my DPhil. and for listening to me when I have really needed it.

My appreciation goes to Peter Jezzard for all his support and the amazing ONBI CDT cohort. The first year was an incredible experience and I am so grateful to have been part of the group.

Thank you to my friends who have been a great source of joy in my life and have cheered me on through the hard times: Tammy, Vaanu, Hanna, Tasha, Anna, Lozi, Sian, Hannah, Wilfride, Nkosi, Bryony, Ellie, Rachel, Alex, Thelma, Peter, Tom, Rosie...

I want to thank my family including my sister Rosie, my mum who I grow closer to every day and to Darren. Thank you for always picking me up. Also to my nana and grandad who nurtured my love of science. I remember trying to make "concoctions" in my nana's kitchen as a toddler and her telling me they were beautiful. Maybe it was this encouragement that eventually caused me to become a chemist. I will always remember trying to teach grandad, who had little education as a boy, some of the quantum chemistry behind EPR to help me in turn learn it. I love them both very much.

Thank you Matthew for staying with me and supporting me through one of the darkest times of my life. Thank you for your constant love and for always challenging me to be best person I can be. I could not have done this DPhil. without you. I love you so much.

The Lord God has been with me every step of the way. Thank you for never leaving me.

Abbreviations

a.u.	arbitrary units
cyclen	1,4,7,10-tetracyclodecane
CW	continuous wave
DCM	dichloromethane
DMF	dimethylformamide
DMSO	dimethylsulfoxide
DNP	dynamic nuclear polarization
DO3A	1,4,7,10-tetraazacyclododecane-1,4,7-triacetic acid
DOTA	1,4,7,10-tetraazacyclododecane-1,4,7,10-tetraacetic acid
DQ	double quantum
EPR	electron paramagnetic resonance
Eq	equivalents
ESMS	electrospray mass spectrometry
Et_3N	triethylamine
EtOAC	ethyl acetate
HRMS	high resolution mass spectrometry
LCMS	liquid chromatography mass spectrometry
Ln	lanthanide
MALDI	matrix-assisted laser desorption and ionisation
MAS	magic angle spinning
MeCN	acetonitrile

MeOH	methanol
MRI	magnetic resonance imaging
OAc	acetate
PEANUT	phase-inverted echo-amplitude detected nutation
SAP	square anti-prism
SQ	single quantum
T_1	longitudinal relaxation time
T_2	transverse relaxation time
TBAF	tetra-n-butylammonium fluoride
^{t}Bu	tert-butyl
TFA	trifluoroacetic acid
TLC	thin layer chromatography
TMF	2,2,5,5,-tetramethyltetrahydrofuran
t_R	retention time
TSAP	twisted square anti-prism
SNR	signal-to-noise ratio
ZQ	zero quantum

Table of contents

Abstract i

Acknowledgements ii

Abbreviations iv

1 Introduction 1

1.1 An Introduction to Lanthanide Chemistry 1

1.1.1 General Context 1

1.1.2 Lanthanide Ions 1

1.1.3 Stability of Lanthanide Complexes 3

1.1.4 SAP and TSAP Isomerisation 6

1.1.5 Lanthanide Luminescence 7

1.1.6 NMR of Lanthanide Complexes 11

1.1.7 Lanthanide Anisotropy 13

1.2 An Introduction to MRI Contrast Agents 15

1.2.1 An Introduction to Medical Imaging 15

1.2.2 An Introduction to MRI 16

1.2.3 The Use of Gadolinium(III) Contrast Agents 17

1.3 An Introduction to DNP MRI 19

1.3.1 An Essential Development for Cancer Imaging 19

1.3.2 The Basics of DNP MRI 20

1.3.3 Mechanisms by which DNP Occurs 21

1.3.3.1 The Overhauser Effect 21

1.3.3.2 The Solid Effect 22

1.3.3.3 The Cross Effect 23

1.3.3.4 Thermal Mixing 25

1.4 An Introduction to EPR 25

1.4.1 Electron Spin 25

1.4.2 The Zeeman Effect 26

1.4.3 The *g*-value 27

1.4.4 Ligand Field Splitting Parameters 29

1.4.5 EPR of Gadolinium(IIII) 30
1.5 Project Aims 33
1.6 References 35
2 Synthesis of Lanthanide Complexes 39
2.1 General Introduction 39
2.2 Synthesis of Mono Gadolinium(III) Complexes 42
2.2.1 Synthesis of Gd.DOTAMPh 42
2.2.2 Synthesis of Gd.pDO3A 46
2.3 Synthesis of Bimetallic Complexes 51
2.3.1 Synthesis of GdGd.p2DO3A 51
2.4 References 57
3 Exploring Zero-Field Splitting upon Changing Axial Donor Ligand 58
3.1 Introduction 58
3.2 Experimental Conditions for CW EPR 59
3.3 Computational Analysis of Results 60
3.4 X-band Spectra 63
3.4.1 Gd.DOTAMPh 63
3.4.2 Benzylamine.Gd.DOTAMPh 64
3.4.3 Phenol.Gd.DOTAMPh 65
3.4.4 Benzoic acid.Gd.DOTAMPh 66
3.4.5 Benzylalcohol.Gd.DOTAMPh 67
3.4.6 Aniline.Gd.DOTAMPh 68
3.4.7 DMSO.Gd.DOTAMPh 69
3.4.8 Fluoride.Gd.DOTAMPh 70
3.5 Q-band Spectra 71
3.5.1 Gd.DOTAMPh 71
3.5.2 Benzylamine.Gd.DOTAMPh 72
3.5.3 Phenol.Gd.DOTAMPh 73
3.5.4 Benzoic acid.Gd.DOTAMPh 74
3.5.5 Benzylalcohol.Gd.DOTAMPh 75
3.5.6 Aniline.Gd.DOTAMPh 76
3.5.7 DMSO.Gd.DOTAMPh 77

3.5.8 Fluoride.Gd.DOTAMPh 78
3.6 Summary of Spectra 79
3.7 Global Fitting 80
3.8 Discussion of Global Fitting 82
3.9 The Contribution of Different Transitions between M_s States 83
3.10 The PEANUT Experiment 86
3.11 PEANUT and Pulsed Experiments 87
3.12 Luminescence Binding Studies 90
3.13 Conclusion to Chapter 93
3.14 References 94
4 Using EPR to Explore Broken Symmetry Systems 95
4.1 Introduction 95
4.2 Experimental Conditions for CW EPR 96
4.3 Computational Analysis of Results 96
4.4 One Component X-band Fitting 98
4.4.1 Gd.pDO3A 98
4.4.2 Benzylamine.Gd.pDO3A 99
4.4.3 Phenol.Gd.pDO3A 100
4.4.4 DMSO.Gd.pDO3A 101
4.5 One Component Q-band Fitting 102
4.5.1 Gd.pDO3A 102
4.5.2 Benzylamine.Gd.pDO3A 103
4.5.3 Phenol.Gd.pDO3A 104
4.5.4 DMSO.Gd.pDO3A 105
4.6 Summary of One Component Model 106
4.7 Global Fitting of One Component Model 107
4.8 Discussion of Global Fitting for One Component Model 107
4.9 Two Component X-band Fitting 108
4.9.1 Gd.pDO3A 108
4.9.2 Benzylamine.Gd.pDO3A 109
4.9.3 Phenol.Gd.pDO3A 110
4.9.4 DMSO.Gd.pDO3A 111

4.10 Two Component Q-band Fitting 112
4.10.1 Gd.pDO3A 112
4.10.2 Benzylamine.Gd.pDO3A 113
4.10.3 Phenol.Gd.pDO3A 114
4.10.4 DMSO.Gd.pDO3A 115
4.11 Summary Two Component Model 116
4.12 Global Fitting of Two Component Model 117
4.13 Discussion of Global Fitting for Two Component Model 119
4.14 Conclusion to Chapter 119
4.15 References 120
5 Using EPR to Explore Polymetallic Complexes and DNP NMR Study 121
5.1 Introduction 121
5.2 Experimental Conditions for CW EPR 123
5.3 Computational Analysis of Results 123
5.4 X-band Spectra 124
5.4.1 GdGd.p2DO3A 124
5.4.2 Resorcinol.GdGd.p2DO3A 125
5.4.3 Catechol.GdGd.p2DO3A 126
5.4.4 Ascorbic acid.GdGd.p2DO3A 127
5.5 Q-band Spectra 128
5.5.1 GdGd.p2DO3A 128
5.5.2 Resorcinol.GdGd.p2DO3A 129
5.5.3 Catechol.GdGd.p2DO3A 130
5.5.4 Ascorbic acid.GdGd.p2DO3A 131
5.6 Summary of Spectra 132
5.7 Global Fitting 133
5.8 Discussion of Global Fitting Results 134
5.9 CW EPR Conclusions 134
5.10 ^{13}C Hyperpolarisation Studies 135
5.11 Discussion of ^{13}C Hyperpolarisation Results 138
5.12 Conclusion to Chapter 139
5.13 References 140

6 Conclusions and Future Work 141
6.1 Thesis Conclusions 141
6.2 Future Work 143
7 Experimental 145
7.1 General Experiment Information 145
7.2 Characterisation of Compounds 146
7.3 Luminescence Titrations 158
7.3.1 Methodology of titrations 158
7.3.2 Dynafit® Scripting 159
7.3.3 Example of Dynafit® Script 159
7.4 References 160

1 Introduction

1.1 An Introduction to Lanthanide Chemistry

1.1.1 General Context

The lanthanides can be found in the first row of the *f*-block in the Periodic Table, located between the *s*-block and the transition metals (*d*-block). From lanthanum to lutetium, the lanthanides have become essential in modern day applications such as medical imaging, microscopy and therapeutic applications. [1] Lanthanides are an ideal chemical species for optical imaging and many are also used in contrast agents and radiotracers. [2, 3] Other applications include their uses in superconductors and lasers. Whilst lanthanides are known more commonly as the rare earth elements, this is misleading with elements such lanthanum, cerium and neodymium being relatively abundant. [4] The concept of the lanthanides rarity instead originates from the difficulty in separating lanthanides from one another. What makes the lanthanides' so valuable is their unique chemical properties which are exploited in their applications.

1.1.2 Lanthanide Ions

Lanthanides have 4*f* valence orbitals with the common electronic configuration of $[Xe]4f^n6s^2$, where n is an integer from 1 to 15. The exceptions to this rule are lanthanum,

cerium, gadolinium and lutetium which have an electronic configuration of [Xe]4f^{n-1}5$d^1$6s^2. Lanthanides tend to form trivalent cations, Ln(III), with an electronic configuration of [Xe]4f^{n-1}. It is also possible for a few lanthanides such as europium and cerium to form species such as Eu(II) and Ce(IV) due to their favourable electronic configurations, [Xe]4f^7 and [Xe], respectively.

The valence electrons of Ln(III) ions are in 4*f* orbitals which are 'core-like' and 'contracted' due the lack of a radial node as part of their radial distribution function, whilst the 6*s*, 6*p* and 5*d* subshells of the lanthanides have a large radial expansion. It is the empty 6*s*, 6*p* and 5*d* that tend to take part in bonding. The shielding of the 4*f* valence orbitals by the 6*s*, 6*p* and 5*d* leads to lanthanides being shielded from their coordination environment **Figure 1.1**. Consequently, the lanthanides tend to form relatively 'hard' trivalent cationic species with complexes that have large coordination numbers greater than 6, typically 8 or 9 and in some cases even reaching 12. [5]

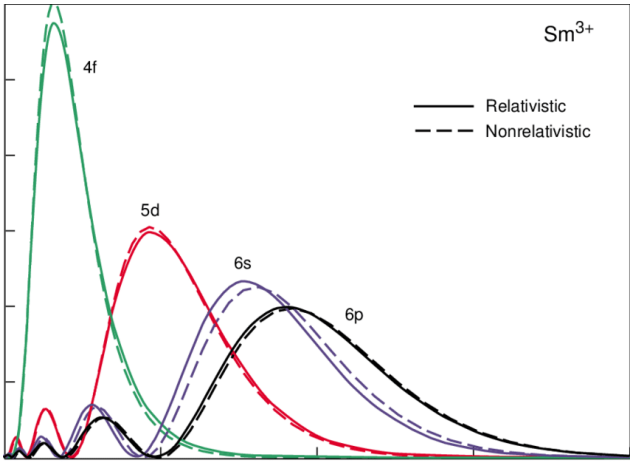

Figure 1.1: The radial probability of finding an electron at a distance r from the nucleus is shown for the valence 4*f*, 5*d*, 6*s*, and 6*p* orbitals of Sm(III). The 4*f* orbitals are clearly the most contracted and do not possess a radial node unlike the other orbitals shown. Citation: Clark, David. (2000). The Chemical Complexities of Plutonium. Los Alamos Sci. 26.

Bonding within lanthanide complexes is presumed to be ionic with negligible ligand field perturbation of the 4*f* valence orbitals. As a result, it is generally assumed that coordination environment of the lanthanide ion has little effect on the properties of the molecule. If correct, this would include magnetic anisotropy and therefore spectroscopy which leads us to imaging applications. If interactions are purely ionic in nature, then the electronic and magnetic properties of lanthanide complexes can be crudely predicted depending on what the identity of the lanthanide ion is.

The ionic nature of the lanthanide ions, despite their high atomic number, is due to the well-known lanthanide contraction where the trivalent cation is much smaller consistently across the 4*f* row than would otherwise be expected. However, the actual nature of bonding within lanthanide complexes is far more complex than this and the coordination environment can contribute to properties such as anisotropy by ligand field perturbation. [6] This, in turn, can have significant influence on spectroscopy and on applications such as imaging. [7] The exploration of ligand field perturbation in lanthanide complexes and its importance for applications will be one of the aims of this thesis.

1.1.3 Stability of Lanthanide Complexes

Lanthanide ions are moderately toxic and can cause conditions such as pneumoconiosis in the body. [8] Lanthanide ions can also biologically mimic Ca(II) due to their radii being of a comparable size thus binding to Ca(II) receptors *in vivo*. As a result, it is not

appropriate to directly inject Ln(III) species into the body such as Gd(III), which is ideal for creating contrast in MRI and discussed in **Section 1.2.3** in this thesis.

To be used in medical applications *in vivo*, lanthanide ions need to be contained within an environment that renders them non-toxic. This typically requires them to be tightly bound to a multidentate ligand or a macrocycle to form a non-toxic complex which must have both high thermodynamic and kinetic stability.

As previously discussed, the bonds within Ln(III) species are highly ionic in nature and simple complexes involving multiple monodentate ligands tend to be unstable relative to the dissolved ion. The chelate effect can be used to produce more stable complexes. The chelate effect is the enhanced affinity of chelating linear multidentate ligands for a metal ion compared to the affinity of a collection of similar non-chelating (monodentate) ligands for the same metal. Rigid macrocyclic ligands are even more stable still which is due to the macrocyclic effect **Figure 1.2**.

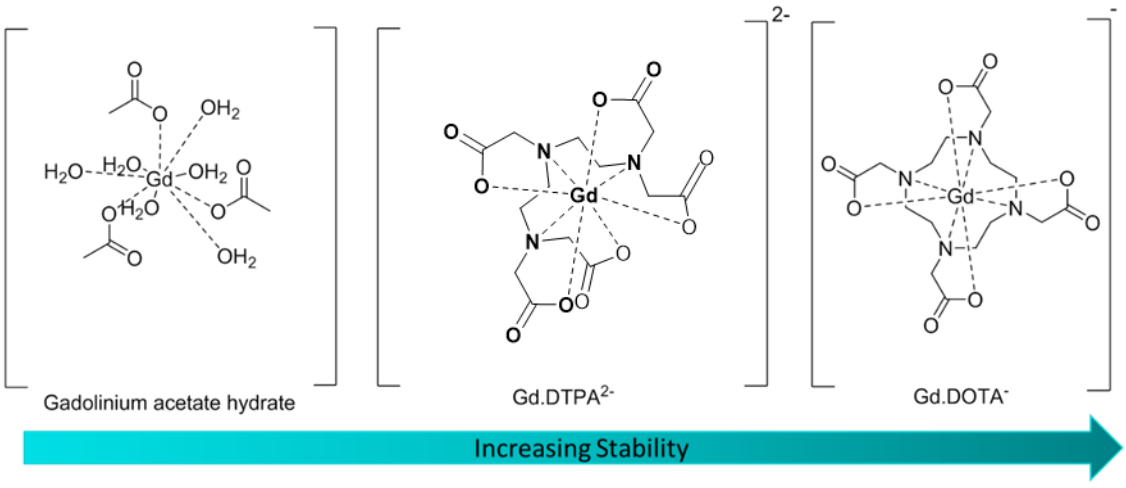

Figure 1.2: Schematic showing how stability increasing from monodentate ligands binding to multidentate chelate binding to macrocyclic binding of analogous species.

$Gd.DOTA^-$ has far greater stability than complexes like $Gd.DTPA^{2-}$ primarily due to higher kinetic stability. Macrocyclic ligands have been shown to be far less labile and have a higher safety record than linear complexes. [9, 10] There have been many macrocyclic chelates developed to make Ln(III) ions biocompatible and render them non-toxic for use *in vivo*. Some literature compounds published include those such as DOTA, DO3A and DO3AM **Figure 1.3** which are three of the most common in use. [11] $Gd.DOTA^-$ is known for its very high stability and is used under the brand name of DOTAREM® worldwide as a contrast agent in magnetic resonance imaging (MRI). [12]

Alternatively, complexes such as DO3A and DO3AM are often used as building blocks to introduce a different fourth arm to the complex with a specific purpose. This appended arm could be an aromatic ligand used to harvest light which is discussed in detail in **Section 1.1.5** of this thesis.

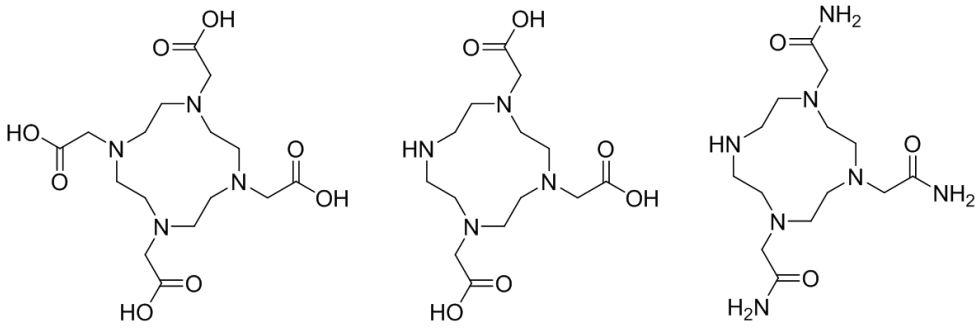

Figure 1.3: Common macrocycles used for binding Ln(III) ions to form stable complexes. DOTA is to the left, DO3A is in the centre and DO3AM is to the right.

1.1.4 SAP and TSAP Isomerisation

Lanthanide DOTA complexes, as with many other macrocyclic lanthanide complexes, have different possible conformations that can be adopted in solution **Figure 1.4**. The two different species can be distinguished by NMR; the square antiprism (SAP) and the twisted square antiprism (TSAP). Interconversion can happen between the diastereomers via a ring inversion or arm rotation. Two steps of an arm rotation followed by a subsequent ring inversion or *vice versa* will produce the other enantiomer. For the two lanthanides that are the main source of study for this thesis, europium and gadolinium, there is a preference for the SAP geometry for the DOTA complex. [13] For macrocycles that have bulky tetra-amide arms the preference is also shifted towards the SAP isomer but different solvents can also have a large impact on the ratio of SAP to TSAP isomers, for example, MeCN can increase the amount of the TSAP isomer. [14]

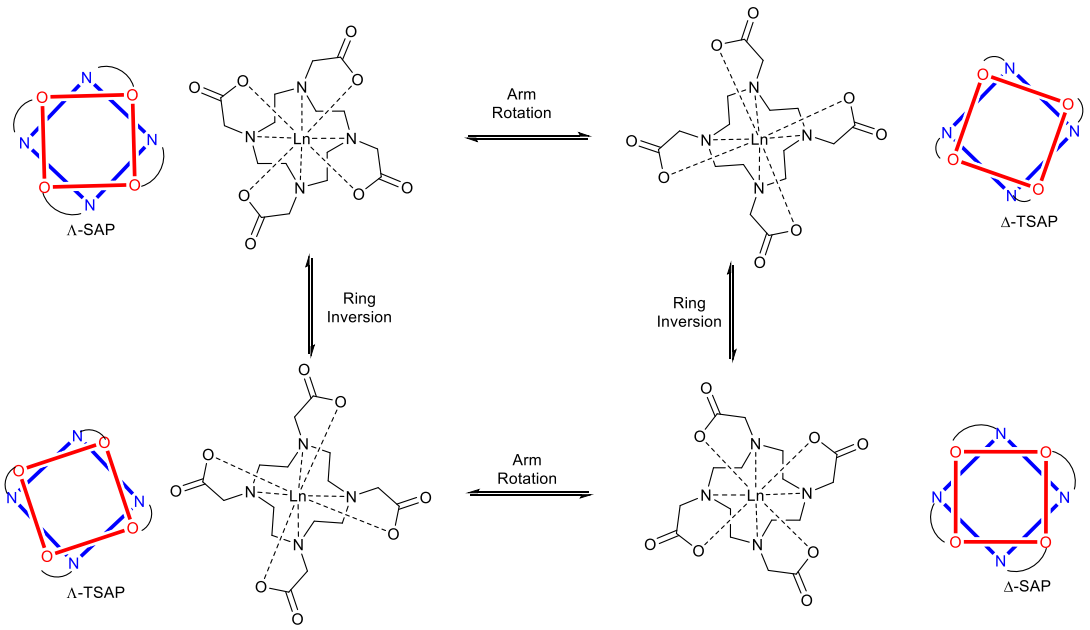

Figure 1.4: Schematic of the four different isomers of Ln.DOTA arising from the mutual inversion of chirality of the macrocycle or the acetate arms.

1.1.5 Lanthanide Luminescence

Lanthanides have long lived luminescence lifetimes of microseconds to milliseconds due to their 4*f*–4*f* absorptions which are technically parity-forbidden but can be overcome due to relatively strong spin-orbit coupling as lanthanides have high atomic numbers and therefore many electrons. [15] All Ln(III) ions except lutetium(III) and lanthanum(III) are luminescent. The forbidden nature of the transitions in lanthanide complexes results in them having low molar extinction coefficients ($\varepsilon < 1$ M^{-1} cm^{-1}) thus, rendering pale coloured aqueous solutions. [16, 17] The luminescence spectra of trivalent lanthanide ions and their complexes show sharp, narrow bands which are used as evidence for their ionic nature **Figure 1.5**. Complexes such as Eu(III) and Tb(III) have visible emission.

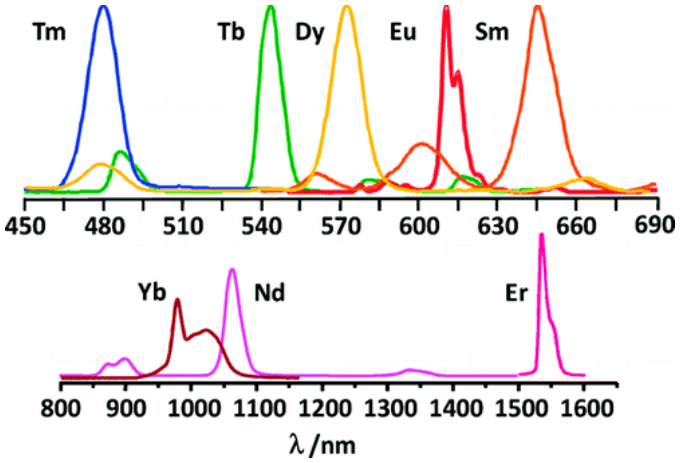

Figure 1.5: Luminscence of lanthanide tris(β-diketonates) species (Caption taken with permission for academic purposes from J.-C. G. Bunzli and C. Piguet, Chem. Soc. Rev., vol. 34, pp. 1048-1077, 2005.)

The long luminescence lifetimes make lanthanide complexes ideal for imaging applications due to their slow relaxation back to the ground state. On the other hand, the weak molar extinction coefficient is not desirable. This is due to the formally forbidden initial excitation of the lanthanide ion within a complex. Lanthanide complexes often

need to be sensitised and usually the incorporation of a chromophore “antenna” into the complex close to the metal centre to harvest light is necessary, as shown in **Figure 1.6**. [11]

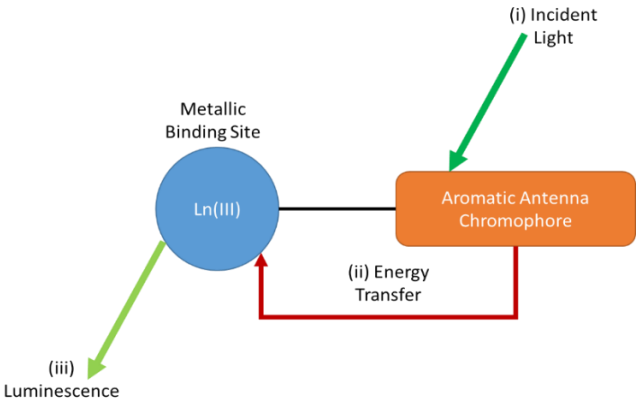

Figure 1.6: Schematic showing how introduction of an aromatic chromophore helps lanthanide complex luminescence.

A basic schematic Jablonski diagram is shown in **Figure 1.7**. The actual process is far more complex, as different types of energy transfer are possible from the antenna to the lanthanide ion.

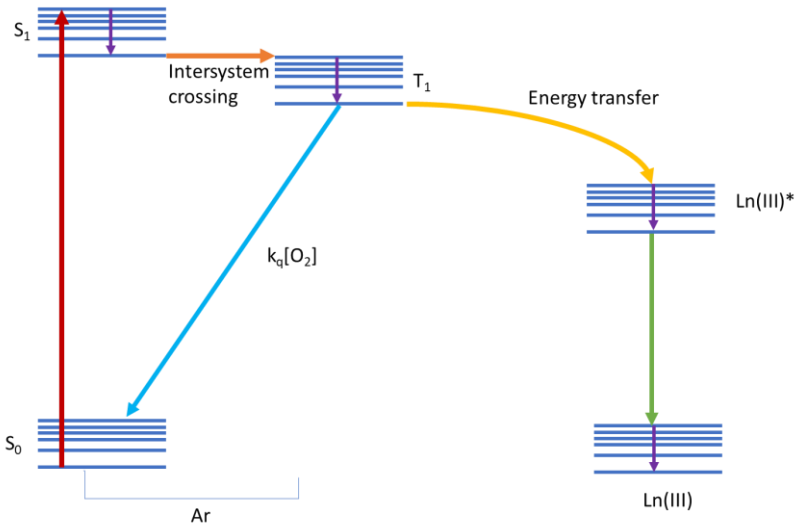

Figure 1.7: Schematic Jablonski diagram of luminescence in lanthanide complexes containing an antenna appended aromatic chromophore.

The two most common types of energy transfer possible are Dexter and Förster electron transfer **Figure 1.8**.

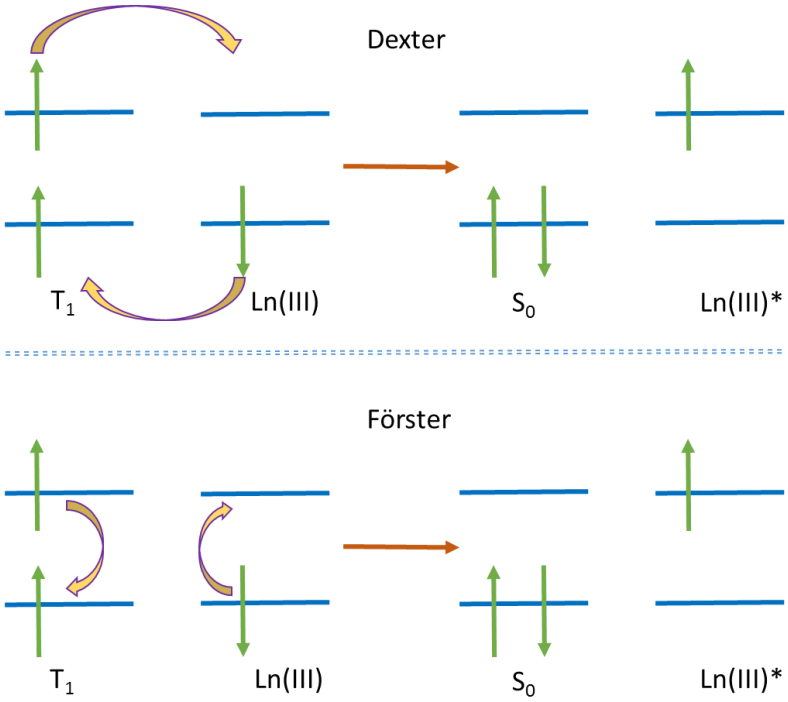

Figure 1.8: Schematic of the Dexter and Förster Energy Transfer Mechanisms.

The Dexter mechanism is a through-bond mechanism that involves the exchange of two electrons with an e^{-r} dependency. In order for this to occur, there must be an overlap of donor and acceptor wavefunctions. [18, 19]

The Förster energy transfer mechanism operates through space and has an r^{-6} dependency. It involves a dipole-dipole through space coupling mechanism and can therefore occur over greater distances of approximately 10 Å. The Förster mechanism relies on the spectral overlap of the acceptor and the donor. [19, 20]

The antenna is essentially an appended aromatic chromophore, so the choice is limited by the high energy emissive state of the lanthanide. [21] Lanthanides which emit light in

the near IR have much lower emissive state energies. There are many examples of a large range of sensitizing chromophores that can be used **Figure 1.9**.

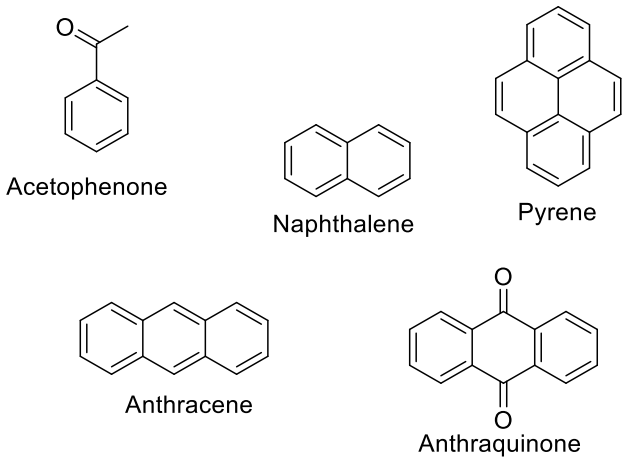

Figure 1.9: Examples of some common aromatic chromophores suitable to be appended to lanthanide complexes to help aid luminescence.

Lifetimes are much shorter, and quantum yields lower than expected for the appended complexes than expected due to quenching with other species such as water. This is caused by the vibrational oscillation of the O-H bonds. Quenching can be decreased and is much less of a problem for deuterated solvents as the O-D oscillation is less problematic. Lifetimes are therefore, longer in deuterated solvent and Horrocks' equation uses this information to calculate the hydration number which is how many solvent molecules are bound in the inner sphere of the complex, where A and B are constants (lanthanide-specific correction factors) and τ is referring to lifetime **Equation 1.1**. [22]

$$q = A\,(\,{\tau_{H2O}}^{-1} - {\tau_{D2O}}^{-1} - \mathrm{B}) \qquad \textit{Equation 1.1}$$

Lanthanide complexes are incredibly useful in biological imaging. Since the lifetimes of lanthanide complexes are long compared to the autofluorescence of background

biomaterial, the switching on of the detector can be delayed so most of the biomaterial has already relaxed back to the ground state which is almost completely non-emissive. The detector can then be switched on and the remaining signal is now almost completely dominated by that of the lanthanide complex **Figure 1.10**. [21]

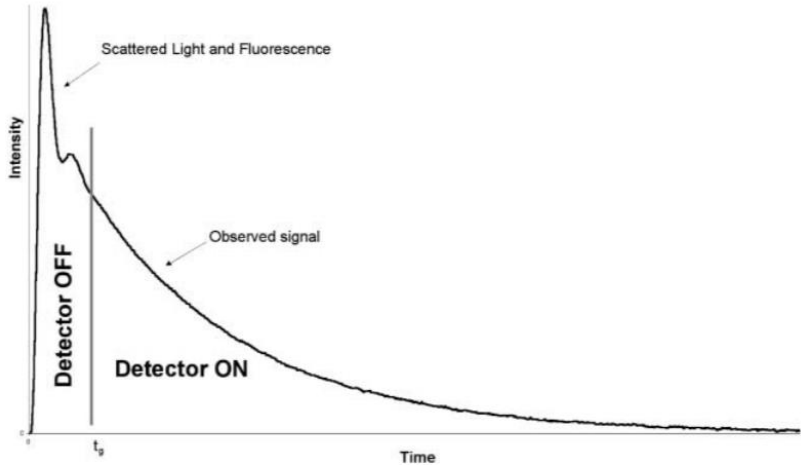

Figure 1.10: Schematic showing time-gated rejection of stray light and fluorescence. Citation: Applied Spectroscopy Reviews, 40: 1–31, 2005.

1.1.6 NMR of lanthanide Complexes

Due to the large number of unpaired electrons in certain lanthanide complexes, a large amount of paramagnetism is created which in turn complicates their NMR spectra. Effects include a wide range in chemical shifts and broadened signals. [23] Paramagnetism leads to shortened relaxation times (T_1) and as a result the rate of spectral acquisition needs to be high.

It is not usually readily possible to take an NMR spectrum of complexes containing Gd(III) using standard NMR techniques. This is because all the 4*f*-subshells are half-

filled, creating the maximum amount of paramagnetism possible, in addition to a large magnetic moment. As a result, the acquisition times are too high as the T_1 relaxation time is too short to readily obtain spectra. A shortening of the T_2 relaxation time also gives rise to line broadening.

Two mechanisms are used to describe how the ^{1}H NMR chemical shift changes for NMR active nuclei in complexes where a lanthanide is bound compared to the unbound complex. These are known as contact shifts and pseudocontact shifts. One effect can be far more dominant than the other though both can operate simultaneously. Contact shifts are essentially responsible for potential hyperfine couplings in EPR spectra. They are the result of the spin polarization transfer from the unpaired electrons in the paramagnetic species to other NMR active nuclei within the molecule.

Lanthanides can experience both contact (through bond) and pseudo-contact (through space) shifts effects. The overall effect due to the lanthanide is known as the lanthanide induced shift (LIS). What is by far the more dominant interaction of interest is the pseudocontact shift for lanthanide species. This is dependent on the magnetic field generated from the Ln(III) ion at the center of the complex.

This concept was explored by Bleaney who was able to describe the change in pseudocontact shift based on a few factors including the geometric coordinates relative to the principal magnetic axis that goes through the central lanthanide ion and the axial and rhombohedral magnetic susceptibility tensor of the compound as described in **Equation 1.2** and **Equation 1.3** where polar coordinates are used as an alternative.

$$\delta_p(x,y,z) = \frac{1}{12\pi r^3}\left[\chi_{ax}\,\frac{2z^2-x^2-y^2}{r^2} + \frac{3}{2}\,\chi_{rh}\,\frac{x^2-y^2}{r^2}\right] \qquad \textit{Equation 1.2}$$

$$\delta_p(r,\theta,\phi) = \frac{1}{12\pi r^3}[\chi_{ax}(3\cos^2\theta - 1) + \frac{3}{2}\chi_{rh}\sin^2\theta\cos 2\phi] \qquad \textit{Equation 1.3}$$

1.1.7 Lanthanide Anisotropy

Anisotropy refers to how a molecule's magnetic properties change based on direction. This can have an impact on the characteristic of the molecule such as its optical transitions or relaxation behaviour. Even in their ground state, due to the shape of the *f*-orbitals that are occupied, it has been shown that Ln(III) ions have an uneven distribution of electron density which it turn leads to anisotropy **Figure 1.11**. [24] The exceptions are the gadolinium(III) and lutetium(III) free ions as both have the totally symmetric $^8S_{7/2}$ and $^1S_0$ states, respectively. They therefore are isotropic in the ground state due to a perfectly spherical electron distribution.

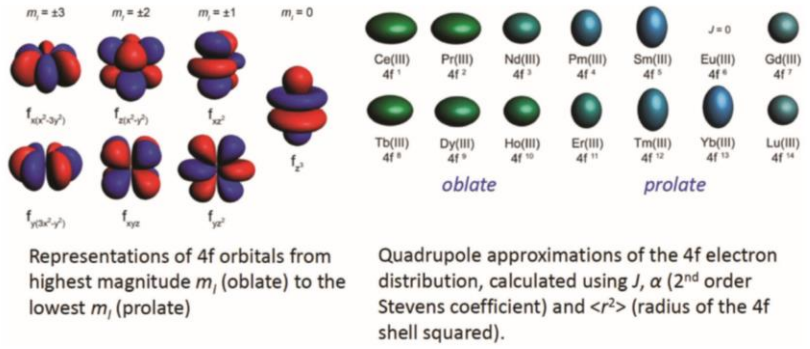

Figure 1.11: Shapes of 4*f* orbitals and 4*f* electron densities; the shape variation of the f electron charge cloud arises from the strong angular dependence of the *f* orbitals. Citation: Dalton Trans., 2016,45, 6782–6800.

Bleaney's theory, as described in **Section 1.1.6**, is essentially a way of describing the anisotropy within lanthanide complexes and has been well used in research studies for decades. [24, 25] **Equation 1.2** and **Equation 1.3** described in **Section 1.1.6** can be

rewritten as **Equation 1.4** where C_J is known as the Bleaney constant which is dependent on the lanthanide at the centre of the complex. The Bleaney constant can be positive or negative in value and therefore shift NMR peaks down or up field as appropriate. The Bleaney constant is calculated using the *J* quantum number and the Landé factor, *g* (**Equation 1.5**). In **Equation 1.4**, θ and φ are the angles between the nucleus under consideration and the principal magnetic axis of the lanthanide ion and μ_B is the Bohr magneton.

$$\delta_p = \frac{C_J {\mu_B}^2}{60(kT)^2}\left[\frac{(3\cos^2\theta - 1)B_0^2}{r^3} + \frac{(\sin^2\theta\cos^2\phi)B_2^2}{r^3}\right] \qquad \textit{Equation 1.4}$$

$$C_J = g^2 J\,(J+1)(2J-1)(2J+3)\langle J|\alpha|J\rangle \qquad \textit{Equation 1.5}$$

The equation also contains B_2^0 and B_2^2 which are the first and second order ligand field splitting parameters, respectively. Bleaney assumed that these were a negligible perturbation in comparison to kT (thermal energy of the system) and this part of the equation could therefore be neglected. This is slowly being proven to be an invalid approximation with some complexes shown to have a crystal field splitting of about 400 cm^{-1} (kT is about 200 cm^{-1} at room temperature). One of the aims of this thesis is to show that there are situations where these parameters cannot be ignored, and that ligand field perturbation does have a substantial impact on the spectroscopy of a complex. Bleaney's theory whilst shown to not be quantitatively accurate for some complexes is still useful as a more qualitative method for analysis to demonstrated that a lanthanide has undergone complexation.

1.2 An Introduction to MRI Contrast Agents

1.2.1 An Introduction to Medical Imaging

Medical imaging has become indispensable in modern day medicine for the diagnosis and monitoring of various diseases such as cancers and heart disease. The most popular techniques include positron emission tomography (PET), computer tomography (CT), single photon emission tomography (SPECT) and magnetic resonance imaging (MRI). Nuclear techniques such as PET and SPECT can also be used to monitor drug distribution, pharmacokinetics and pharmacodynamics. [26]

Each imaging technique has its own advantages and disadvantages with the result that each is appropriately applied to different medical scenarios. Imaging can be used to analyze physiological, anatomical or metabolic change. Whilst not discussed in detail in this thesis, luminescence is an imaging technique that can be used to pinpoint activity within cells and tissues using microscopy. The diversity of medical imaging is summarized below briefly in **Table 1.1**.

Table 1.1: Overview of imaging systems in clinical use. (Weissleder, R.; Pittet, M. J. Nature 2008, 452 (7187), 580-589 and Rudin, M.; Weissleder, R. Nature Reviews Drug Discovery 2003, 2, 123-131.)

	Resolution / mm	Time	Imaging agent	Target	Cost / US$	Main preclinical use
MRI	0.01-0.1	Minutes-hours	Gd, Dy, Iron oxide particles	Anatomical, physiological, molecular	>300,000	Versatile, high soft-tissue contrast
CT	0.05	Minutes	Iodine	Anatomical, physiological	100,000-300,000	Lung imaging, bone imaging
PET	1-2	Minutes-hours	^{18}F, ^{11}C, 15O	Physiological, molecular	>300,000	Versatile, many tracers
SPECT	1-2	Minutes-hours	^{99m}Tc, ^{111}In chelates	Physiological, molecular	100,000-300,000	Antibodies, peptides

1.2.2 An Introduction to MRI

Since commercial MRI became available in 1983, around 20,000 MRI systems have been installed worldwide. [27] Except for the problem of patient motion, MRI offers high soft-tissue contrast with excellent resolution images primarily used for assessing brain disease, spinal disorders, angiography, cardiac function and musculoskeletal damage. [28] MRI, whilst expensive, is still a very versatile technique.

MRI uses the NMR signal from protons (^{1}H) in water molecules. The contrast comes from different tissues, where the environment and quantity of water will vary enabling an image to be produced. Like all magnetic resonance techniques, MRI has low sensitivity but is made viable due to the high abundance of water molecules within the body. Whilst nuclear magnetic resonance (NMR) can use other nuclei for chemical analysis, due to the lack of other naturally occurring NMR active isotopes in the body (such as ^{13}C nuclei within biological compounds) it is not feasible to use standard MRI to measure metabolism.

MRI works by first aligning the ^{1}H nuclei in water with or against the magnetic field of the MRI scanner which is known as the B_0 field. ^{1}H has a nuclear spin of $I = ½$ and although 100% of the nuclei in water are NMR active the difference population of in α and β spin states is still very small. This explains the low sensitivity of NMR generally. The NMR signal can be increased by using a stronger B_0 field which will enlarge the energy difference between the α and β spin states and therefore alter the population difference according to the Boltzmann distribution (**Equation 1.6**).

$$\frac{p_i}{p_j} = e^{\frac{\varepsilon_j - \varepsilon_i}{kT}}$$ *Equation 1.6*

The spin active nuclei align parallel or anti-parallel to the B_0 field. The spins are then perturbed by applying magnetic fields that are typically perpendicular to the B_0 field, this is known as the B_1 field and most modern methods do this using pulse sequences. The nuclei then take varying amounts of time to relax back to the ground state. The time taken for relaxation is measured and used to form an image.

There are three types of image that can commonly be obtained using MRI. A T_1 weighted image which measures the longitudinal relaxation time of the protons, essentially measuring how often an experiment can be repeated. A T_2 experiment on the other hand, measures how the different nuclei become out of phase with each other and how long this takes to return to equilibrium, effectively measuring how long it takes for the signal to diminish. The final type of image that can be taken is a proton density image which simply looks at the number of protons present in different tissues.

1.2.3 The Use of Gadolinium(III) Contrast Agents

Both T_1 and T_2 can be affected by lanthanide contrast agents. However, it is T_1 contrast agents that are typically used in clinical medical imaging and will be explained in this section. Gadolinium(III) contrast agents are the most commonly used contrast agents, though some europium(II) agents have been developed for effective use. [29]

Gd(III) contrast agents effectively work due to the complexes' rapid relaxation rate. This is due to its high paramagnetism which leads to a short T_1. Gd(III) complexes can have a coordination number up to nine and most complexes have eight sites occupied. As a result, when the complex is injected *in vivo* water molecules can move into and out of the place of the ninth coordination site. This causes these water molecules' relaxation rate to also increase as a result **Figure 1.12.** Consequently, this changes the contrast within our image due to the altered T_1 of the surrounding water molecules and the variation of this in different tissues.

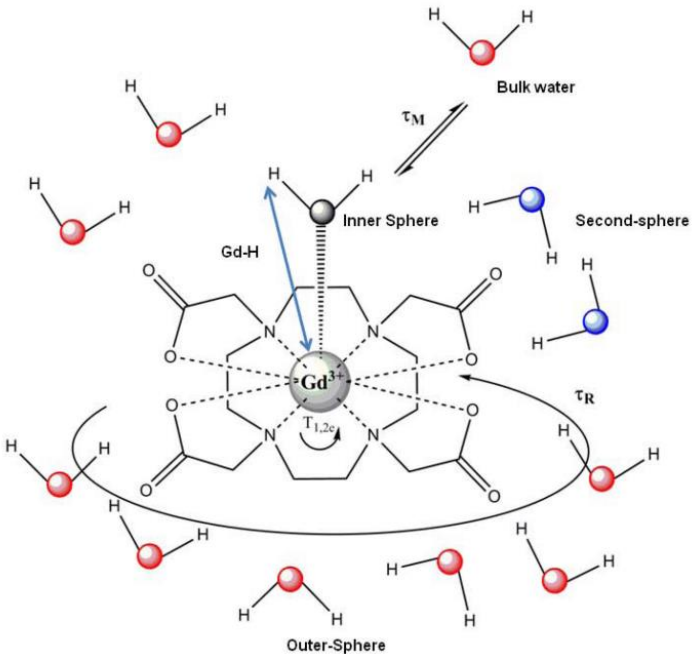

Figure 1.12: Schematic of how Gd(III) Complexes affect relaxation rate of the surrounding water molecules they encounter. Citation: JMRI. 2015; 42 (3): 545-565.

1.3 An Introduction to DNP MRI

1.3.1 An Essential Development for Cancer Imaging

The current "gold-standard" for non-invasively measuring tumour metabolism *in vivo* is PET imaging and less commonly, SPECT imaging. They are used in the diagnosis, staging and follow-up of malignant tumours that allows the quantification of metabolic processes at a molecular level. [30] Both these techniques use radioactive nuclei such as ^{18}F which is a positron emitter with a biological half-life of just under 2 hours (110 minutes). PET-CT and SPECT-CT are currently well established in the clinic giving additional anatomical detail which is often lacking in PET and SPECT. However, CT scans expose patients to further radiation and do not give high spatial resolution due to poor soft tissue contrast. PET-CT also has the limitation that the imaging techniques are performed sequentially, eliminating any temporal correlation. [30, 31]

Another key issue found across all areas of nuclear medicine is the nature of the radioactive nuclei themselves as they emit ionising radiation. As a result, whilst they can help in the treatment of many diseases, they themselves can cause damage to DNA within cells which may potentially lead to cancer. If the patient already has cancer, this is a necessary risk. However, in the case of a healthy patient there is approximately a 1 in 2000 chance of developing cancer after being exposed to techniques such as CT. [32] Although relatively small, this risk is not insignificant and supports research into metabolic imaging not involving ionising radiation.

1.3.2 The Basics of DNP MRI

Observing a change in metabolism in tissues is essential for the diagnosis of diseases such as cancer which is problematic for standard MRI techniques, as previously discussed. Due to the lack of naturally abundant ^{13}C and low sensitivity of MR experiments, it is not feasible to use MRI to measure metabolism. Fortunately, Dynamic Nuclear Polarization (DNP) MR imaging has been developed to increase the amount of nuclear spin polarization in a sample and therefore measurable signal. This occurs via various mechanisms where high polarization of electrons is transferred to the nuclei of the substrate. Hence, the substrate and its downstream metabolites can be observed over time. DNP results in a more intense signal and currently a 10,000 fold increase in signal-to-noise ratio. [32, 33] In current DNP, spins from unpaired electrons in an organic radical that are polarized by a strong magnetic field (3-5 T) at very low temperatures (~1 K) are transferred to ^{13}C nuclei in the substrate by microwaves. The sample, after dissolution, can be injected into an organism in millimolar amounts and an MRI pulse sequence can be used to generate real-time hyperpolarized MRI images to monitor changes in metabolism *in vivo*. The technique is powerful but limited in terms of timescale as the enhanced signal only lasts for about 1 minute. [34]

[1-^{13}C]pyruvate when used as the substrate in DNP MRI can be imaged using hyperpolarized MRI and its metabolic products such as [1-^{13}C]lactate can also be observed. [35] This has proved important in oncological imaging due to the increased rate of glycolysis and lactate fermentation in cancer cells, known as the *Warburg Effect*. [36]

1.3.3 Mechanisms by which DNP Occurs

1.3.3.1 The Overhauser Effect

The Overhauser Effect relies on there being an electron and a nucleus where double quantum (DQ) and zero quantum (ZQ) transitions can occur in addition to the normal single quantum (SQ) transitions that occur for electron paramagnetic resonance (EPR) and nuclear magnetic resonance (NMR) **Figure 1.13**. In the Overhauser effect the electronic SQ transition is saturated and the effect then relies on there being a difference in the relaxation rates of these DQ and ZQ transitions which subsequently occur. The imbalance in these rates leads to an enhancement in nuclear polarization. Solids tend to have a *positive* enhancement with the ZQ transition being dominant. [37] The Overhauser effect occurs if the homogeneous EPR linewidth is approximately equal to the breadth of the EPR signal and is smaller than the nuclear Larmor frequency.

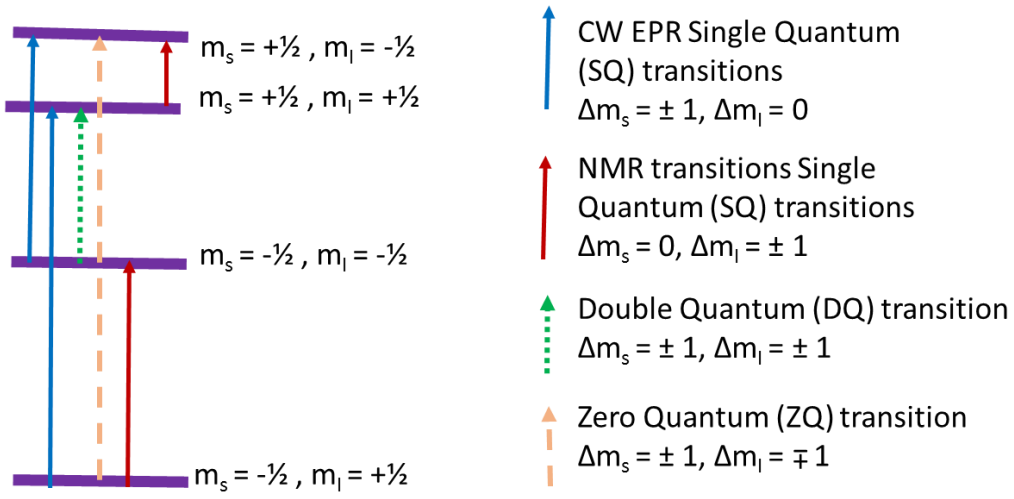

Figure 1.13: Schematic diagram showing the simplest case for different possible quantum transitions in a one electron, one nucleus system with S = I = ½.

1.3.3.2 The Solid Effect

The solid effect is the commonly exploited mechanism that is used in pre-clinical DNP MRI studies. [38] The solid effect occurs if the homogeneous EPR linewidth and inhomogeneous EPR linewidth is greater than the nuclear Larmor frequency. For the solid effect to occur in an $S = I = ½$ single electron and single nucleus species, the nucleus and electron must have something called a pseudo-secular coupling between them which is a coupling that allows the states to be mixed. Microwaves can then drive electron nuclear polarisation transfer. The microwave frequency is equal to the difference between electron Larmor frequency and the nuclear Larmor frequency. When this microwave frequency is applied the double quantum (DQ) transition (or the zero quantum transition (ZQ)) is weakly allowed and is energy conserving. As a result the electron and nuclear polarisations become equalised. This overall will lead to additional nuclear polarisation **Figure 1.14**. [39]

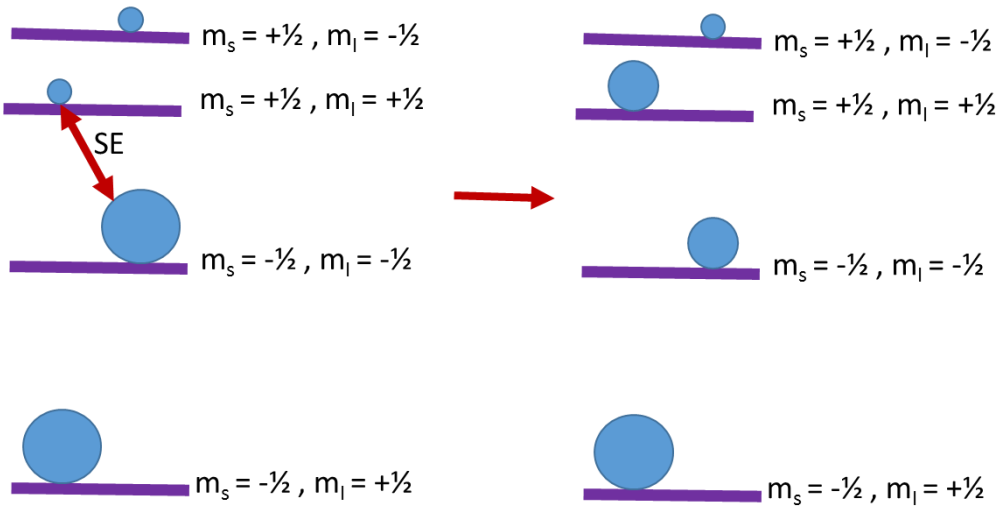

Figure 1.14: A schematic diagram demonstrating the solid effect.

1.3.3.3 Cross Effect

The cross effect is being explored as an improvement on the solid effect for pre-clinical and clinical DNP studies. [40, 41] If the polarisation increase is large enough in impact this could also be a contributing factor for the development of DNP into wider clinical practice.

The cross effect occurs when a species has two radicals present within it. If they are close enough to each other dipolar coupling can occur between the two radical species. If the difference in their electron resonance frequencies is enough that it matches the Larmor frequency of the nucleus that needs to be hyperpolarised then DNP enhancement occurs for that NMR active nucleus **Figure 1.15**. This effect can only occur if the inhomogeneous broadening of the EPR spectra are greater than that of the nuclear Larmor frequency.

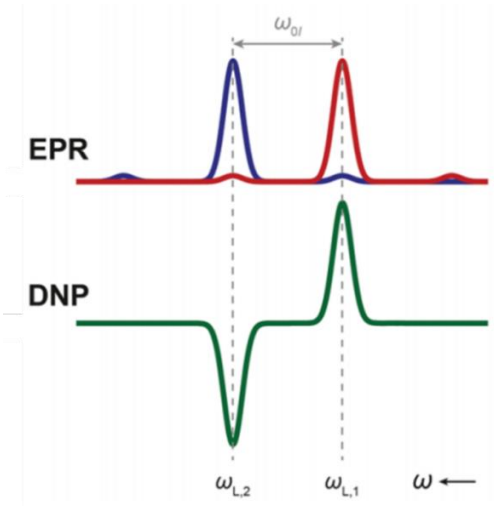

Figure 1.15: Schematic of the cross effect. Figure adapted from Corzilius, Bjorn (2016). Phys Chem. Chem. Phys., 18, 27190-27204.

When magic angle spinning is introduced, the DNP effect becomes even more efficient as the matching condition does not have to be fulfilled at all times for the cross effect to

occur. [40] When magic angle spinning is introduced the two radical centres begin with their individual electronic Larmor frequencies. As the sample rotates one of the radical centres is irradiated by the microwave frequency which causes a partial saturation of the SQ for that centre and therefore there is now a difference in the electron polarisation of the two centres. Then, on continuation of rotation, when the difference in the two radical centres matches that of the Larmor frequency of the nucleus to be polarised there is a partial transfer of electron spin to the nucleus to be polarised. The peaks then cross allowing dipolar coupling and then the process is continued onwards with the ever increasing addition of DNP signal until full thermalization of populations is reached **Figure 1.16**.

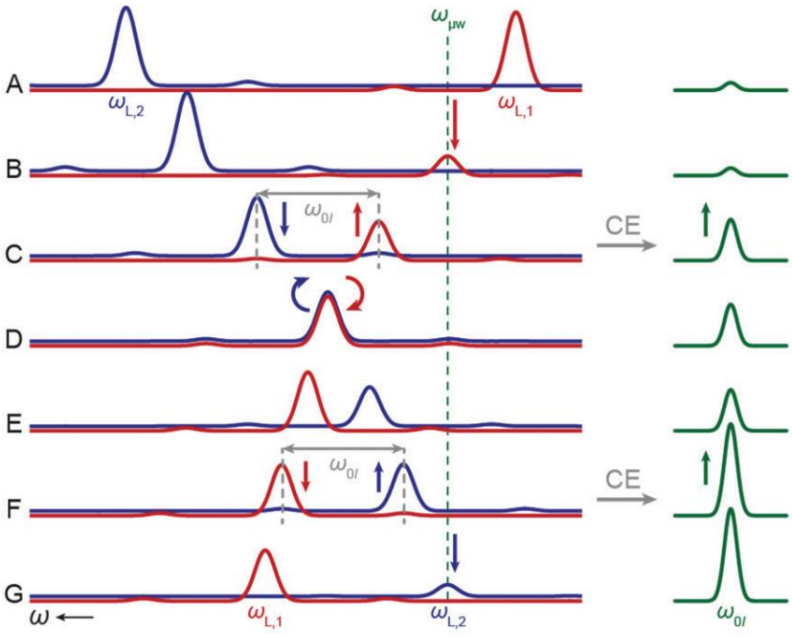

Figure 1.16: Schematic of the cross effect with Magic Angle spinning over time from A to G. The schematic is shown in the rotating frame. Figure adapted from Corzilius, Bjorn (2016). Phys Chem. Chem. Phys., 18, 27190-27204.

1.3.3.4 Thermal Mixing

Thermal mixing is a mechanism that is strongly related to the cross effect with various definitions of the mechanism given in the literature relating to the heat exchange of different spin reservoirs. [39, 42] This mechanism will not be discussed in detail as part of this thesis.

1.4 An Introduction to EPR

1.4.1 Electron Spin

Electrons have an intrinsic property called "spin" and an appropriate spin quantum number, where:

$$s = \frac{1}{2} \qquad \textit{Equation 1.7}$$

Electrons can "spin" in two possible orientations i.e. in an up (alpha) or down orientation (beta) and as electrons are charged this gives rise to two possible magnetic spin quantum numbers, m_s:

$$m_s = \pm\frac{1}{2} \qquad \textit{Equation 1.8}$$

For a system the sum of the m_s values gives rise to S which is the total electron spin quantum number. The overall "spin" of the system is characterised by the spin angular momentum vector **S** which is vector quantised in units of ħ:

$$|\mathbf{S}| = \sqrt{S(S+1)} \qquad \textit{Equation 1. 9}$$

There are $2S + 1$ allowed projections of this onto an arbitrarily chosen axis, taken as the z-axis, which coincides with the direction of the applied magnetic field vector **B**:

$$M_S = -S, -S+1, \ldots, S-1, S \qquad \textit{Equation 1.10}$$

1.4.2 The Zeeman Effect

In the absence of an external magnetic field the M_S states are degenerate. When a magnetic field is applied to the system, the M_S states have different energy values due to the Zeeman effect. In a radical system containing at least 1 unpaired electron and where M_S does not equal zero; EPR can be used to measure the energy difference in M_S states.

EPR is a spectroscopic technique that uses magnetic resonance to study systems containing unpaired electrons; this includes species containing multiple unpaired electrons such as the Gd(III) ion. The simplest EPR experiments are continuous wave experiments (CW) and are normally performed at X-band (9.5 GHz). In CW spectroscopy, transitions between different spin states can be observed whereas NMR observes transitions between nuclear spin states **Figure 1.17**. There is a phenomenon that

can occur called the hyperfine interaction which is second order perturbation between the electronic and nuclear Zeeman effects.

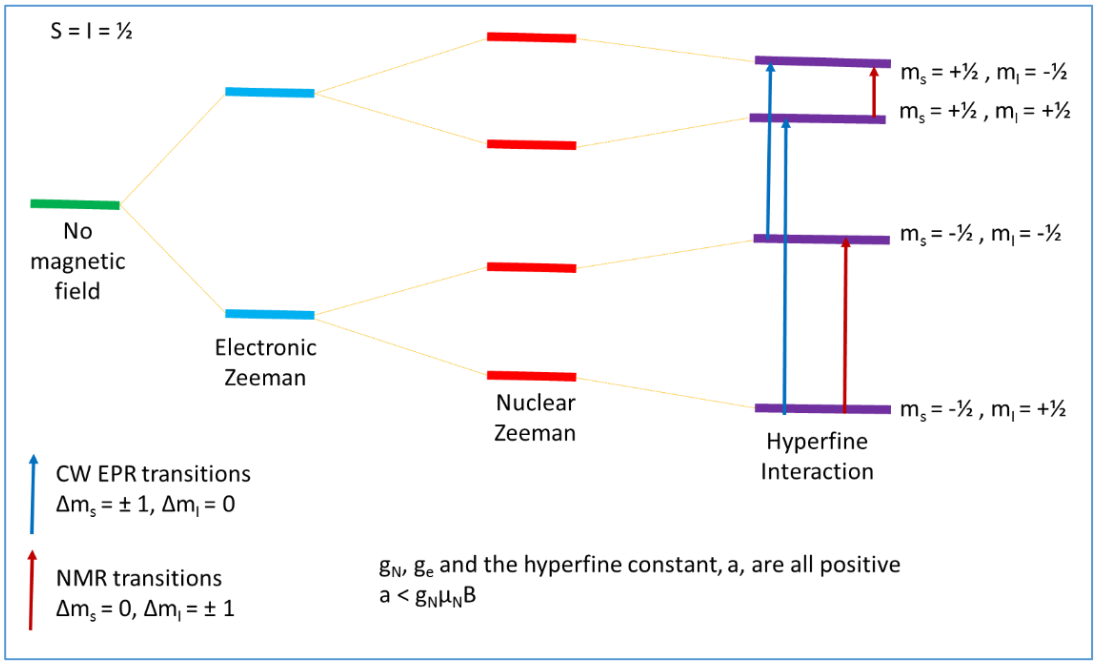

Figure 1.17: A schematic representation of EPR and NMR transitions for electron and nuclear spin-half systems ($S = I = ½$). Note: the hyperfine interaction is a second order perturbation; the magnitude of this interaction is exaggerated in this representation. The case for a lanthanide ion such as Gd(III), where there are seven unpaired electrons, is far more complex.

1.4.3 The *g*-value

The microwave frequency is held constant in CW EPR and the magnetic field 'swept' until electron resonance occurs **Figure 1.18**. Allowed transitions occur when $\Delta M_s = \pm 1$.

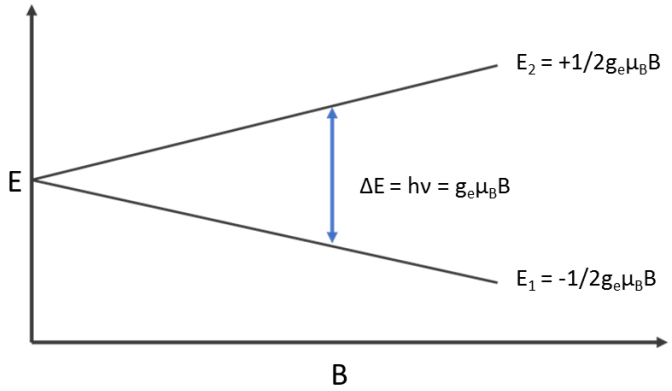

Figure 1.18: The electronic Zeeman levels and corresponding transition in EPR spectroscopy for a simple $S = 1/2$ system.

The effective *g*-value indicates where the species comes into resonance and is unique to each individual system, indicating the kind of environment the unpaired electron is in. Depending on the anisotropy of the system the *g*-value can have a single value consisting of components, g_x, g_y and g_z. A simple CW X-band experiment is simulated and shown below in **Figure 1.19** where the *g*-value would be the peak value when the spectrometer is in absorption mode, equivalent to the turning point for the first derivative mode. Spectrometers measure around a 100 kHz Zeeman modulation, which electronically takes the derivative of absorption and is used to capture a signal from background noise. Therefore, most spectra are presented in first derivative mode.

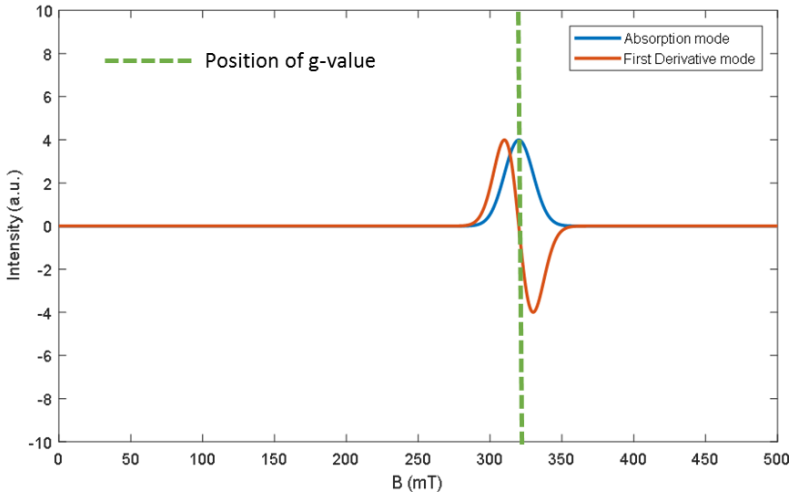

Figure 1.19: Simplified plot of an example EPR spectrum.

Knowledge of the *g*-value is important for the development of DNP MRI, in particular for the cross effect. For a given microwave frequency, if there are two radical species in a sample then in order for the cross effect to occur their *g*-values must differ by that of the Lamour frequency of the nucleus that needs to be hyperpolarised. Therefore, the *g*-value of each radical centre should be known and the difference between the two at least on the correct order of magnitude of the nuclear Larmor frequency if MAS is to also be used.

1.4.4 Ligand Field Splitting Parameters

In a multi-electron system where $S > ½$ the electrons can interact with each other. One way is that their orbitals can partially overlap known as an isotropic exchange interaction. If this occurs through other atoms this is known as superexchange. The other is through the anisotropic dipole-dipole interaction which is normally averaged to zero through molecules rapidly tumbling in fluid solution. It can be thought of as the effect of the magnetic field created by one electron on another. This interaction depends on the distance between the electrons and their relative orientations. As a result, it is dependent on the ligand field of the system. The zero-field splitting Hamiltonian which contributes to the overall Spin Hamiltonian is given in **Equation 1.11**.

$$\widehat{H}_{ZF} = D\left[\hat{S}_z - \frac{1}{3}S(S+1)\right] + E(\hat{S}_x^2 - \hat{S}_y^2) \qquad \textit{Equation 1.11}$$

Where *D* is the axial ligand field splitting parameter and *E* is the rhombicity parameter. *D* and *E* are connected to the ligand field splitting parameters shown in **Equation 1.12** and **Equation 1.13**.

$$D = 3B_2^0 \qquad \textit{Equation 1.12}$$

$$E = B_2^2 \qquad \textit{Equation 1.13}$$

The ratio of *E*/*D* can give information about the extent of the rhombohedral distortion of the anisotropy, with a maximum value of 1/3. [46]

1.4.5 EPR of Gadolinium(III)

The Gd(III) ion has a totally symmetric ground state of $^8S_{7/2}$ with all 4*f* shells half-filled and total momentum is approximately equal to the spin momentum (*J* approximately equals *S*). As a result the free ion has an isotropic magnetic field **Figure 1.20**.

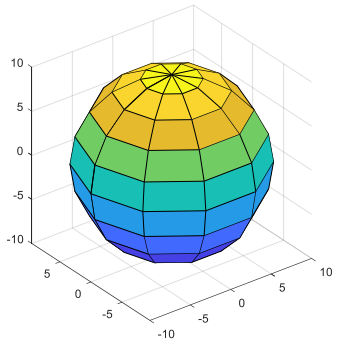

Figure 1.20: Schematic representation of a spherical isotropic magnetic field created using MATLAB®.

Gd(III) has seven unpaired electrons and before a magnetic field is applied all the spin states have the same relative energy. These are then all equally split as the magnetic field is increased. There is a negligible nuclear Zeeman contribution for Gd(III) because 97.5 % of gadolinium nuclei have $I = 0$ (^{155}Gd and ^{157}Gd have $I = 3/2$ and are a total of 2.5 % naturally abundant) so this does not need to be accounted for a good approximation. For a given microwave frequency all the allowed $\Delta M_S = \pm 1$ transitions are the same in value **Figure 1.21**.

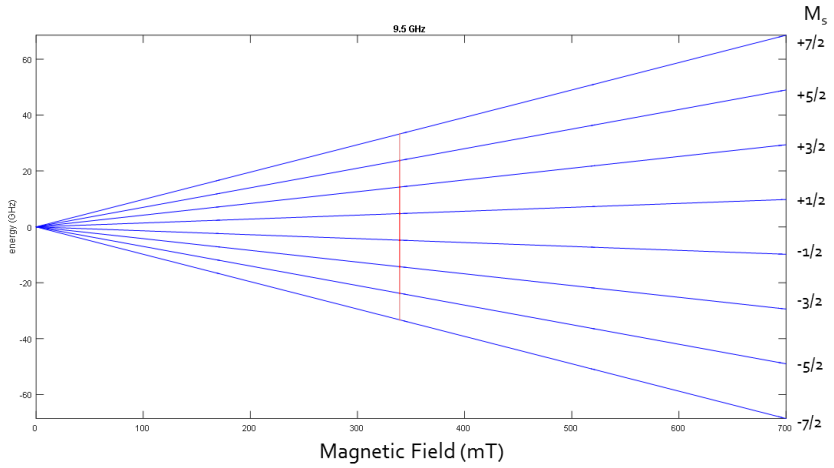

Figure 1.21: A simulated transition map showing the energy levels of the Gd(III) free ion as a function of magnetic field strength. Note: The magnetic field is applied parallel to the principal axis.

However, when the ligand field parameter *D* is not equal to 0 there is an axial distortion. Whilst the energy levels split appropriately with application of a magnetic field, as in the case of the isotropic example, the energy levels are no longer the same to begin with, i.e. the Kramers doublets are no longer energy degenerate. The order in which the Kramers doublets order themselves will depend on whether *D* is negative ('prolate' anisotropy) or positive ('oblate' anisotropy) in value. The principle is demonstrated in **Figure 1.22** and **Figure 1.23**, respectively. [47]

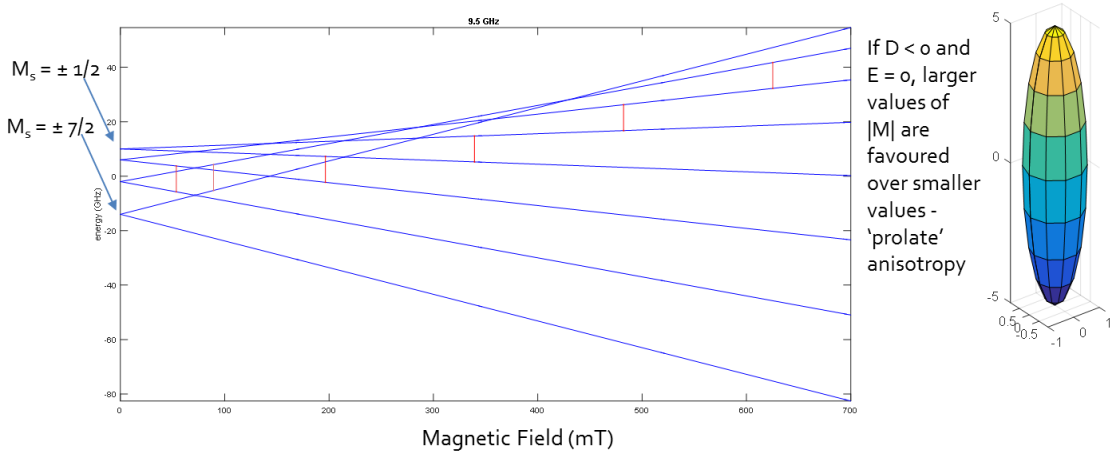

Figure 1.22: A simulated transition map showing the energy levels and how they are not degenerate when the applied magnetic field is zero when *D* is less than 0 in value resulting in prolate anisotropy.

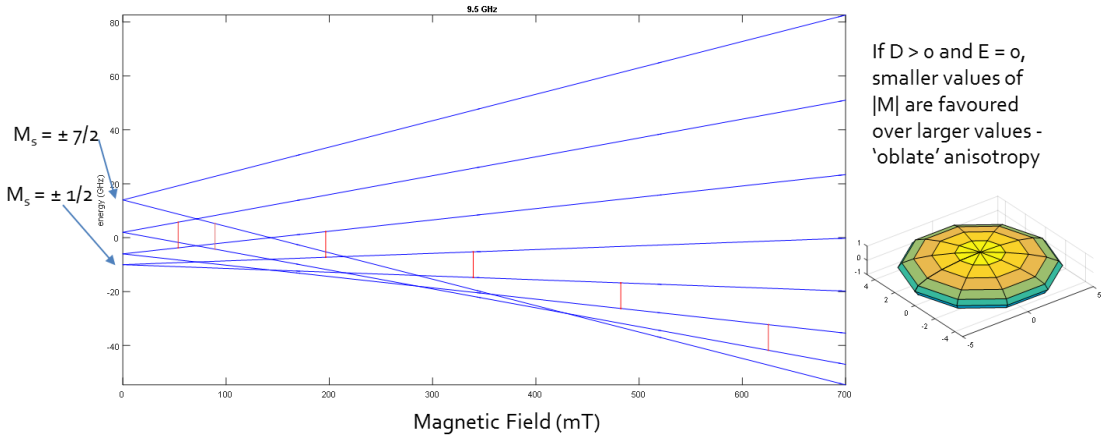

Figure 1.23: A simulated transition map showing the energy levels and how they are not degenerate when the applied magnetic field is zero when *D* is greater than 0 in value resulting in oblate anisotropy.

When *E* is not equal to zero there is now a rhombicity parameter and contribution to our system. In the absence of a magnetic field our doublets remain. However, as a magnetic field is applied the splitting of the energy states is no longer straight forward and depends more strongly on the direction in which the magnetic field is applied. We are also no longer able to speak in terms of 'prolate' or 'oblate' anisotropy due to the increased complexity. [46] Such a system is shown in **Figure 1.24**.

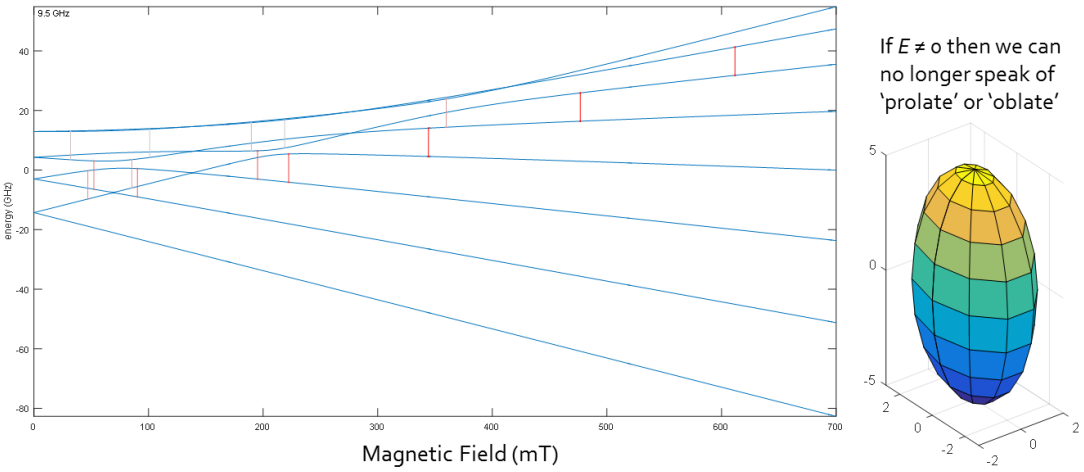

Figure 1.284: A system where *E* is a non-zero value and there is a more complex relationship in terms of energy levels and applied magnetic field. Note: The non-linear energy levels in the magnetic field also occur for an axial system when moving away from the z-direction.

1.5 Project Aims

In current DNP, monoradicals are used, such as trityl based radicals, as the source of unpaired electrons. The main mechanism by which the electron polarisation transfer occurs is the solid-effect mechanism for which monoradicals with a single narrow EPR line are ideal. [43] Magic Angle Spinning DNP (MAS-DNP) at low temperature has demonstrated itself useful for application to DNP MRI and DNP NMR. [44] As a result, recently, there has been a shift in focus to high-field MAS-DNP where the cross-effect mechanism is used as an alternative to the solid-effect mechanism and a large signal enhancement is expected for biradical species. [40] *Vidal-Gancedo et al.* have developed a novel, mixed, covalently bound biradical using this for fast dissolution DNP with an enhancement signal of greater than 50,000 times. [41] For the cross-effect to be effective, the difference in *g*-value, obtained from EPR spectroscopy for the two radical species

needs to be on the order of the Larmor frequency of the nucleus which needs to undergo polarization. After EPR investigations have been explored, Gd(III) complexes, developed originally as MRI contrast agents may be able to be used for this application and therefore, undergo development as DNP electron polarization transfer agents. The target is to create a far more effective and efficient electron polarization transfer agents for DNP.

This thesis will first set out to explore in more detail how properties of metallodrugs can be varied based on their environment. The study will initially take place on simpler systems, i.e. ones where only a single SAP/TSAP isomer is present. This will involve ligation of the metal ion with various ligands. This will be followed by studies such as EPR spectroscopy to see how this impacts parameters such *g*-value as well as the ligand field splitting parameters.

After these initial aims have been completed this project will continue to look at increasingly more complex systems i.e. those that are no longer C_4 symmetric and also have a mixture of the TSAP and SAP isomers. Furthermore, bimetallic systems will be explored to ascertain if the same principle found for monometallic complexes can also be applied here.

The main aim of the project is to establish if these findings can lead to an application for biomedical imaging. Using the bimetallic complexes and various ligands, including asymmetric ones, we will aim to see if varying coordination environment can aid in appliation for DNP **Figure 1.25**.

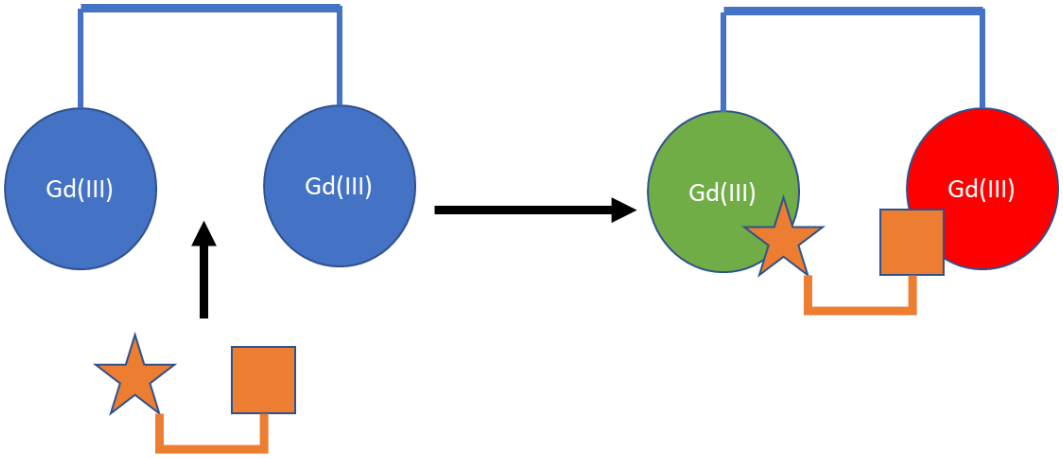

Figure 1.25: Schematic of how ligand binding is hypothesised to change the environment of a bis-Gd(III) complex.

1.6 References

[1] S. P. Fricker, "The therapeutic application of lanthanides," Chem. Soc. Rev., no. 35, p. 524–533, 2006.

[2] M. Bottrill, L. Kwok and N. J. Long, "Lanthanides in magnetic resonance imaging," Chem. Soc. Rev., vol. 6, vol. 35, pp. 557-571, 2006.

[3] S. A. Ametamey, M. Haner and P. A. Schubiger, Chemical Reviews, vol. 108, no. 5, pp. 1501-1516, 2008.

[4] K. L. Nash and M. P. Jensen, SEPARATION SCIENCE AND TECHNOLOGY, vol. 5&6, no. 36, p. 1257–1282, 2001.

[5] S. A. Cotton, C. R. Chimie, vol. 8, p. 129–145, 2005.

[6] O. A. Blackburn, R. M. Edkins, S. Faulkner, A. M. Kenwright, D. Parker, N. J. Rogers and S. Shuveav, Dalton Trans., no. 45, pp. 6782-6800, 2016.

[7] O. A. Blackburn, J. D. Routledge, L. B. Jennings, N. H. Rees, A. M. Kenwright, P. D. Beer and S. Faulkner, "Substituent effects on fluoride binding by lanthanide complexes of DOTA-tetraamides," Dalton Trans., vol. 45, pp. 3070-3077, 2016.

[8] G. Vocaturo, F. Colombo, M. Zanoni, F. Rodi, E. Sabbioni, R. Pietra, "Human exposure to heavy metals. Rare earth pneumoconiosis in occupational workers," Chest, no. 83, pp. 780-783, 1983.

[9] P. Robert, X. Violas, S. Grand, S. Lehericy, J-M. Idée, S. Ballet, C. Corot, "Linear Gadolinium-Based Contrast Agents Are Associated With Brain Gadolinium Retention in Healthy Rats," Investigative Radiology, vol. 51, no. 2, p. 73–82, 2016.

[10] M. W. Brechbiel, M. Williams, C. A. Regino, M. Bernardo and K. Nwe, Bioorg. Med. Chem., vol. 16, no. 181, p. 5925–5931, 2010.

[11] J. D. Routledge, M. W. Jones, M. Trapiano and S. Faulkner, Inorg. Chem., vol. 54, pp. 3337-3345, 2015.

[12] A. Tartaro and M. T. Maccarone, "The utility of gadoteric acid in contrast-enhanced MRI: a review," Reports in Medical Imaging, vol. 8, pp. 25-35, 2015.

[13] G. Tircso, B. C. Webber, B. E. Kucera, V. G. Young and M. Woods, Inorg. Chem., vol. 17, no. 50, pp. 7966-7979, 2011.

[14] K. J. Miller, A. A. Saherwala, B. C. Webber, Y. Wu, A. D. Sherry and M. Woods, Inorg. Chem., vol. 49, pp. 8662-8664, 2010.

[15] S. I. Weissman, J. Chem. Phys., vol. 10, pp. 214-217, 1942.

[16] J.-C. G. Bunzlia and C. Piguet, Chem. Soc. Rev., vol. 34, pp. 1048-1077, 2005.

[17] Z. Ahmed and K. Iftikhar, Inorganic Chemica Acta, no. 392, pp. 165-276, 2012.

[18] S. S. Skourtis, C. Lui, P. Antoniou, A. M. Virshup and D. N. Beratan, PNAS, vol. 29, no. 113, pp. 8115-8120, 2016.

[19] Z.-Q. You and C.-P. Hsu, International Journal of Quantum Chemistry, no. 114, p. 102–115, 2014.

[20] T. H. Forster, "Transfer Mechanisms of Electronic Excitation Energy," Radiation Research Supplement, no. 2, pp. 326-339, 1960.

[21] S. Faulkner, S. J. A. Pope and B. P. Burton-Pye, "Lanthanide Complexes for Luminescence Imaging Applications," Applied Spectroscopy Reviews, vol. 40, pp. 1-31, 2005.

[22] A. Beeby, I. M. Clarkson, R. S. Dickins, S. Faulkner, D. Parker, L. Royle, A. S. de Sousa, J. A. G. Williams and M. Woods, J. Chem. Soc. Perkin Trans. 2, pp. 493-504, 1999.

[23] B. C. Mayo, Chem. Soc. Rev., vol. 1, pp. 49-74, 1973.

[24] B. Bleaney, J. Magn. Reson., vol. 8, pp. 91-100, 1972.

[25] A. M. Funk, K.-L. N. A. Finney, P. Harvey, A. M. Kenwright, E. R. Neil, N. J. Rogers, P. K. Senanayake and D. Parker, Chem. Sci., vol. 6, pp. 1655-1662, 2015.

[26] H. Ding and F. Wu, “Image Guided Biodistribution and Pharmacokinetic Studies of Theranostics,” Theranostics, vol. 2, no. 11, p. 1040–1053, 2012.

[27] A. M. Blamire, “The technology of MRI - the next 10 years?,” The British Journal of Radiology, vol. 81, pp. 601-617, 2008.

[28] A. Webb, Introduction to Biomedical Imaging, Hoboken, New Jersey: John Wiley & Sons, Inc., 2003.

[29] L. A. Ekanger, L. A. Polin, Y. Shen, E. M. Haacke and M. J. Allen, Contrast Media Mol. Imaging, vol. 11, no. 4, pp. 299-303, 2016.

[30] V. Kapoor, B. M. McCook and F. S. Toroh, “An Introduction to PET-CT Imaging,” RadioGraphics, vol. 24, no. 2, pp. 523-543, 2004.

[31] M. S. Judenhofer, H. F. Wehrl, D. F. Newport, C. Catana, S. B. Siegel and M. Becken, “Simultaneous PET-MRI: a new approach for functional and morophological imaging,” Nature Medicine, vol. 14, pp. 459-465, 2008.

[32] “UT Southwestern Medical Centre,” [Online]. Available: https://utswmed.org/medblog/radiation-pet-ct-scan/. [Accessed 10 05 2019].

[33] J. H. Ardenkjær, B. Friland and A. Gram, “Increase in signal-to-noise of >10,000 times in liquid state NMR,” PNAS, vol. 100, no. 18, pp. 10158-10163, 2003.

[34] R. E. Hurd, Y. F. Yen and A. Chen, “Hyperpolarized ^{13}C Metabolic Imaging Using Dissolution Dynamic Nuclear Polarization,” Journal of Magnetic Resonance Imaging, vol. 36, pp. 1314-1318, 2012.

[35] R. E. Hurd, Y. F. Yen and D. Mayer, “Metabolic Imaging in the Anesthetized Rat Brain Using Hyperpolarized [1-^{13}C] Pyruvate and [1-^{13}C] Ethyl Pyruvate,” Magnetic Resonance in Medicine, vol. 63, no. 5, pp. 1137-1143, 2010.

[36] K. Golman, R. I. Zandt and M. Lerche, “Metabolic Imaging by Hyperpolarized ^{13}C Magnetic Resonance Imaging for In Vivo Tumor Diagnosis,” Cancer Research, vol. 66, no. 22, pp. 10855-10860, 2006.

[37] T. V. Can, M. A. Caporini, F. Mentink-Vieger, B. Corzilius, J. J. Walish, M. Rosay, W. E. Maas, M. Baldus, S. Vegas, T. M. Swager and R. G. Griffin, “Overhauser effects in insulating solids,” Journal of Chemical Physics, p. 141, 2014.

[38] Y. Hovav, A. Feintuch and S. Vega, J. Magn. Reson, vol. 207, no. 2, pp. 176-189, 2010.

[39] A. S. L. Thankamony, J. J. Whittmann, M. Kaushik and B. Corzilius, Progress in Nuclear Magnetic Resonance Spectroscopy, Vols. 102-103, pp. 120-195, 2017.

[40] B. Corzilius, “Theory of solid effect and cross effect dynamic nuclear polarization with half-integer high-spin metal polarizing agents in rotating solids,” Physical Chemistry Chemical Physics, vol. 18, pp. 27190-27204, 2016.

[41] L. F. Pinto, I. Marin-Montesinos, J. L. Monez-Gomez, M. Pons, J. Veciana and J. Vidal-Gancedo, “NMR signal enhancement of >50,000 times in fast dissolution dynamic nuclear polarization,” ChemComm, vol. 53, pp. 3757-3760, 2017.

[42] D. Guarin, S. Marhabaie, A. Rosso, D. Abergel, G. Bodenhausen, K. L. Ivanov and D. Kurzbach, J. Phys. Chem. Lett., pp. 5531-5536, 2017.

[43] A. Abragam and W. G. Proctor, “Une nouvelle methode de polarisation dynamique des noyaux atomiques dans les solides,” C R Hebd Seances Acad Sci, vol. 246, pp. 2253-2256, 1958.

[44] D. A. Hall, D. C. Maus, G. J. Gerfen, S. J. Inati, I. R. Becerra, F. W. Dahlquist and R. G. Griffin, “Polarization-enhanced NMR spectroscopy of biomolecules in frozen solution.,” Science, vol. 276, pp. 930-932, 1997.

[45] O. A. Blackburn, N. F. Chilton, K. Keller, C. E. Tait, W. K. Myers, E. J. L. McInnes, A. M. Kenwright, P. D. Beer, C. R. Timmel and S. Faulkner, Angew. Chem. Int. Ed., vol. 54, pp. 10783-10786, 2015.

[46] J. A. Clayton, K. Keller, M. Qi, J. Wegner, K. Vanessa, H. Hintz, A. Godt, S. Han, G. Jeschke, M. S. Sherwin and M. Yulikov, Phys. Chem. Chem. Phys. , vol. 20, pp. 10470-10492, 2018.

[47] M. Benmelouka, J. Van Tol, A. Borel, S. Nellutla, M. Port, L. Helm, L.-C. Brunel and A. E. Merbach, Helv. Chim. Acta., vol. 92, pp. 2173-2185, 2009.

[48] S. Stoll and A. Schweiger, J. Magn. Reson., vol. 178, pp. 42-55, 2006.

[49] S. Stoll, G. Jeschke, M. Willer and A. Schweiger, J. Magn. Reson., vol. 130, pp. 86-96, 1998.

2 Synthesis of Lanthanide Complexes

2.1 General Introduction

Mono-gadolinium(III) complexes were needed to test the hypothesis that *g*-value, *D* and *E* could be varied based on environment. These values were varied depending on ligation of the complex (see **Chapter 3**).

Gd.DOTAMPh was chosen as a C_4 symmetric system with predominantly only a distorted SAP isomer present. *Zucchi et al.* describe this as the TSAP isomer in their paper but report dihedral angles (the angle between the coordinated nitrogen and oxygen atoms) of 38 °. Normally, TSAP can typically be between 25 ° – 30 °. [1, 2, 3] Other literature describes certain tetraamide complexes with dihedral angles of 37 °as a slightly distorted SAP isomer, we have therefore decided to do the same with Gd.DOTAMPh. The presence of only one isomer greatly simplifies our model when fitting CW EPR spectra (see **Chapter 3**).

Gd.DOTAMPh is a gadolinium(III) cyclen derived compound with a gadolinium bound in the centre of this macrocycle (**Figure 2.1**). It differs from the commonly used DOTAREM© contrast agent, which is in fact the sodium salt of $Gd.DOTA^-$, by changing the carboxylate groups for phenyl amides. Although not well established for commercial use, this compound can also be used effectively as a contrast agent and has been used as an NMR probe for protein-protein interactions. [4] Gd.DOTAMPh was needed in abundance for this project due to the vast number of EPR experiments of interest

involving anisotropy (see **Chapter 3**). As a result, much was needed to be synthesised using adapted literature procedures for relatively larger scaled amounts of the product. The europium(III) analogue was also synthesised for NMR analysis and luminescence titrations (**Figure 2.2**).

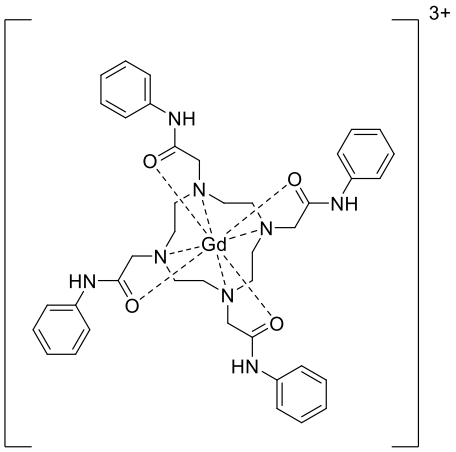

Figure 2.1: The structure of Gd.DOTAMPh. The counterions are not shown.

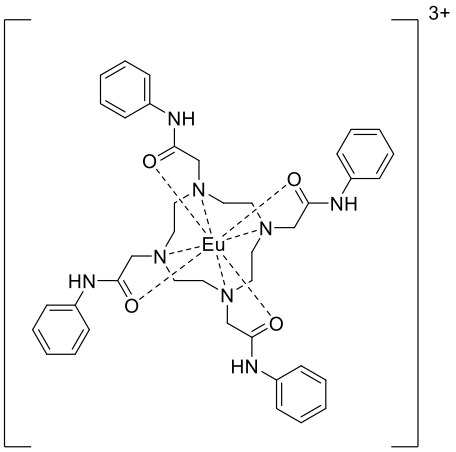

Figure 2.2: The structure of Eu.DOTAMPh. The counterions are not shown.

GdGd.p2DO3A (**Figure 2.3**) was chosen as a potential polymetallic complex for DNP studies and to be used in EPR studies. Once again the europium analogue was also synthesised to confirm the synthetic method by NMR. Such a system allows coordination of molecular ions that can bridge the two metal centres, and it has already been shown that such systems can bind guests such as fructose-1,6 bisphosphate and pyrophosphate. [5] It was anticipated that binding of a bridging guest which presents different donor ligands to the two metal centres would differentiate the coordination environments at the two lanthanide centres, resulting in a small but significant change in zero field splitting and, as a consequence, *g*-value for each gadolinium centre.

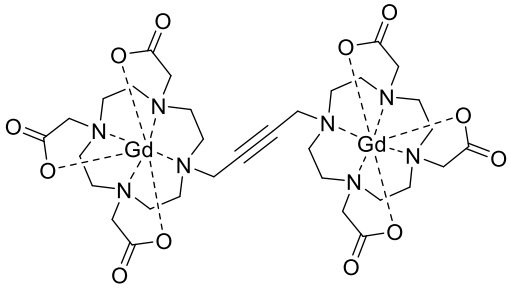

Figure 2.3: The structure of GdGd.p2DO3A.

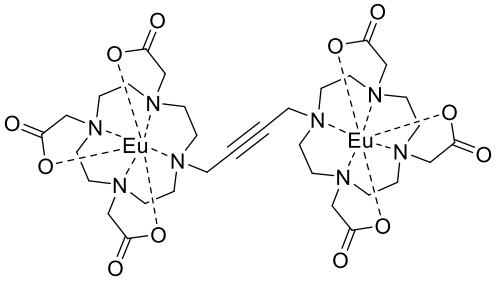

Figure 2.4: The structure of EuEu.p2DO3A.

Gd.pDO3A (**Figure 2.5**) was chosen as the mono-analogue of the bimetallic complex that was to undergo study for DNP. The main difference between the synthesis for complexes like Gd.pDO3A and a species like Gd.DOTA or Gd.DOTAMPh is that for the former three arms consist of one species and one is adapted to be different whereas for the latter all four are the same. EPR studies on this complex would give us an impression for how *g*-value, *D* and *E* all could be changed using different ligands for this non-C_4 symmetric system. The results should also give us an indication of what may be happening with the bis-analogue. The europium(III) analogue (**Figure 2.6**) was also synthesised to obtain useful NMR data.

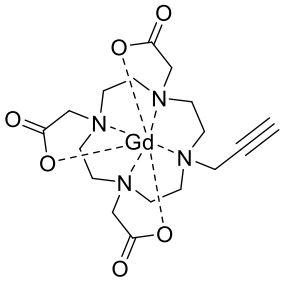

Figure 2.5: The structure of Gd.pDO3A.

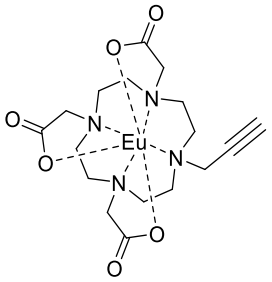

Figure 2.6: The structure of Eu.pDO3A.

2.2 Synthesis of Mono Gadolinium(III) Complexes

2.2.1 Synthesis of Gd.DOTAMPh

The synthesis of Gd.DOTAMPh was achieved as shown in **Figure 2.7** from adapted literature procedures. [6] Eu.DOTAMPh was synthesised in an analogous way except the europium salt, $Eu(OTf)_3$, was used rather than $Gd(OTf)_3$.

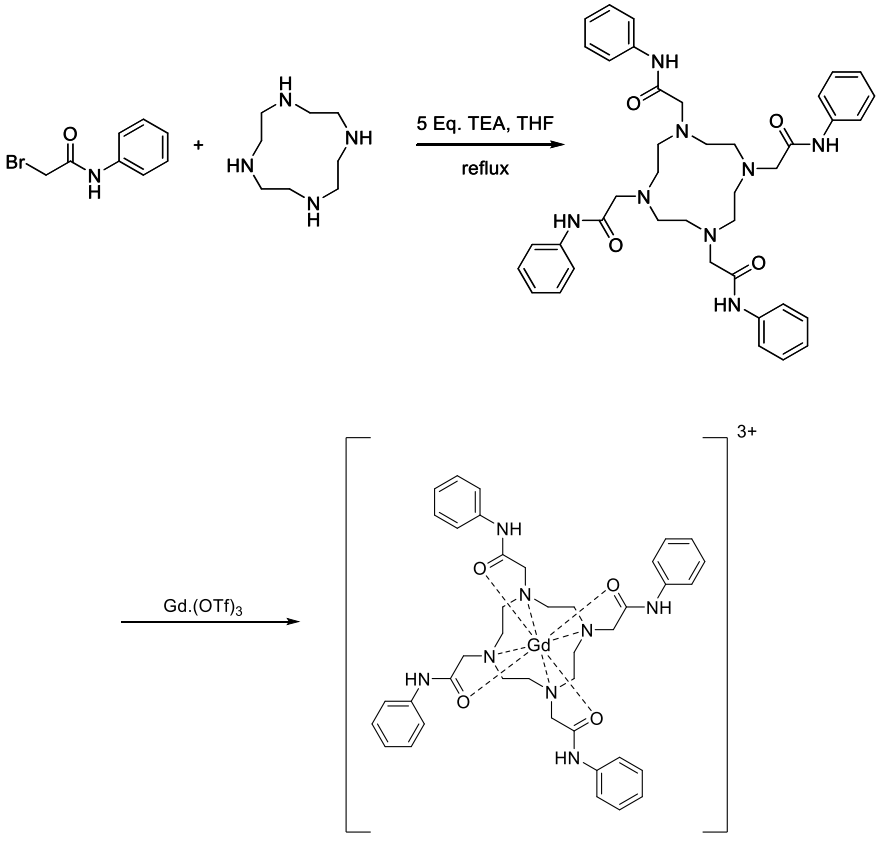

Figure 2.7: Overall synthesis of Gd.DOTAMPh.

The most common starting material for all macrocyclic based lanthanide complexes is 1,4,7,10-Tetraazacyclododecane which is more commonly known as cyclen. Cyclen is an ideal building block as it contains four equally spaced nitrogen atoms that can be used

in coordinate bonding and have different arms attached which in turn can also be used to coordinate to the lanthanide ion.

The first step towards making Gd.DOATMPh was to add the phenyl amide-based side arms to the cyclen backbone and synthesise 2,2',2",2"'-(1,4,7,10-tetraazacyclododecane-1,4,7,10-tetrayl)tetrakis(N-phenylacetamide). This was achieved by using 4 equivalents of *N*-(phenyl)bromoacetamide and basic conditions (5 equivalents of triethylamine) in dry tetrahydrofuran which was refluxed until the tetra substituted product was formed with negligible amounts of the tri, bis and mono substituted product present. The reaction regularly was monitored by both thin layer chromatography and low-resolution positive electrospray ionisation mass spectrometry.

Once the crude product was formed only a simple purification step was needed (recrystallization using hot DMF). Flash column chromatography was not required to remove any remaining tri, bis and mono substituted products. Drying the product completely took a significant amount of time, much longer than indicated by the literature procedure (3 days compared to 8 hours). However, a reasonable yield of 21 % was still obtained though far less than the literature value of 78 % (**Figure 2.8**).

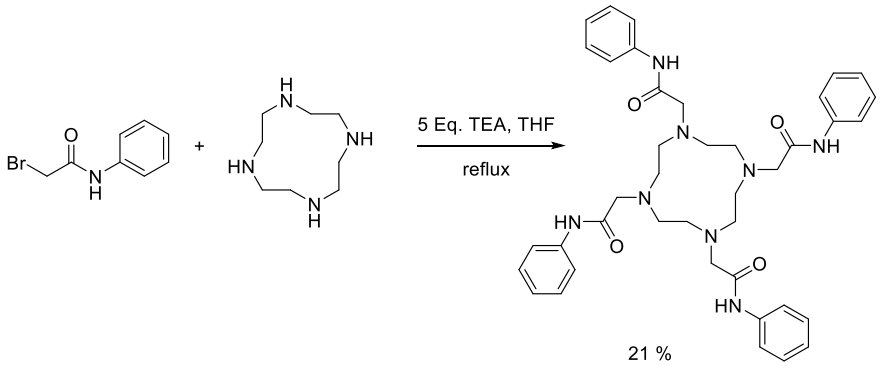

Figure 2.8: The synthesis of 2,2',2",2"'-(1,4,7,10-tetraazacyclododecane-1,4,7,10-tetrayl)tetrakis(N-phenylacetamide).

Once enough of the product had been synthesised all that remained was to insert the Gd(III) ion into the complex. The Eu(III) analogue was also synthesised by the same method to be used for experiments and analysis not suitable for gadolinium(III) substituents such as NMR and luminescence binding titrations (**Chapter 3**). The ^{1}H NMR of Eu.DOTAMPh shows that insertion of the lanthanide has been successful as the ^{1}H chemical shifts now vary from around -15 to +25 ppm (**Figure 2.9**). The shifting of the proton environments to this extreme is typical on insertion of Eu(III). [6]

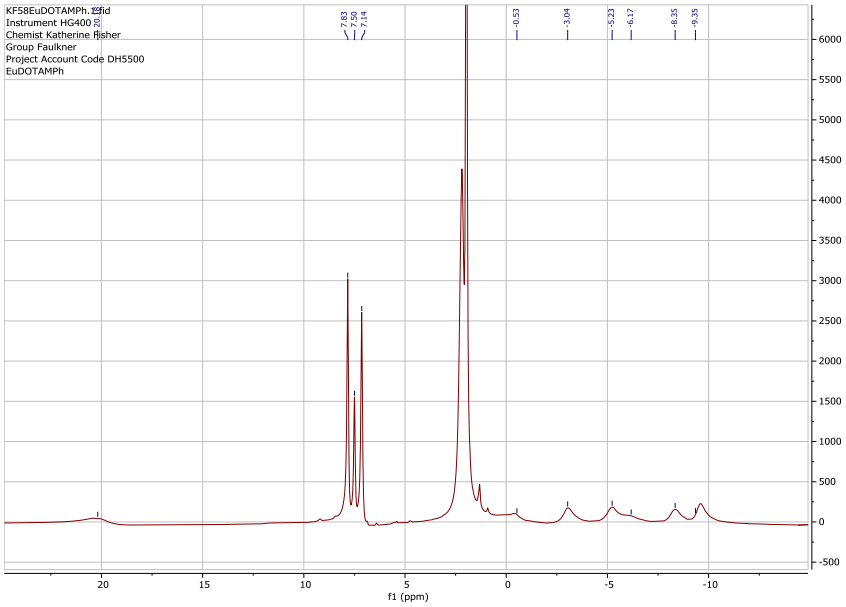

Figure 2.9: ^{1}H NMR of Eu.DOTAMPh which shows successful insertion based on the broad range of chemical shift. Note: Only peaks outside the range of 0 to 5 ppm are identified due to the water peak.

The binding of both the gadolinium(III) and europium(III) analogue was straightforward though the reaction had to be monitored carefully throughout to ensure the binding took place and that the hydroxide salt was not formed in great excess. The method for both was identical with the only difference being whether a gadolinium(III) or europium(III) salt was initially used as a reagent. To remove any other products and excess salts, an Amberlite XAD16N column was undertaken for purification using xylenol orange as a

means of testing so that no excess salt was remained bound to the column. The product was then eluted later when no other salts were confirmed present with 10 % MeCN:H_2O.

The gadolinium product was characterised using low resolution positive electrospray ionisation. The identity of the product was also confirmed by CW X-band EPR by comparing its form to a previously synthesised batch of Gd.DOTAMPh by Octavia Blackburn. A sample of this stock had undergone elemental analysis which also confirmed its identity. The yield for Gd.DOTAMPh was 50 % (**Figure 2.10**).

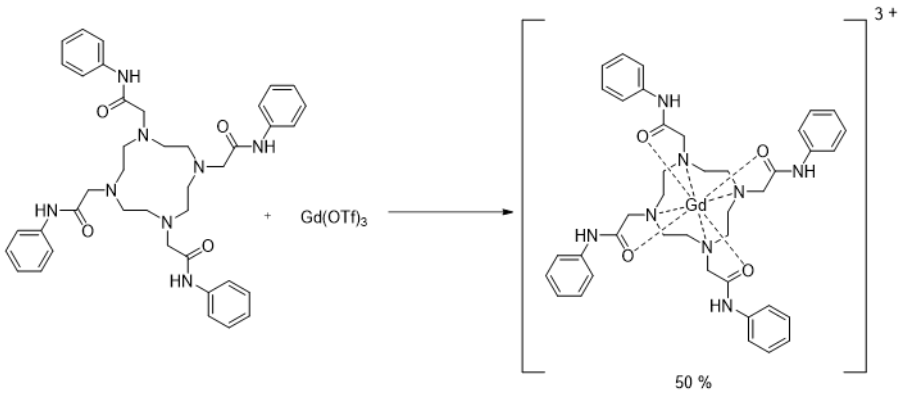

Figure 2.10: The synthesis of Gd.DOTAMPh

For the europium(III) complex NMR (already shown) could be taken as well as electrospray ionisation low resolution mass spectroscopy to confirm the identity of the bound complex. The yield for the europium(III) product was 50 % (**Figure 2.11**).

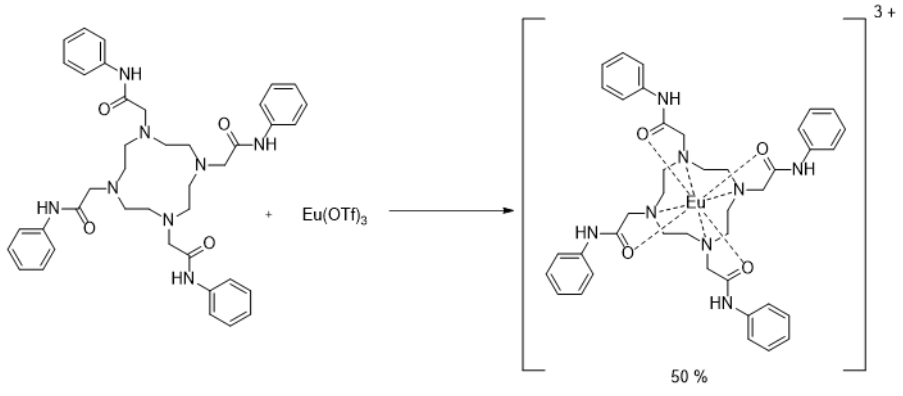

Figure 2.11: The synthesis of Eu.DOTAMPh

2.2.2 Synthesis of Gd.pDO3A

The overall synthesis of Gd.pDO3A is shown in **Figure 2.12** and was adapted from literature procedures. [7, 8]

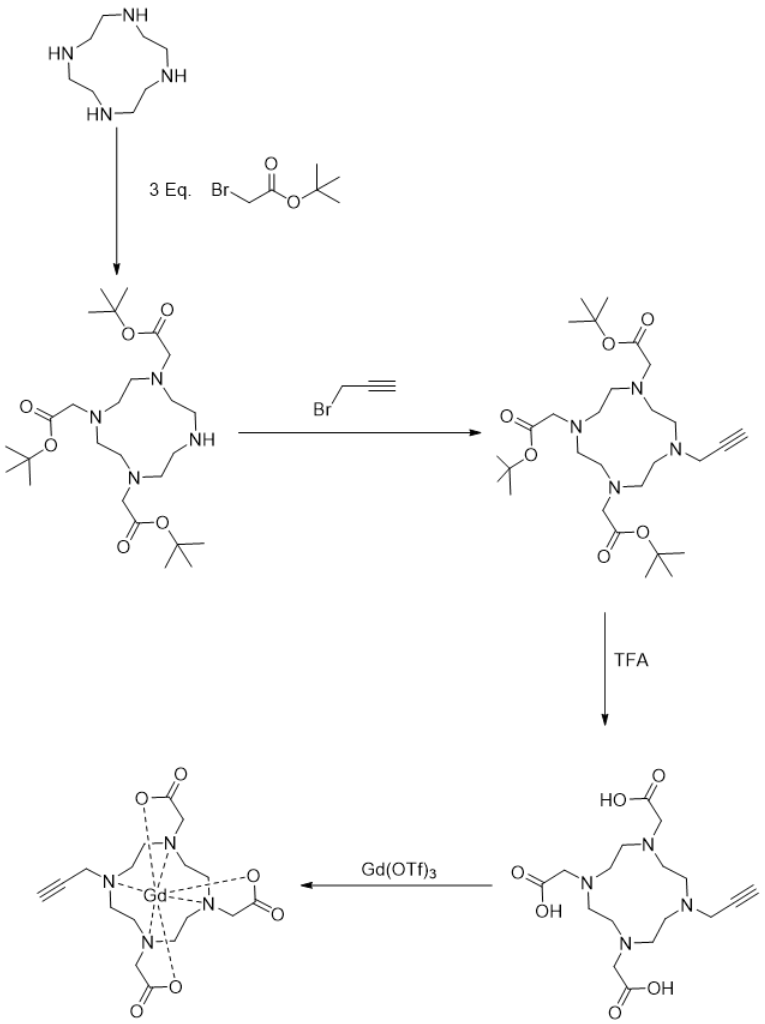

Figure 2.12: Overall synthesis of Gd.pDO3A.

Three *tert*-butyl acetate arms are added first to the cyclen starting material to form a very common precursor known commonly as the triester complex. The bulk of the *tert*-butyl groups combined to cyclen without the need for heating the reaction. The 3 equivalents of *tert*-butyl bromoacetate present and the lack of heat encourages the tetra product not

to form. Any side products (primarily the tetra substituted product) were removed by recrystallization with hot toluene. This afforded an acceptable yield 54 % and the reaction could be undertaken on a large scale (6 g) (**Figure 2.13**). This procedure used was adapted from literature. [7]

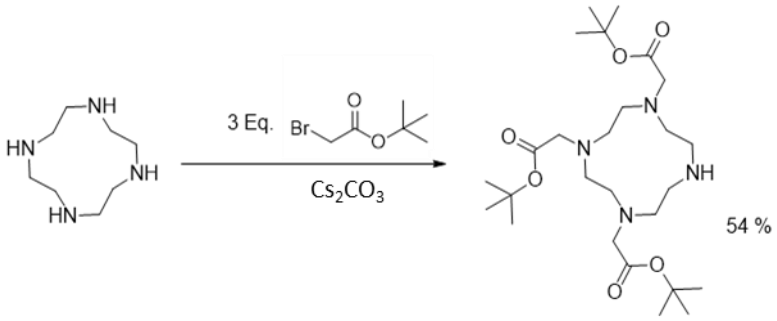

Figure 2.13: The synthesis of tri-tert-butyl 2,2',2''-(1,4,7,10-tetraazacyclododecane-1,4,7-triyl)triacetate.

The well-established triester product could then be reacted further to put the propargyl group into the final available position on the cyclen backbone. Propargyl bromide was reacted with triester at 0 ^{o} C using Cs_2CO_3 as a mild base to help deprotonate the nitrogen after the simple S_N2 reaction had occurred (**Figure 2.14**). The reaction mixture was purified after removing the solvent i*n vacuo* by adding toluene to dissolve the product and washing three times with water, so the impurities would pass into the aqueous layer. Any remaining propargyl bromide starting material would react with water and be removed i*n vacuo*. The reaction afforded a relatively pleasing yield of 53 % (**Figure 2.14**). The procedure was adapted from literature originally developed by *Jauregui et al.* for application for click chemistry. [8]

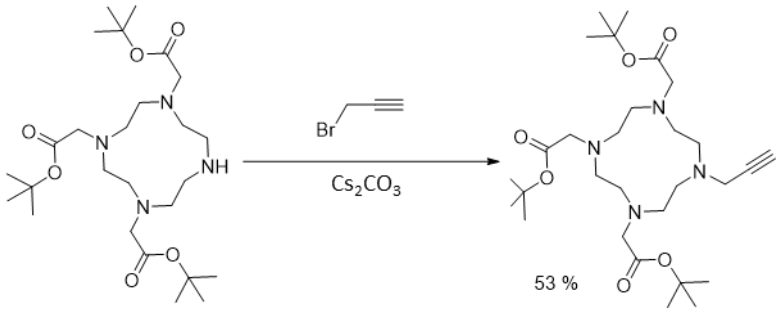

Figure 2.14: The synthesis of 'triester' pDO3A.

The propargyl ligand was confirmed to be attached by electrospray ionisation low resolution mass spectroscopy and ^{1}H NMR spectroscopy, where the proton on the α-carbon to the alkyne could be observed as the triplet at 2.07 ppm (**Figure 2.15**).

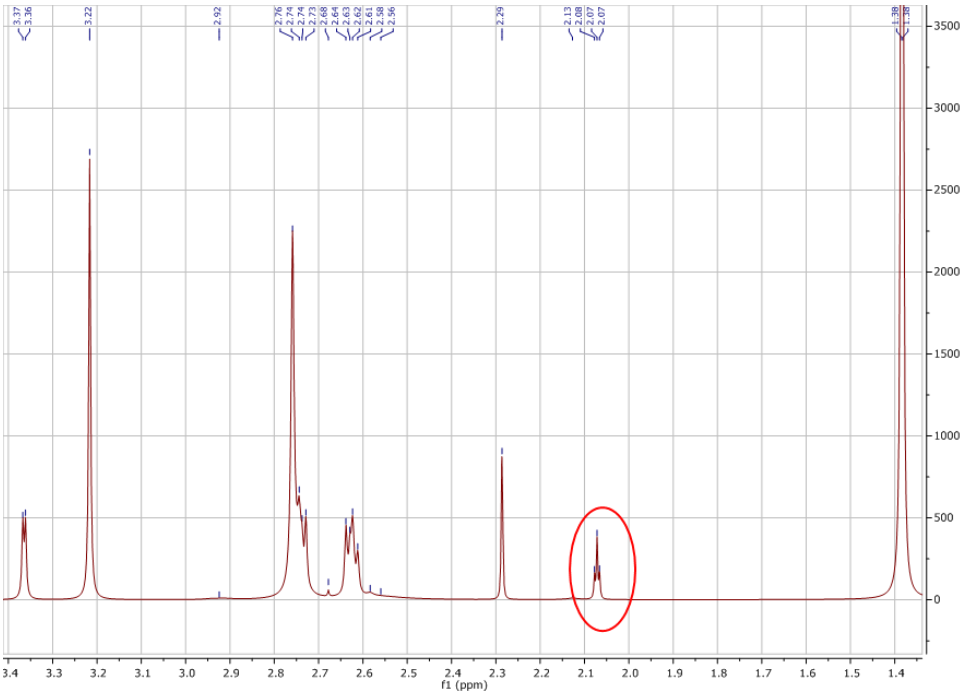

Figure 2.15: ^{1}H NMR spectrum of the triester of pDO3A. the proton on the alpha-carbon of the alkyne is highlighted by the red oval.

The next stage of the synthesis was to deprotect the other 3 arms of the macrocycle so that the lanthanide could later appropriately be inserted and bound (**Scheme 2.16**). The arms were deprotected with a standard trifluoracetic acid (TFA) deprotection. The main

issue with this procedure was the ‘stickiness’ of the TFA after the deprotection had been completed. Any remaining TFA could be clearly detected using ^{1}H NMR and this had be removed by many ether rinses where the solvent and TFA were removed each time *en vacuo* in a fumehood due to the toxicity of TFA. No other purification was needed for the reaction a 99 % yield was afforded as a result (**Figure 2.16**).

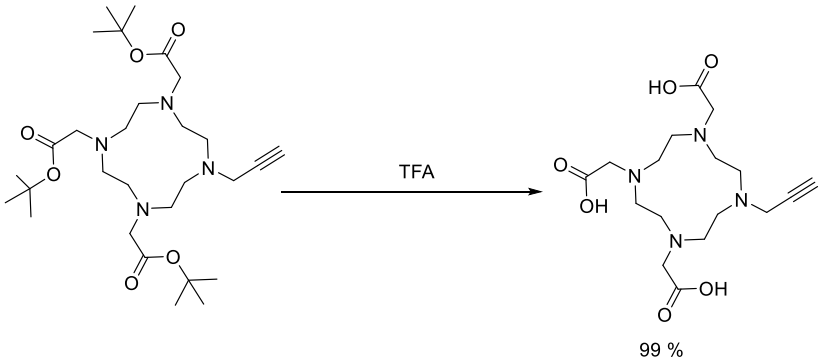

Figure 2.16: The deprotection of the triester of pDO3A.

The Gd(III) ion was then inserted using the same method as for Gd.DOTAMPh. This method was also repeated for the Eu(III) analogue. The pH had to be monitored carefully once again and the products were purified by an Amberlite XAD16N column using xylenol orange as a means of testing to see that no excess salt had remained bound to the column.

The identity of the Gd(III) complex was confirmed by LRMS and the Eu.pDO3A was confirmed by both mass spectrometry and NMR and compared to the literature. [9, 10] Gd.pDO3A afforded a 43 % yield and Eu.pDO3A a 50 % yield **Figure 2.17**.

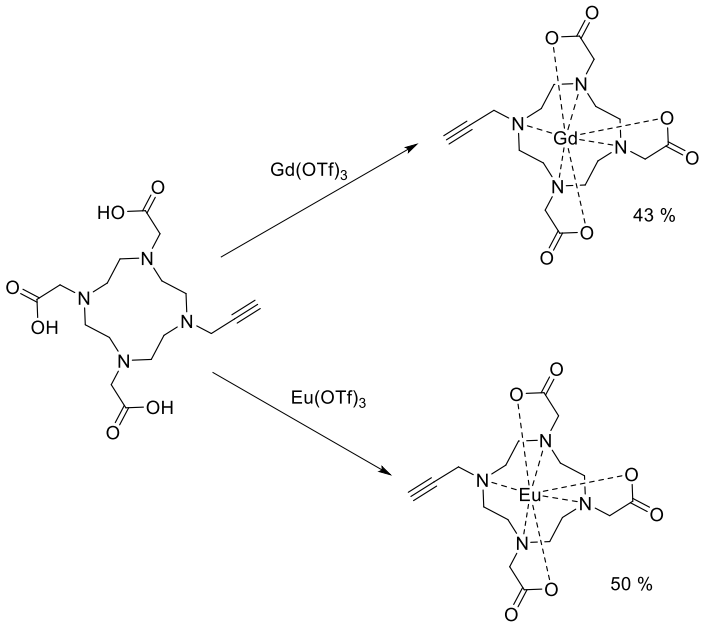

Figure 2.17: The synthesis of Gd.pDO3A and Eu.pDO3A.

The ^{1}H NMR spectrum for Eu.pDO3A is shown below (**Figure 2.18**). The fact there are peaks that have been shifted between around 30 ppm and -25 ppm far outside the range of a standard ^{1}H NMR shows the insertion has been successful. The broad peaks also indicate exchange within the system, likely to be between the SAP and TSAP isomers.

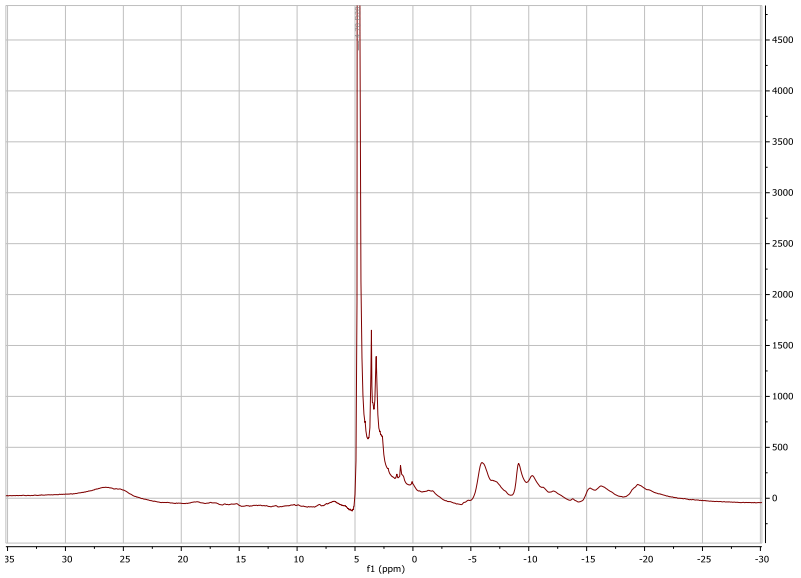

Figure 2.18: ^{1}H NMR spectrum of Eu.pDO3A which shows successful insertion based on the broad range of chemical shift.

2.3 Synthesis of Bimetallic Complexes

2.3.1 Synthesis of GdGd.p2DO3A

Synthesis of GdGd.p2DO3A was necessary to test the final aim of the project which would involve DNP NMR studies as well as EPR spectroscopy. The alkyne is essentially used as the central part of the linker and makes the system in theory symmetric i.e. the protons in the macrocycle should be in equivalent environments in each macrocycle.

The main difference between the synthesis for GdGd.p2DO3A and Gd.pDO3A is that rather than propargyl bromide being used as the fourth arm, two equivalents of triester complex were used with 1 equivalent of 1,4-dichlorobut-2-yne to form a bis-macrocyclic system. This can then be used, after deprotection, to form the bimetallic Gd(III) species and Eu(III) analogue.

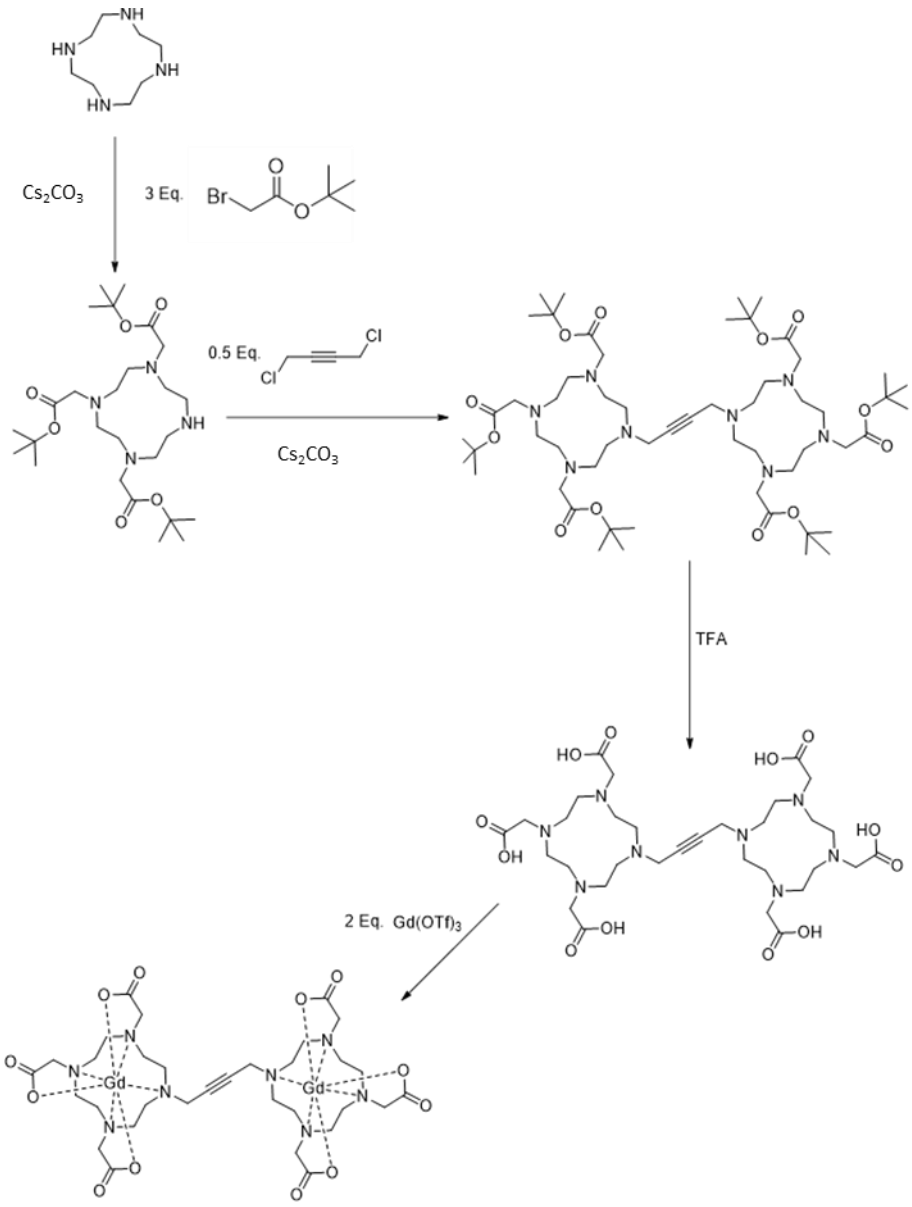

Figure 2.19: The overall synthesis of GdGd.p2DO3A.

The overall synthesis for GdGd.2pDO3A is shown in **Figure 2.19**. The first step in the synthesis is to again synthesise the triester complex with the same procedure which was used for the initial step of the synthesis of Gd.pDO3A. This was discussed in **Section 2.2.2**.

The 2 equivalents of triester were reacted with 1,4-dichlorobut-2-yne using Cs_2CO_3 as a base in acetonitrile. Purification proved very difficult for the product, eventually using a

96:4 by volume DCM:MeOH gravity alumina column to isolate the pure product as a yellow solid with 23 % pure yield (**Figure 2.20**). The NMR is shown in **Figure 2.21**.

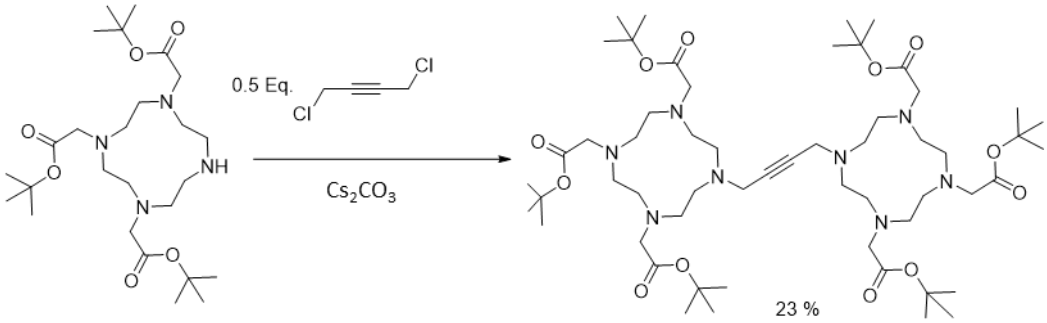

Figure 2.20: The synthesis of 1,4-bis-(tri-tert-butyl 2,2',2''-(1,4,7,10-tetraazacyclododecane-1,4,7-triyl)triacetate)- but-2-yne.

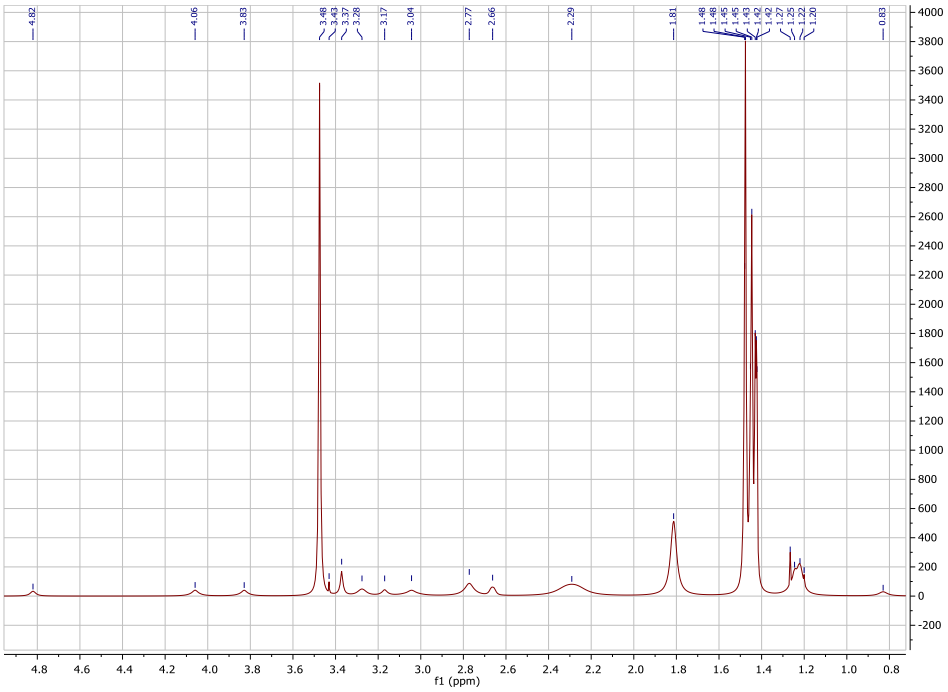

Figure 2.21: ^{1}H NMR spectrum of 1,4-bis-(Tri-tert-butyl 2,2',2''-(1,4,7,10-tetraazacyclododecane-1,4,7-triyl)triacetate)- but-2-yne.

There was also a 41 % yield of product with potential impurities as a pale orange oil. This was taken on to the next step to be purified completely after the TFA deprotection.

The TFA deprotection consisted of the addition of TFA in excess to the p2.DO3A in DCM and was left to stir at room temperature for 3 days (**Figure 2.22**).

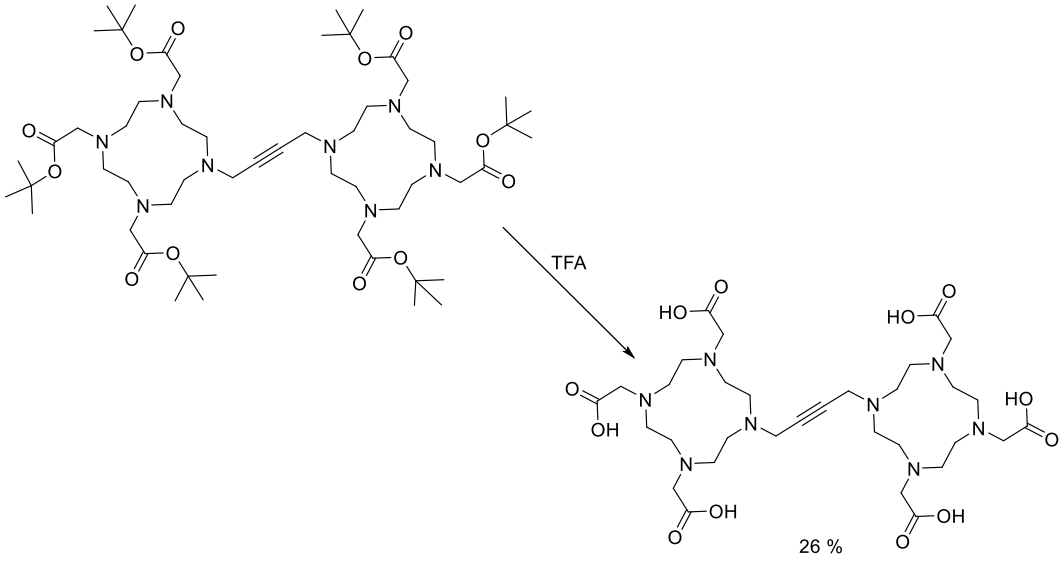

Figure 2.22: The synthesis of 2pDO3A.

The removal of TFA from the product proved difficult. To remove the remaining TFA, after the removal of the DCM *in vacuo*, methanol was added and removed i*n vacuo* a total five times. This was followed by a trituration by dissolving the product in the minimum amount of methanol and using ether to produce a pale pink solid. After filtering the solid, this was then re-dissolved in water and freeze dried to remove the water and remaining TFA.

After the TFA was finally removed the ^{1}H NMR showed that an impurity (related to the product but with one ^{t}Bu group remaining according to LRMS) remained. Fortunately, this could be removed as the impurity was soluble in chloroform but the product not. As a result, the solid was washed multiple times in chloroform and filtered. This result afforded 80 mg (26 % yield) of a pale pink solid which was confirmed as the product by NMR and ESI mass spectrometry.

The Gd(III) ion was then inserted using the same method as the insertion for Gd.pDO3A. This method was also repeated for the Eu(III) analogue. The pH had to be monitored carefully once again and the products were purified by an Amberlite XAD16N column using xylenol orange as a means of testing to see that no excess salt remained bound to the column.

The Gd(III) analogue was confirmed by MALDI mass spectrometry (**Figure 2.23**). The EuEu.2pDO3A was confirmed by both LC-MS mass spectrometry and ^{1}H NMR (**Figure 2.24**). [9, 10] GdGd.2pDO3A afforded a 58 % yield and EuEu.2pDO3A a 12 % yield (Figure 2.25).

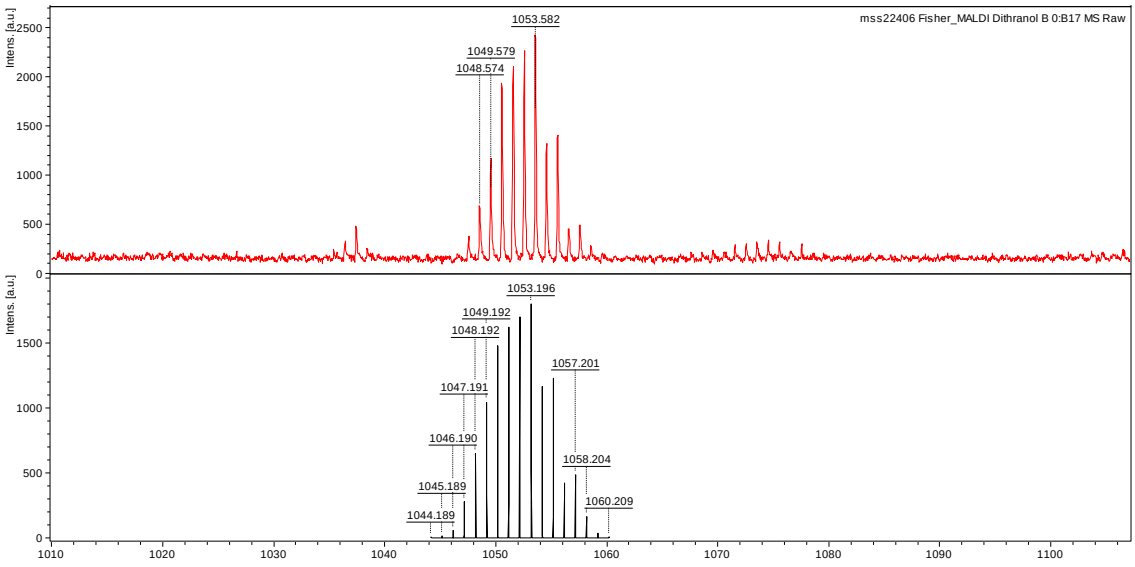

Figure 2.23: MALDI spectra of GdGd.p2DO3A. The top image is the actual spectra in dithranol matrix and the bottom is the theoretically calculated spectra.

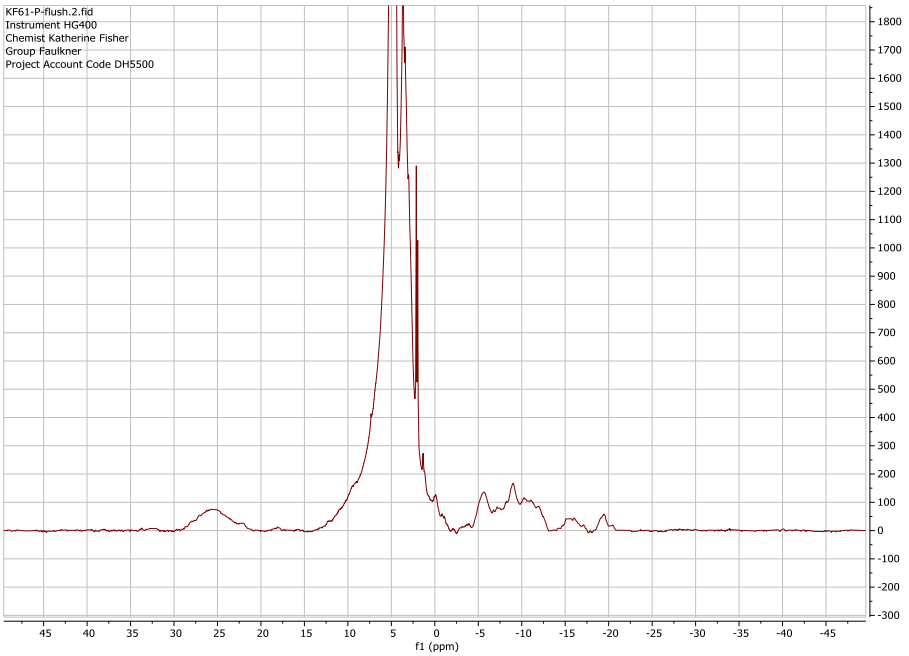

Figure 2.24: The ^{1}H NMR spectrum of EuEu.p2DO3A.

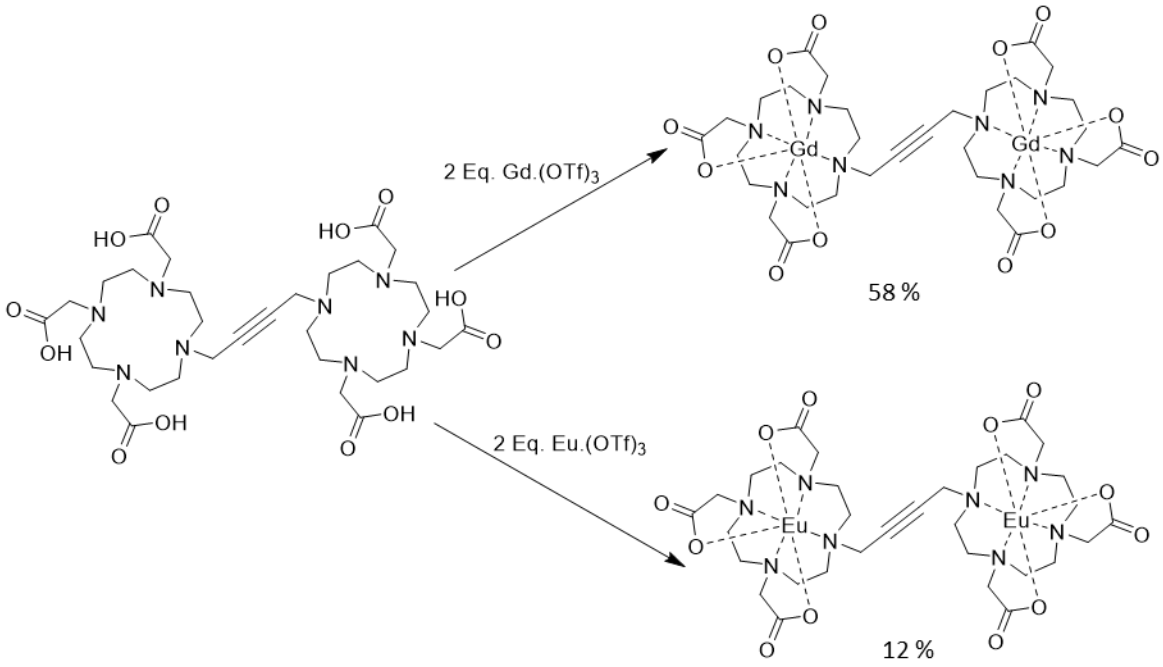

Figure 2.25: The complexation of lanthanides to give EuEu.p2DO3A and GdGd.p2DO3A.

2.4 References

[1] M. Woods, K. M. Payne, E. J. Valente, B. E. Kucera and V. G. Young Jr., Chem. Eur. J., vol. 25, no. 42, pp. 9997-10005, 2019.

[2] G. Zucchi, A. C. Ferrand, R. Scopelliti and J. C. G. Bunzli, Inorg. Chem., vol. 41, pp. 2459-2465, 2002.

[3] G. Zucchi, R. Scopelliti and J. G. Bunzli, J. Chem. Soc., Dalton Trans., p. 1975–1985, 2001.

[4] R. M. Almeida, C. F. Geraldes, S. R. Pauleta and J. J. Moura, "Gd(III) chelates as NMR probes of protein-protein interactions. Case study: rubredoxin and cytochrome c3," Inorg. Chem., vol. 21, no. 50, pp. 10600-10607, 2011.

[5] G. O'Maille, M. Jamshed and S. Faulkner, Manuscript in preparation, 2020.

[6] V. Lagostina, L. Leone, F. Carniato, G. Digilio, L. Tei and M. Botta, Inorganics, vol. 7, no. 43, 2019.

[7] A. Dadabhoy, S. Faulkner and P. G. Sammes, J. Chem. Soc. Perkin Trans. 2, pp. 348-357, 2002.

[8] M. Jauregui, W. S. Perry, C. Allain, L. R. Vidler, M. C. Willis, A. M. Kenwright, J. S. Snaith, G. J. Stasiuk, M. P. Lowe and S. Faulkner, Dalton Trans., vol. 0, pp. 6283-6285, 2009.

[9] L. Tear, "DPhil Thesis", University of Oxford, 2018.

[10] G. M. O'Mallie, "Personnal communication", University of Oxford, 2015.

3 Exploring Zero-Field Splitting upon Changing Axial Donor Ligand

3.1 Introduction

It has been shown that changes to the local ligand field can have profound consequences for the NMR, luminescence and EPR properties of lanthanide ions with inherent magnetic anisotropy, such as europium and ytterbium. [1, 2] In this chapter, these principles are extended to the behaviour of gadolinium(III) complexes, for which the ground state of the free ion has an isotropic electron distribution ($^8S_{7/2}$) where L is zero and there is therefore no *g*-anisotropy in the free ion.

Both X-band and Q-band CW (continuous wave) EPR and pulsed PEANUT (phase-inverted echo-amplitude detected nutation) experiments have been used to characterise these systems. Understanding the influence of the axial donors and ligand field on the zero field splitting (ZFS) parameters of Gd(III) will allow informed design of new contrast media for MRI. As discussed in **Chapter 1** of this thesis, the *D* and *E* values dictate the anisotropy of the system which is in turn related to magnetic susceptibility. This is important as, relaxivity is dependent on the χ_x, χ_y and χ_z terms of magnetic susceptibility which can be used to influence contrast agent design. Exploration of how *g*-value can vary will also allow for the development of electron polarisation agents for DNP MRI based on the theory discussed in **Chapter 1**.

It was decided to explore the effect of an axial ligand bound to the ninth coordination of the Gd.DOTAMPh complex and to observe how this would affect the anisotropy and *g*-value of the system. The synthesis of Gd.DOTAMPh is discussed in **Chapter 2**. Gd.DOTAMPh is a C_4 symmetric molecule when we consider a species bound in the ninth coordination site. The nature of how an axial donor ligand (X) binds to the ninth coordination site of Gd.DOTAMPh is shown in **Figure 3.1**.

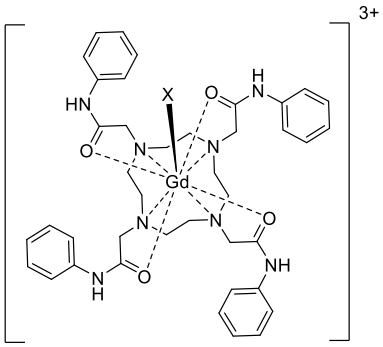

Figure 3.1: The nature of axial donor ligand (X) bound to the ninth coordination site of Gd.DOTAMPh. The triflate counterions are not shown.

3.2 Experimental Conditions for CW EPR

Measurements were initially taken using CW EPR using X-band (9.5 GHz) frequencies followed by Q-band (34 GHz) at 100 K. Measurements were carried out on a Bruker Biospin EMX spectrometer equipped with a high sensitivity Bruker probe head and an Oxford Instruments helium-flow cryostat. Modulation amplitudes and frequencies of 0.01 mT and 100 kHz were used, respectively. The microwave power was adjusted in order to avoid spectral distortions.

A 5 mM solution of Gd.DOTAMPh complex dissolved in 5:3 MeCN:^{t}BuOH by volume. This solvent system was initially chosen due to the very limited coordination of the solvent in the axial site on the metal since MeCN is a poor donor for lanthanides even though it can still bind, while ^{t}BuOH is too bulky to fit in the cavity. [3] This solvent system also forms an amorphous glass at very low temperatures which is important for any future applications for DNP NMR which needs this environment for electron polarisation mechanisms to occur.

Each axial donor was added in a 100-fold excess, giving a 500 mM solution of the axial ligand. The donor was added in excess in each case to ensure binding. The one exception was fluoride where only 10 equivalents were added (50 mM) as no EPR signal could be detected at higher equivalency. This could be due to fluoride binding strongly to the complex and forming aggregates that are EPR silent due to Gd(III) centres being held in too close proximity to one another. The would cause extremely rapid relaxation. There was some evidence for this shown by gel formation.

3.3 Computational Analysis of Results

The CW spectra were processed using MATLAB® and EasySpin® software. [4] For the frozen solution CW EPR data the *pepper* function was used. [4] After spectra were processed, using the software, parameters were extracted by fitting the spectra obtained using a non-linear least squares regression model where an overall RMSD value for the entire system is minimized to as close to zero as possible. Using the parameters extracted from the simulations, model spectra can be produced.

To obtain the best fit possible using the software, initial reasonable values are first approximated and simulated to see whether they give a model with a similar profile and features to the obtained spectra. After this has been established as a reasonable fit the simulation is undertaken for a set period before the results are examined. If the values are converging to a certain value and the model looks progressively like the data, then the simulation can be allowed to run until the software accesses that the best possible values have been obtained. If it is obvious that the values are converging far too slowly then the model with the initial values set for parameters will have to be adapted and reassessed.

The *g*-value was assumed to be isotropic due to the nature of the Gd(III) free ion and the assumption that the anisotropy comes from ligand-field perturbations from being in a coordination environment with the macrocycle and the axial donor ligand. Due to the C_4 symmetry of the system and the vast majority of the species being found as the distorted SAP isomer according to NMR of the Eu(III) analogue **Figure 3.2**. The NMR spectrum was taken in CD_3CN and the preference for distorted SAP in this solvent system has been reported in literature and is discussed in **Chapter 2**. [5] This indicated that only one species is present and the system can be modelled using one component.

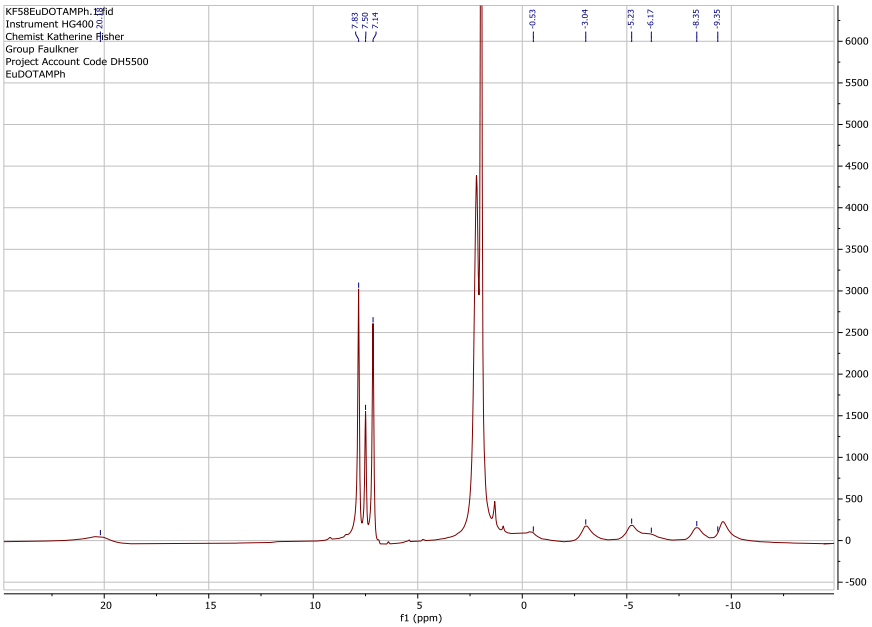

Figure 3.2: The NMR of Eu.DOAMPh which shows peaks only in the range of the distorted SAP isomer. The NMR was taken in CD_3CN. Note: Only peaks outside the range 0 to 5 ppm were identified due to the central water peak.

Using one component model to fit the obtained spectra makes the simulations much more facile. As discussed in **Chapter 1**, identifying *g*-values for different species is important in the application of DNP MRI and essentially tells us when our molecule comes into resonance.

D and *E*, are also crucial parameters to be simulated as they are directly related to the crystal field splitting parameters. They not only tell us about the magnitude and ordering of zero field splitting but also about the anisotropy of system which is important in the application of the development of new contrast agents as discussed in **Chapter 1**.

As well as, *g*-value, *D* and *E*, other various strain parameters were also obtained. *D*-Strain and *E*-Strain are introduced to account for inhomogeneous broadening of the resonances and are set to be Gaussian distributions given by **Equation 3.1** and **Equation 3.2**. It is assumed that there is no correlation between *D*-strain and *E*-strain. [6, 7]

$$P(D_i) = e^{-\left(\frac{2(D_i - D)}{D - Strain}\right)^2}$$ *Equation 3.1*

$$P(E_i) = e^{-\left(\frac{2(E_i - E)}{E - Strain}\right)^2}$$ *Equation 3.2*

The *H*-Strain values are used to account for unresolved hyperfine couplings of the gadolinium with the nitrogen nuclei ($I = 1$) and protons ($I = ½$) in the chelate. *H*-Strain 1, *H*-Strain 2 and *H*-Strain 3 correlate to the *H*-Strain values in the z, x and y-directions, respectively. The various strain values allow us to take into account line broadening in our spectra. Field measurements were not corrected relative to a standardized sample.

3.4 X-band Spectra

3.4.1 Gd.DOTAMPh

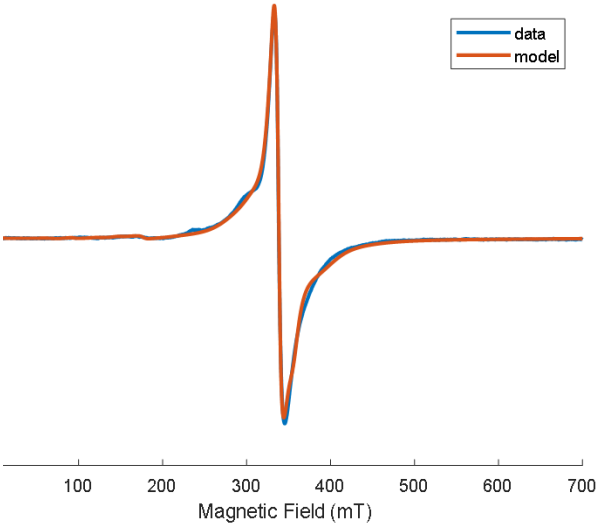

Figure 3.3: CW X-band frozen solution EPR spectrum of Gd.DOTAMPh at 100 K, experimental (blue) and simulated (red), using the parameters in Table 3.1.

Table 3.1: Parameters obtained from non-linear least square regression model at X-band.

g	1.987
D	-687 MHz
E	-227 MHz
D-Strain	1021 MHz
E-Strain	277 MHz
H-Strain 1	23 MHz
H-Strain 2	21 MHz
H-Strain 3	26 MHz

The fitting of Gd.DOTAMPh is of good quality as most of the features were accounted for well. The spectrum has a sharp central feature with a turning point at about 320 mT and secondary side features can just be distinguished. The *D* and *E* values are relatively large. The *D* value is negative and the *E* value is non-zero which suggest that the system has prolate anisotropy with a rhombohedral distortion. The *D*-strain value is rather large, hence the line-broadening of the central feature. Whilst the *H*-strain values are non-zero they are not particularly large for this species so only make small contributions to the secondary fine structure of the spectrum.

3.4.2 Benzylamine.Gd.DOTMAPh

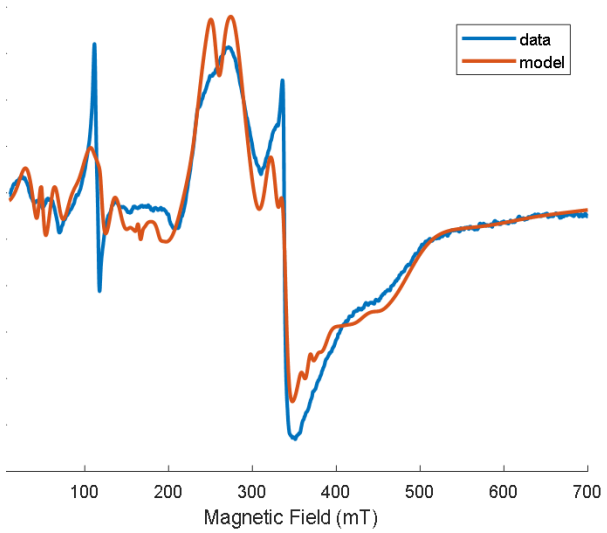

Figure 3.4: CW X-band frozen solution EPR spectrum of benzylamine.Gd.DOTAMPh at 100 K, experimental (blue) and simulated (red), using the parameters in Table 3.2.

Table 3.2: Parameters obtained from non-linear least square regression model for benzylamine.Gd.DOTAMPh at X-band.

g	1.995
D	-1419 MHz
E	-658 MHz
D-Strain	543 MHz
E-Strain	330 MHz
H-Strain 1	37 MHz
H-Strain 2	50 MHz
H-Strain 3	37 MHz

On addition of benzylamine the spectrum changed dramatically. The central feature is no longer sharp and there are a number of secondary features. The *D* and *E* values are significantly larger than for Gd.DOTAMPh. The magnitude of *D* provides a significant contribution to the shape of the spectrum. The relative *E*/*D* ratio is approximately 1/3 which is the maximum possible rhombohedral distortion in a system, though in practise this is more of an approximation and tends more to a value of 1/3. There is a slight increase in the *H*-strain values though these still remain relatively small. This spectrum proved much more difficult to fit using the EasySpin® software due to the larger number of secondary features (for instance those at 100 mT and 280 mT). Attempts to improve the fit by varying the model did not yield significant improvement.

3.4.3 Phenol.Gd.DOTAMPh

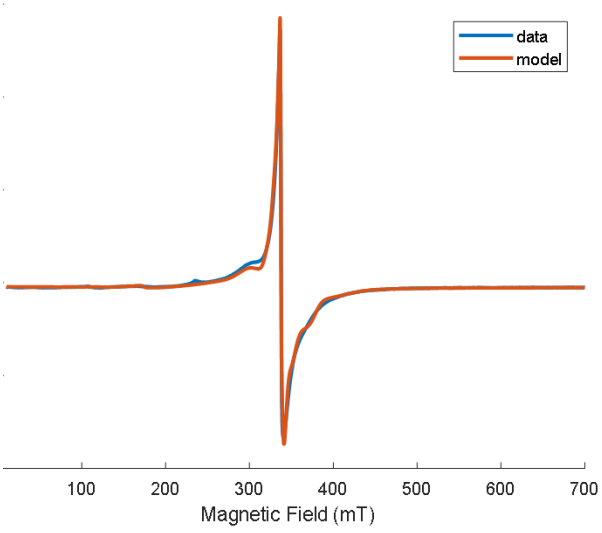

Figure 3.5: CW X-band frozen solution EPR spectrum of phenol.Gd.DOTAMPh at 100 K, experimental (blue) and simulated (red), using the parameters in Table 3.3.

Table 3.3: Parameters obtained from non-linear least square regression model for phenol.Gd.DOTAMPh at X-band.

g	1.989
D	-688 MHz
E	-111 MHz
D-Strain	698 MHz
E-Strain	72 MHz
H-Strain 1	129 MHz
H-Strain 2	2 MHz
H-Strain 3	32 MHz

The one component model fits this spectrum very well. On addition of phenol the central feature becomes much sharper than that for Gd.DOTAMPh. The secondary feature at about 300 mT can be seen more readily than for Gd.DOTAMPh due to the increased sharpness of the central feature. The *E*/*D* ratio has significantly reduced meaning the system is now tending more towards prolate anisotropy with a slight rhombohedral distortion. The *D*-strain is relatively large though not as large as for Gd.DOTAMPh with no axial ligand bound which could explain why the central feature is not as broad. The *g*-value is significantly different upon binding of phenol compared to the binding of benzylamine. Interestingly, one of the *H*-Strain values is much larger than the other two which contributes to line broadening. This could mean than the molecule is distorting on binding so that part of the chelate may have come into closer contact with the Gd(III) centre.

3.4.4 Benzoic acid.Gd.DOTMAPh

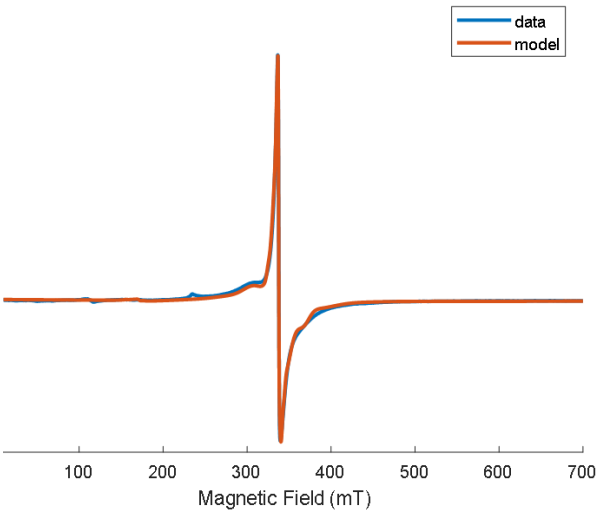

Figure 3.6: CW X-band frozen solution EPR spectrum of benzoic acid.Gd.DOTAMPh at 100 K, experimental (blue) and simulated (red), using the parameters in Table 3.4.

Table 3.4: Parameters obtained from non-linear least square regression model for benzoic acid.Gd.DOTAMPh at X-band.

g	1.989
D	-585 MHz
E	-94 MHz
D-Strain	602 MHz
E-Strain	43 MHz
H-Strain 1	128 MHz
H-Strain 2	28 MHz
H-Strain 3	30 MHz

Benzoic acid is another oxygen donor so it is not a surprise to see similarities between this and phenol.Gd.DOTAMPh. On addition of benzoic acid, the central feature, though very similar, ,becomes even sharper than when phenol was added to Gd.DOTAMPh. Though the spectra is similar to that of phenol.Gd.DOTAMPh there are subtle differences. The key difference is that the magnitude of *D* and *E* values are smaller, while the secondary features are not as well defined. Again there remains one *H*-strain value larger than the rest which suggests a similar distortion to that in the phenol.Gd.DOTAMPh is taking place.

3.4.5 Benzyl alcohol.Gd.DOTAMPh

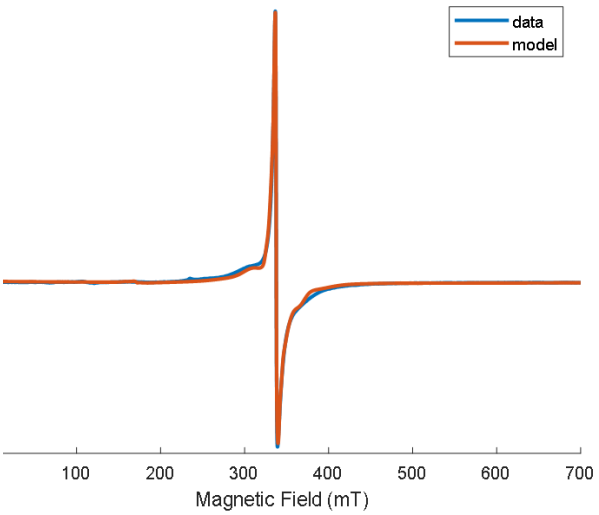

Figure 3.7: CW X-band frozen solution EPR spectrum of benzyl alcohol.Gd.DOTAMPh at 100 K, experimental (blue) and simulated (red), using the parameters in Table 3.5.

Table 3.5: Parameters obtained from a non-linear least square regression model for benzyl alcohol.Gd.DOTAMPh at X-band.

G	1.989
D	-538 MHz
E	-86 MHz
D-Strain	584 MHz
E-Strain	41 MHz
H-Strain 1	118 MHz
H-Strain 2	11 MHz
H-Strain 3	29 MHz

This spectrum is very similar in form to that of benzoic acid.Gd.DOTAMPh in shape. The *D* and *E* values are also comparable to that for benzoic acid. Benzyl alcohol is once again an oxygen donor and similar observations can be made.

3.4.6 Aniline.Gd.DOTAMPh

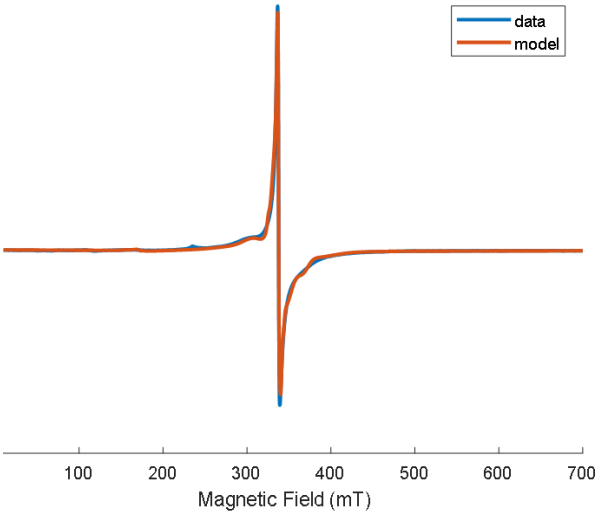

Figure 3.8: CW X-band frozen solution EPR spectrum of aniline.Gd.DOTAMPh at 100 K, experimental (blue) and simulated (red), using the parameters in Table 3.6.

Table 3.6: Parameters obtained from non-linear least square regression model for benzyl aniline.Gd.DOTAMPh at X-band.

g	1.989
D	-590 MHz
E	-88 MHz
D-Strain	619 MHz
E-Strain	30 MHz
H-Strain 1	89 MHz
H-Strain 2	12 MHz
H-Strain 3	27 MHz

Aniline gives similar results to the oxygen donors in terms of values for *g*, *D* and *E*. The value of *D* and *E* are slightly larger than the previous two examples. The *H*-strain 1 value is lower than that for the oxygen donors meaning that there is less coupling going on with the nuclei in the cyclen ring. This could mean that aniline causes less distortion.

3.4.7 DMSO.Gd.DOTAMPh

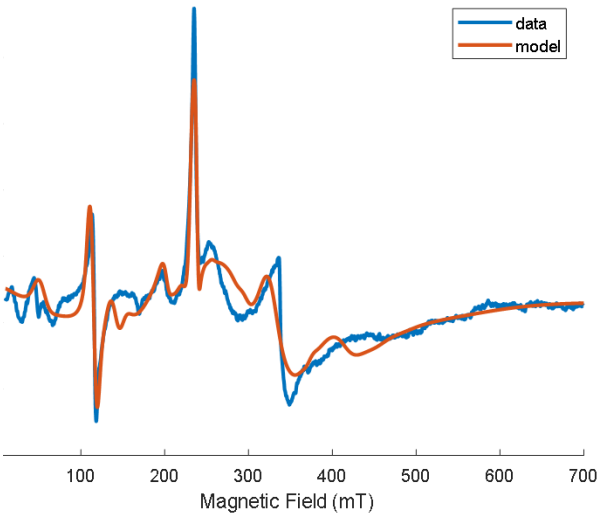

Figure 3.9: CW X-band frozen solution EPR spectrum of DMSO.Gd.DOTAMPh at 100 K, experimental (blue) and simulated (red), using the parameters in Table 3.7.

Table 3.7: Parameters obtained from non-linear least square regression model for benzyl DMSO.Gd.DOTAMPh at X-band.

g	2.004
D	-2131
E	-442
D-Strain	1526 MHz
E-Strain	268 MHz
H-Strain 1	135 MHz
H-Strain 2	127 MHz
H-Strain 3	55 MHz

On addition of DMSO to Gd.DOTAMPh there is a dramatic change to the form of the spectrum. *D* is very large and there are a number of interesting, well defined features to the spectrum. There is also a significant change in *g*-value to 2.004; the largest g-value of all the species. Two of the *H*-strain values are also relatively large suggesting potential structural distortion. The dominant features of the observed spectrum can be modelled well using the approach that worked well for other compounds. However, the quality of fit of the model to the observed spectra is significantly worse than that observed for the other cases described in this chapter. The disparity between the model and the observed spectrum suggests that the speciation or structure may be more complex in this system

than in the others. However, attempts to improve the fit by increasing the number of components in the did not yield significant improvement.

3.4.8 Fluoride.Gd.DOTAMPh

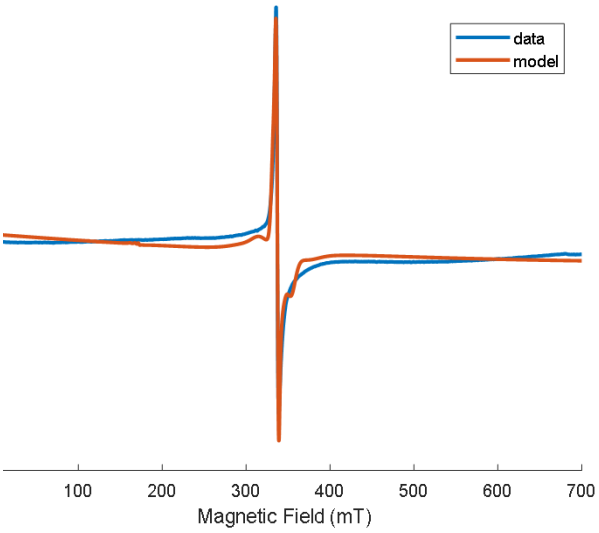

Figure 3.10: CW X-band frozen solution EPR spectrum of fluoride.Gd.DOTAMPh at 100 K, experimental (blue) and simulated (red), using the parameters in Table 3.8.

Table 3.8: Parameters obtained from non-linear least square regression model for fluoride.Gd.DOTAMPh at X-band.

g	1.987
D	-454 MHz
E	0 MHz
D-Strain	514 MHz
E-Strain	0 MHz
H-Strain 1	75 MHz
H-Strain 2	11 MHz
H-Strain 3	113 MHz

1 M TBAF in THF was added to give a 50 mM concentration of fluoride ions in solution. On addition of the fluoride, the spectrum became dramatically sharp and the *E* value became zero for the first time. The absence of an *E* value shows us a dramatic change to 'prolate' anisotropy with no rhombohedral distortion. This would occur as a result if there was higher symmetry present than for other bound ligands. There is now also no *E*-strain value and the *D* value is not particularly large in magnitude compared to other species.

However, the *D*-strain value is relatively large suggesting a broad distribution of values. Whilst the sharp feature was fitted very well by the software it struggled to incorporate the lack of distinguishable secondary features. The is one *H*-strain value larger than the others, however, this is a different *H*-Strain value to that of the oxygen donors which suggests that if there is a distortion it is different to these species in nature.

3.5 Q-Band Spectra

3.5.1 Gd.DOTAMPh

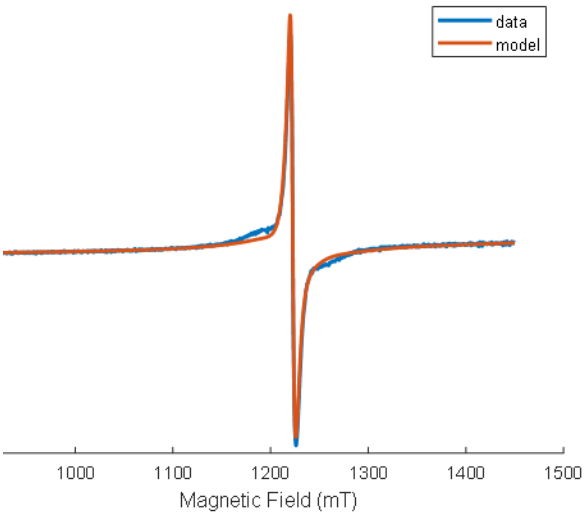

Figure 3.11: CW Q-band frozen solution EPR spectrum of Gd.DOTAMPh at 100 K, experimental (blue) and simulated (red), using the parameters in Table 3.9.

Table 3.9: Parameters obtained from non-linear least square regression model for Gd.DOTAMPh at Q-band.

g	1.989
D	-886 MHz
E	272 MHz
D-Strain	2020 MHz
E-Strain	434 MHz
H-Strain 1	0 MHz
H-Strain 2	0 MHz
H-Strain 3	0 MHz

This spectrum appears much sharper at Q-band. There is a difference in the *D* value between the X-band and Q-band fitting and the simulation struggled to pick up on the secondary features of the spectrum, focusing on fitting well the sharp central feature. This was also the case for the fitting of the fluoride spectrum at X-band and is a limitation of the software. Simultaneous fitting of both spectra using a global fit should help eradicate some of this bias. The *D*-strain value remains very large for this species suggesting a large distribution of values which could also potentially explain the discrepancy. A potential reason for this could be there were slight differences in the flash freezing process of the solution. The *H*-strain values are also all almost zero in this simulation which whilst they were small for X-band was not the case.

3.5.2 Benzylamine.Gd.DOTAMPh

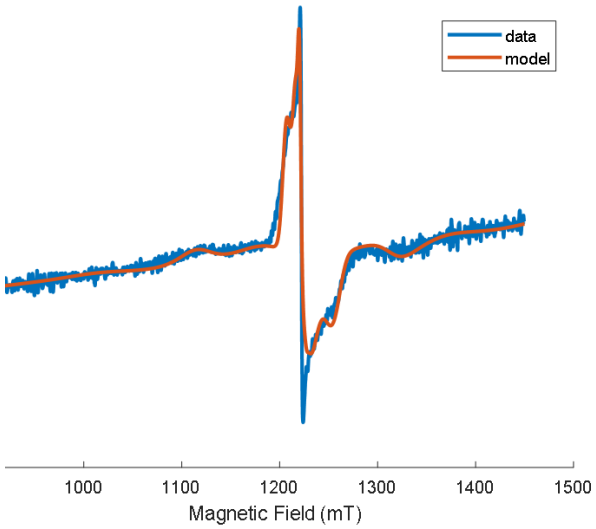

Figure 3.12: CW Q-band frozen solution EPR spectrum of benzylamine.Gd.DOTAMPh at 100 K, experimental (blue) and simulated (red), using the parameters in Table 3.10.

Table 3.10: Parameters obtained from non-linear least square regression model for benzylamine.Gd.DOTAMPh at Q-band.

g	1.989
D	-1463 MHz
E	623 MHz
D-Strain	419 MHz
E-Strain	333 MHz
H-Strain 1	0 MHz
H-Strain 2	0 MHz
H-Strain 3	76 MHz

Even at Q-band there are a number of distinct features to this spectrum and the software managed to fit the secondary features well. The model parameters are very similar here to the X-band with the exception of the *H*-strain values. The signal lacked intensity for the Q-band measurement, hence there may have been an overfitting of the noise within the spectrum.

3.5.3 Phenol.Gd.DOTAMPh

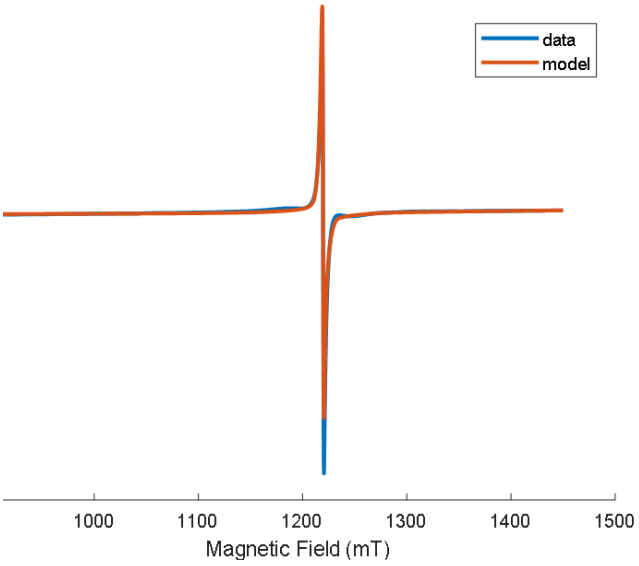

Figure 3.13: CW Q-band frozen solution EPR spectrum of phenol.Gd.DOTAMPh at 100 K, experimental (blue) and simulated (red), using the parameters in Table 3.11.

Table 3.11: Parameters obtained from non-linear least square regression model for phenol.Gd.DOTAMPh at Q-band.

g	1.990
D	-548 MHz
E	0 MHz
D-Strain	1337 MHz
E-Strain	119 MHz
H-Strain 1	81 MHz
H-Strain 2	18 MHz
H-Strain 3	20 MHz

The *E* value differs from X-band as here the *E* value is equal to 0. Although small, this was not the case for X-band. The other values a quite similar to that given for X-band.

The global fitting of the spectrum will help gain a more accurate value for these parameters. The main spectral feature remains sharp and is fitted well.

3.5.4 Benzoic acid.Gd.DOTAMPh

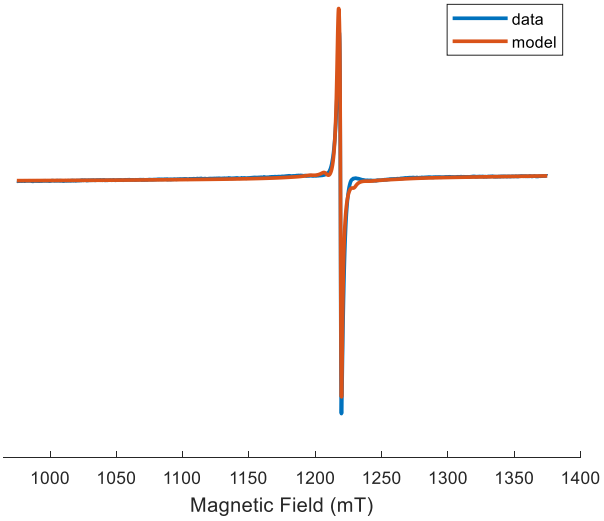

Figure 3.14: CW Q-band frozen solution EPR spectrum of benzoic acid.Gd.DOTAMPh at 100 K, experimental (blue) and simulated (red), using the parameters in Table 3.12.

Table 3.12: Parameters obtained from non-linear least square regression model for benzoic acid.Gd.DOTAMPh at Q-band.

g	1.991
D	-497 MHz
E	-148 MHz
D-Strain	1337 MHz
E-Strain	5 MHz
H-Strain 1	0 MHz
H-Strain 2	42 MHz
H-Strain 3	68 MHz

The model parameters are very similar here compared to the X-band. The main spectral feature remains sharp. The only difference is that of the *H*-Strain values which are still small but do not present one particularly larger value. The *D* values are similar although the *E* values are slightly larger than for X-band.

3.5.5 Benzylalcohol.Gd.DOTAMPh

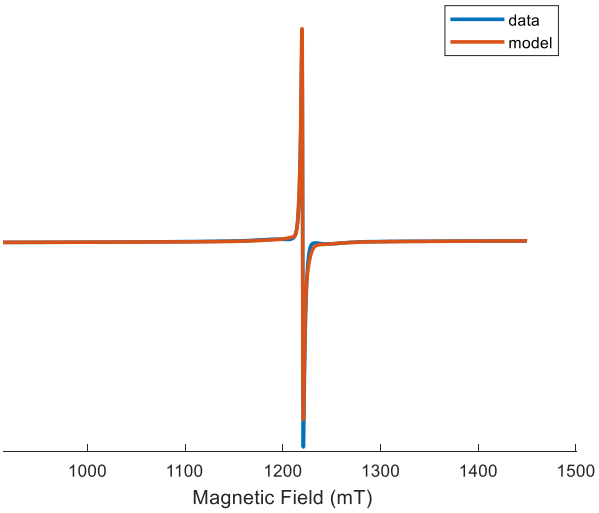

Figure 3.15: CW Q-band frozen solution EPR spectrum of benzylalcohol.Gd.DOTAMPh at 100 K, experimental (blue) and simulated (red), using the parameters in Table 3.13.

Table 3.13: Parameters obtained from non-linear least square regression model for benzylalcohol.Gd.DOTAMPh at Q-band.

g	1.990
D	-590 MHz
E	-91 MHz
D-Strain	1049 MHz
E-Strain	130 MHz
H-Strain 1	44 MHz
H-Strain 2	18 MHz
H-Strain 3	15 MHz

The model parameters are very similar here to the X-band and other oxygen donor species. The main spectral feature remains sharp and it is well fit. The *D*-strain value is rather large suggesting there is still a large distribution of possible values despite the spectral sharpness.

3.5.6 Aniline.Gd.DOTAMPh

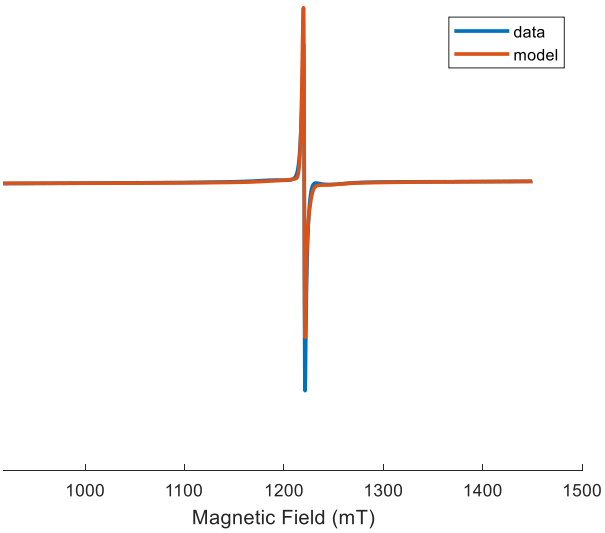

Figure 3.16: CW Q-band frozen solution EPR spectrum of aniline.Gd.DOTAMPh at 100 K, experimental (blue) and simulated (red), using the parameters in Table 3.14.

Table 3.14: Parameters obtained from non-linear least square regression model for Aniline.Gd.DOTAMPh at Q-band.

g	1.990
D	-584 MHz
E	-77 MHz
D-Strain	892 MHz
E-Strain	158 MHz
H-Strain 1	45 MHz
H-Strain 2	40 MHz
H-Strain 3	18 MHz

The model parameters are very similar here to the X-band values. The main spectral feature remains sharp. The difference between this species and the oxygen donors are again very subtle. However, the *D*-strain value is smaller meaning there is a smaller distribution of possible values when compared to the oxygen donors.

3.5.7 DMSO.Gd.DOTAMPh

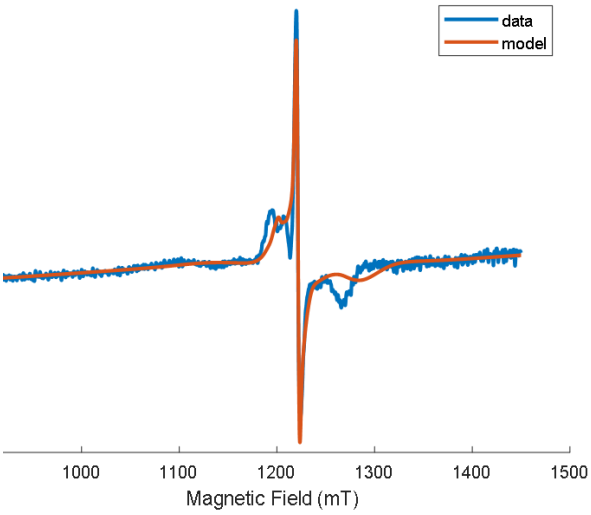

Figure 3.17: CW Q-band frozen solution EPR spectrum of DMSO.Gd.DOTAMPh at 100 K, experimental (blue) and simulated (red), using the parameters in Table 3.15.

Table 3.15: Parameters obtained from non-linear least square regression model for DMSO.Gd.DOTAMPh at Q-band.

g	1.990
D	-1882 MHz
E	-42.00 MHz
D-Strain	1906 MHz
E-strain	0 MHz
H-Strain 1	82 MHz
H-Strain 2	0 MHz
H-Strain 3	82 MHz

This spectrum proved difficult to fit at Q-band and more accurate values should be obtained when a global fitting is used. There are a number of features that are distinguishable at Q-band as well as at X-band. As with the X-band fitting of bound DMSO.Gd.DOTMAPh, there is significant divergence between the modelled spectrum and the observed one. As before, this suggests more complex speciation, which proved impossible to define further.

3.5.8 Fluoride.Gd.DOTAMPh

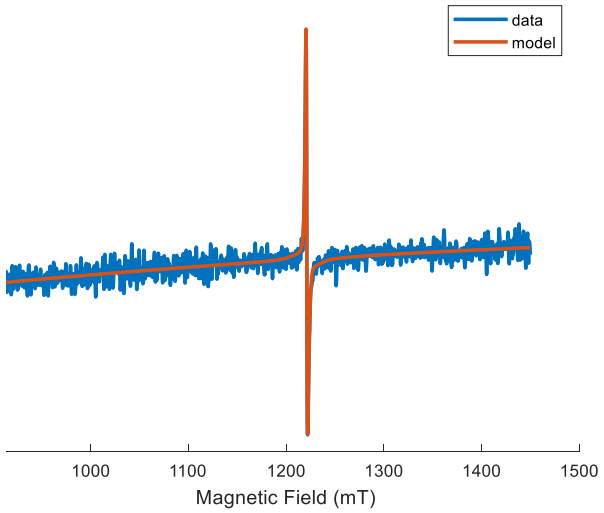

Figure 3.18: CW Q-band frozen solution EPR spectrum of fluoride.Gd.DOTAMPh at 100 K, experimental (blue) and simulated (red) using the parameters in Table 3.16.

Table 3.16: Parameters obtained from non-linear least square regression model for Fluoride.Gd.DOTAMPh at Q-band.

g	1.990
D	- 257 MHz
E	-16 MHz
D-Strain	480 MHz
E- Strain	14 MHz
H-Strain 1	69 MHz
H-Strain 2	12 MHz
H-Strain 3	139 MHz

The addition of fluoride once again gives an incredibly sharp feature. There is a very small *E* value given at Q-band, whereas this is zero for the X-band measurement. The spectrum was very low in intensity which made the data more difficult to fit due to noise. Despite this the large central feature was fitted well. However, there may be some features that are slightly hidden by the noise of the spectra. Whilst the *E*/*D* ratio remains similar due to the small size of *E*, the *D*-value is much smaller than that given for X-band. The *g*-value also differs somewhat. It will be good to gain a global fit to examine the anisotropy more accurately of this system by simultaneously fitting the two spectra.

3.6 Summary of Spectra

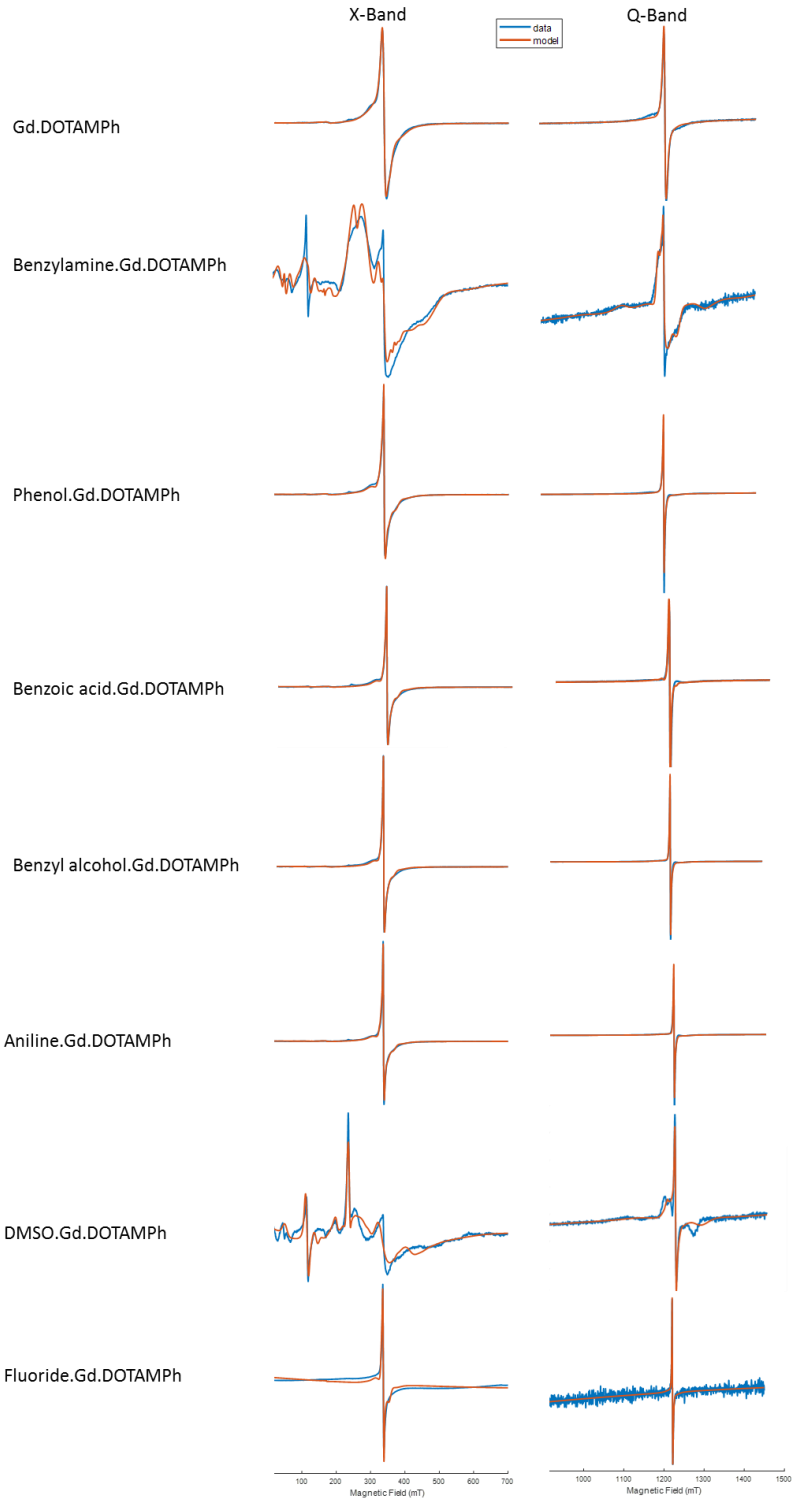

Figure 3.19: A summary of the spectra CW X-band and Q-band frozen solution EPR spectrum of the different species at 100 K, experimental (blue) and simulated (red).

The summary given in **Figure 3.19** shows that there is a large amount of variation in shape and number of features of the spectra depending on the axial donor ligand that is added to the system. This suggests that the electronic and magnetic properties can be dramatically changed depending on the local environment of our Gd(III).

The oxygen donors and aniline all show very similar shaped spectra. Phenol can be seen to be subtly different for both X-band and Q-band, this may be due to the oxygen being directly attached to the benzene ring. As a result, either the oxygen cannot reach the cavity quite as well or the lone pair of electrons might be less accessible due to resonance. This may also explain some of the subtle differences shown with aniline.

Both the fluoride.Gd.DOTAMPh spectra show a single large central feature which may be explained by the small *D* value and minimization of an *E* value. In other words, we can see the system has tends to prolate anisotropy.

Both DMSO and benzylamine give very interesting spectra. This is ultimately due to the large D value and relatively large *E*/*D* ratio given for both. However, it is also the subtle difference in these values that make the spectra look so different from one another.

3.7 Global Fitting

After the X-band and Q-band spectra were individually fitted, a global fit was established of the two spectra. This is where the two spectra are normalised and concatenated together. They were then fitted simultaneously by the EasySpin® package with initial estimates established using the individual fittings. The parameters *g*, *D* and *E* were

extracted using this method to give us a better look at the anisotropy of the system. An approximate *E*/*D* ratio was also calculated to establish a relative measure of anisotropy of the system. These values are shown in **Table 3.17**. An example of a spectra fit by the global fit method is given for context in **Figure 3.20**.

Table 3.17: Fitting parameters obtained for simulation of frozen solution (100 K) X-band and Q-band CW EPR spectra of the different species, using a global fitting method (see text for details).

Species	*g*	*D*(MHz)	*E*(MHz)	*E*/*D* ratio	Anisotropy of the system
Gd.DOTAMPh	1.987	-795	222	~1/4	Rhombohedral distortion from prolate
Benzylamine.Gd.DOTAMPh	1.995	-1418	-667	~1/3	Maximum rhombohedral distortion from prolate
Phenol.Gd.DOTAMPh	1.989	-457	91	~1/5	Rhombohedral distortion from prolate
Benzoic acid.Gd.DOTAMPh	1.989	-584	96	~1/6	Slight rhombohedral distortion from prolate
Benzyl alcohol.Gd.DOTAMPh	1.990	-548	89	~1/6	Slight rhombohedral distortion from prolate
Aniline.Gd.DOTAMPh	1.987	535	82	~1/6	Slight rhombohedral distortion from prolate
DMSO.Gd.DOTAMPh	2.006	-1822	542	~1/4	Rhombohedral distortion from prolate
Fluoride.Gd.DOTAMPh	1.985	-354	0	0	Prolate anisotropy

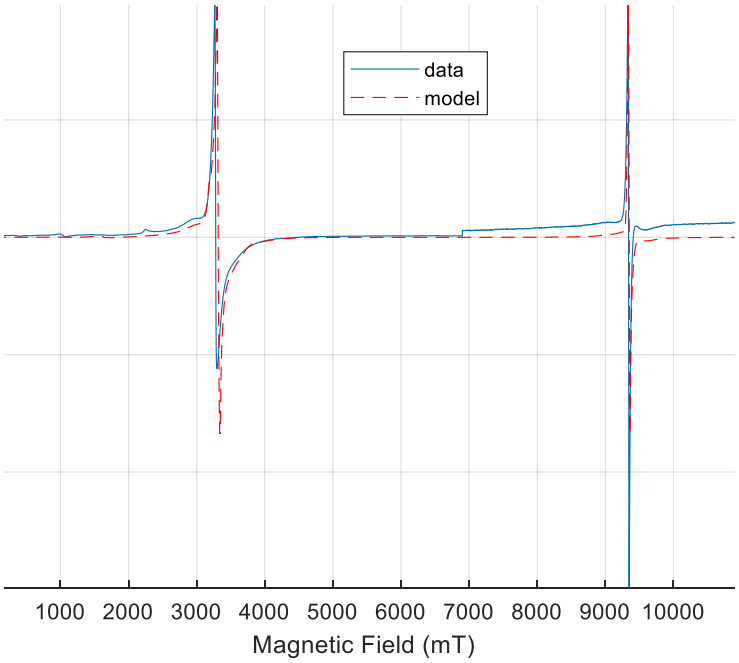

Figure 3.20: Spectra of frozen solution (100 K) X-band and Q-band CW EPR spectra of the benzoic acid.Gd.DOTAMPh as an example of using a global fitting method (see text for details).

3.8 Discussion of Global Fitting Results

The variation in parameters shows that the anisotropy of the system can be controlled by binding different ligands into the 9th coordination site. There is a significant change in magnitude of *D* and *E* as well as *E*/*D* ratio depending on the species. The most dramatic change is when fluoride is added and the system adopts complete 'prolate' anisotropy.

There potentially is a loose correlation between ligand field theory and the anisotropy of the system as fluoride is a weak field ligand and benzylamine a strong field ligand **Figure 3.21**. These findings may suggest that the weak field ligands encourage prolate anisotropy whereas strong field ligands encourage a rhombohedral distortion. There could also be a correlation due to the charge of the species i.e. as the donor becomes more 'charged' there

is a greater increase in the symmetry of the system. However, this could be coincidental and the dependence could actually be based more on where the ligand sits above the cavity. Fluoride is small, so may be able to access the Gd(III) more readily. The actual values could be a combination of both these factors or other factors.

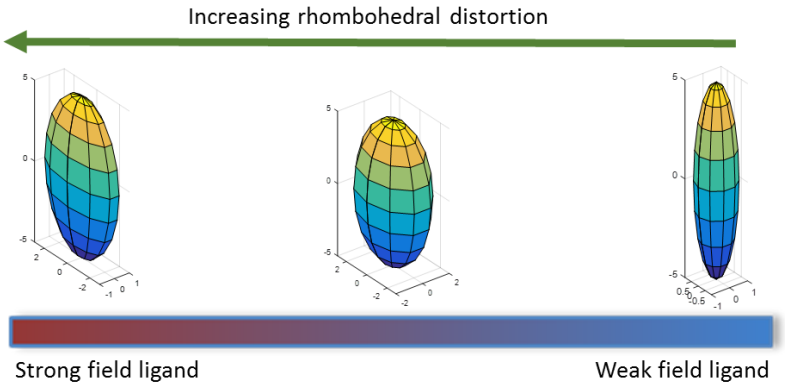

Figure 3.21: Schematic showing possible reasoning for change in anisotropy due to ligand field theory.

As well as the changes in *D* and *E*, there is also a huge variation in the *g*-value of the species. DMSO.Gd.DOTAMPh gives a *g*-value of 2.006 whereas fluoride.Gd.DOTAMPh is 1.985. Such a large variation in *g*-value is important for future application to DNP MRI.

3.9 The Contribution of Different Transitions between M_S States

Once parameters have been obtained, it is possible to simulate the individual contributions from different transitions. This has been completed for Gd.DOTAMPh and for the benzylamine.Gd.DOTAMPh species at X-band **Figure 3.22** and **Figure 3.24**. Transition maps can also be simulated using the EasySpin® in Matlab®. These can be

used to observe where the allowed transitions have occurred, and the extent of transition crossing can be seen as a result of anisotropy and the *D* and *E* values (**Figure 3.23** and **Figure 3.25**). A more detailed explanation of these forms of spectra is given in **Chapter 1** where their forms can also be compared with the simulated example given of a $D < 0$ and $E \neq 0$ system. For allowed transitions the selection rule is $\Delta M_S = \pm 1$.

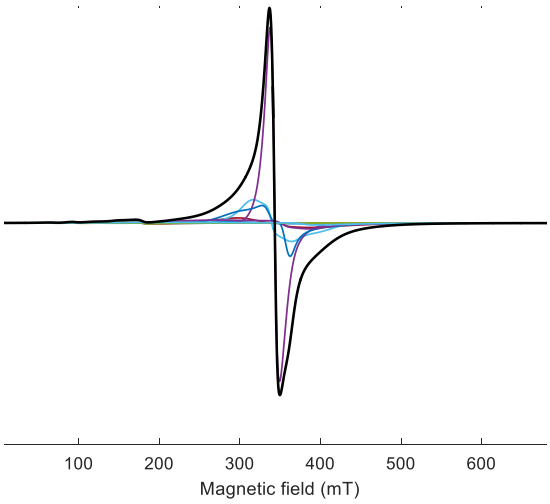

Figure 3.22: The simulated different transitions within the species Gd.DOTAMPh. The black line indicates the sum of these transitions and gives rise to the overall spectrum and the purple line shows the dominant $\Delta M_s = -1/2 \rightarrow \Delta M_s = +1/2$ transition. The other allowed transitions are much less dominant and are shown in the other colours.

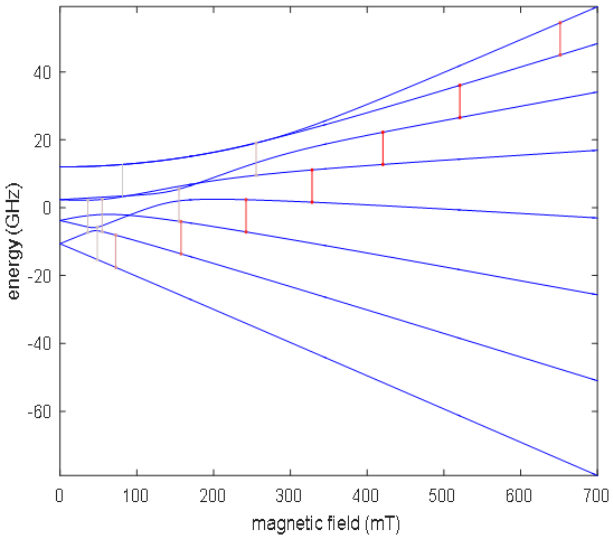

Figure 3.23: A transition map to show the forbidden (grey) and allowed transitions (red) occurring within the species Gd.DOTAMPh.

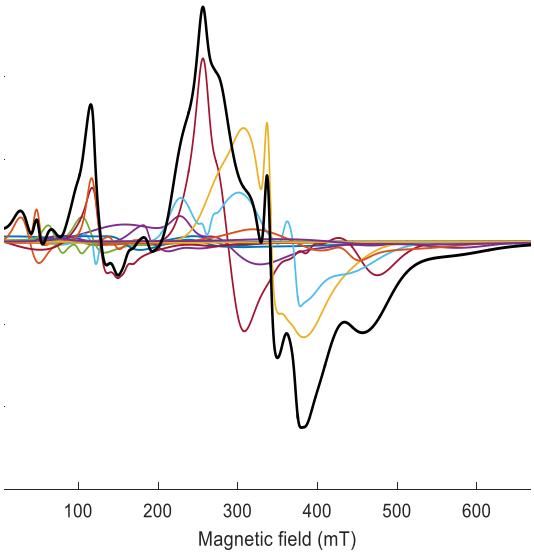

Figure 3.24: The simulated different transitions within the species benzylamine.Gd.DOTAMPh. The black line indicates the sum of these transitions and gives rise to the overall spectrum. The red line shows the $\Delta M_s = -3/2 \rightarrow \Delta M_s = -1/2$ transition which is the dominant transition. The yellow line shows the $\Delta M_s = -1/2 \rightarrow \Delta M_s = +1/2$ transition which also is a highly populated transition. The other transitions are much weaker and make up the other colours.

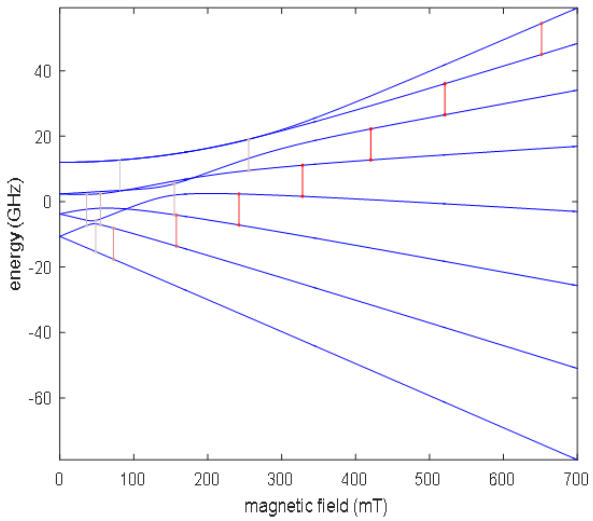

Figure 3.25: A transition map to show the forbidden (grey) and allowed transitions (red) occurring within the species benzylamine.Gd.DOTAMPh.

When comparing the bound benzylamine.Gd.DOTAMPh and unbound Gd.DOTAMPh it is clear that increasing the magnetic field affects the allowed transitions far more for the latter than for the former species. The result is a large difference in the shape and features of the two spectra which is ultimately due to the summation of their allowed transitions.

From the transition maps it is possible to see that for Gd.DOTAMPh the biggest contribution to the overall spectrum is the $\Delta M_s = -1/2 \rightarrow \Delta M_s = +1/2$. However, for benzylamine.Gd.DOTAMPh the biggest contribution comes from the $\Delta M_s = -3/2 \rightarrow \Delta M_s = -1/2$. This shows that changing the ligand can have a significant impact on which transitions dominate which dramatically changes the shape of spectrum.

3.10 The PEANUT Experiment

Conventional EPR can struggle to separate overlapping or broadened transitions. As a result two dimensional phase-inverted echo-amplitude detected nutation (PEANUT) is a powerful tool for analysing and interpreting EPR spectra. [8] A schematic of the pulse sequence used for this experiment is shown in **Figure 3.26**. In the experiment, a 90° pulse is applied and then the system is allowed to partially relax. A high turning angle pulse is applied for a period of time followed by the a pulse of the same magnitude but the opposite phase (-x). The overall result is that the different M_S states undergo nutation a different rates which can be distinguished when looking at the transitions between different M_S states.

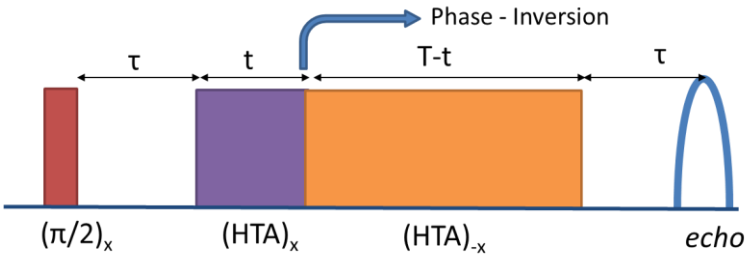

Figure 3.26: Schematic diagram showing pulse sequence of PEANUT experiment.

This experiment can correlate nutation frequency of EPR transitions with the fields at which they occur. The nutation frequency of a given transition depends on the total spin quantum number, *S*, the microwave frequency, ω_1 and the projection quantum numbers, M_S involved in the transitions **Equation 3.3**.

$$\omega_{TN} = \sqrt{[S(S+1) - M_s M_s']}\omega_1 \qquad \textit{Equation 3.3}$$

The allowed transitions are $\Delta M_S = \pm 1$ which gives us the values at different fields. Depending on the number of transitions, the relative ratios can be calculated between the different transitions and checked if this is correct for the species present.

3.11 PEANUT and Pulsed Experiments

It was decided to measure spectra using Q-band (34 GHz) frequencies at 10 K using pulsed-EPR experiments such as PEANUT in order to further explore the properties of the benzylamine.Gd.DOTAMPh species (**Figure 3.27**). Initially a field sweep EPR echo detected spectra was taken (**Figure 3.30**). The dominant Gd.DOTAMPh with benzylamine species was observed, and it was possible to use the knowledge already

obtained to assign the turning points of the transitions. The large zero field splitting parameters for this complex allowed a PEANUT experiment, a pulsed EPR experiment, (see **Figure 3.25** for pulse sequence) to be used to identify the different transitions between spin manifolds . [8]

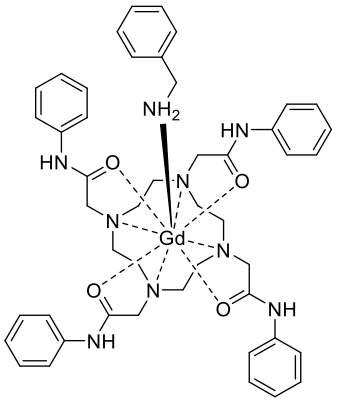

Figure 3.27: Schematic structure of benzylamine.Gd.DOTAMPh. Note: the charge is not shown.

Four prominent transitions were observed with different relative nutation frequencies (ω_{TN}) (**Figure 3.28** and **Figure 3.29**). The ratios between the transitions are consistent with that expected for the Gd(III) ion and able to be seen due to the anisotropy relative to the free ion. This shows that there is indeed only one species present within our frozen solution. We can now also assign our different turning points within our spectra and show what transition contributes to them (**Figure 3.29**).

The experiment shows that the most dominant transition is now the $\Delta M_s = -1/2 \rightarrow M_s = +1/2$ closely followed by the $\Delta M_s = -3/2 \rightarrow \Delta M_s = -1/2$ which is now the case because the conditions are at Q-band rather than at X-band and this will mean that while the *g*, *D* and *E* parameters should remain the same, the frequency at which the different transitions come into resonance will be different. This is why X-band and Q-band spectra look different.

The demonstration that experiments such as these are possible for these complexes will be useful for future work involving multiple Gd(III) centres or potnetially multiple Gd(III) species. If the spin manifolds for two centres can be individually assigned, this may help us to gain further understanding of the magnetic properties and behaviour of these novel systems.

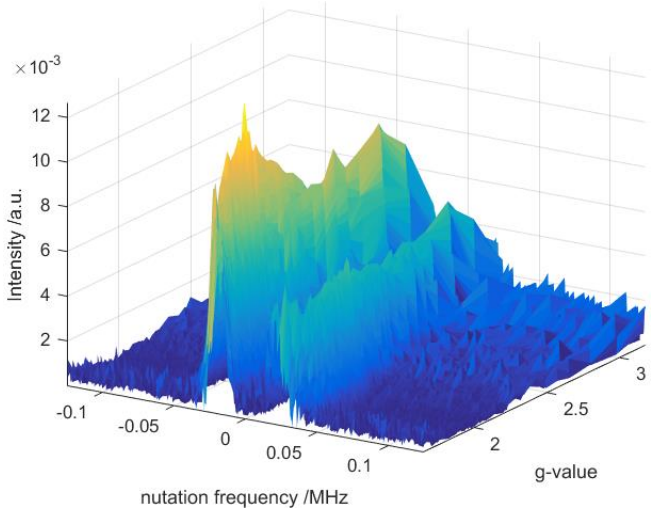

Figure 3.28: The overall results of the PEANUT experiment on Gd.DOTAMPh with benzylamine. Nutation frequency is plotted against intensity for different values of *g*-value.

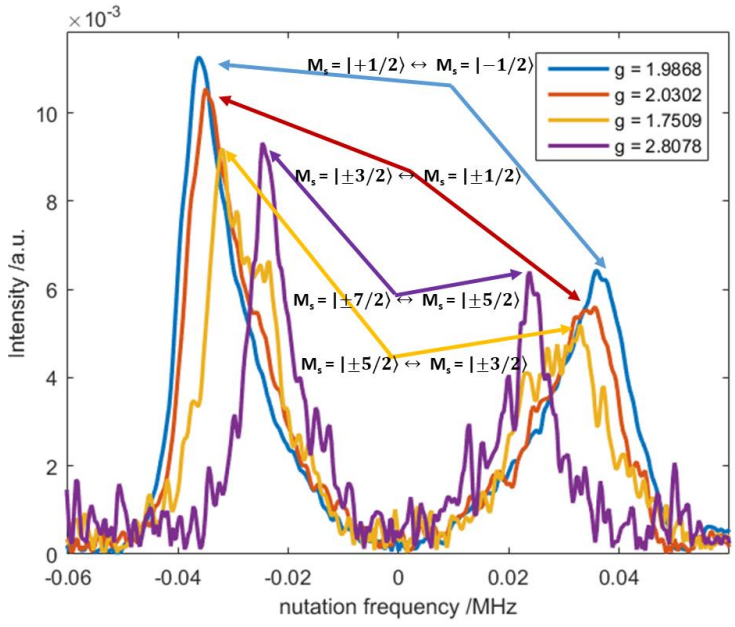

Figure 3.29: Key 2D slices from **Figure 3.19** that show 4 nutation frequency transitions and therefore the spin manifolds of the benzylamine.Gd.DOTAMPh.

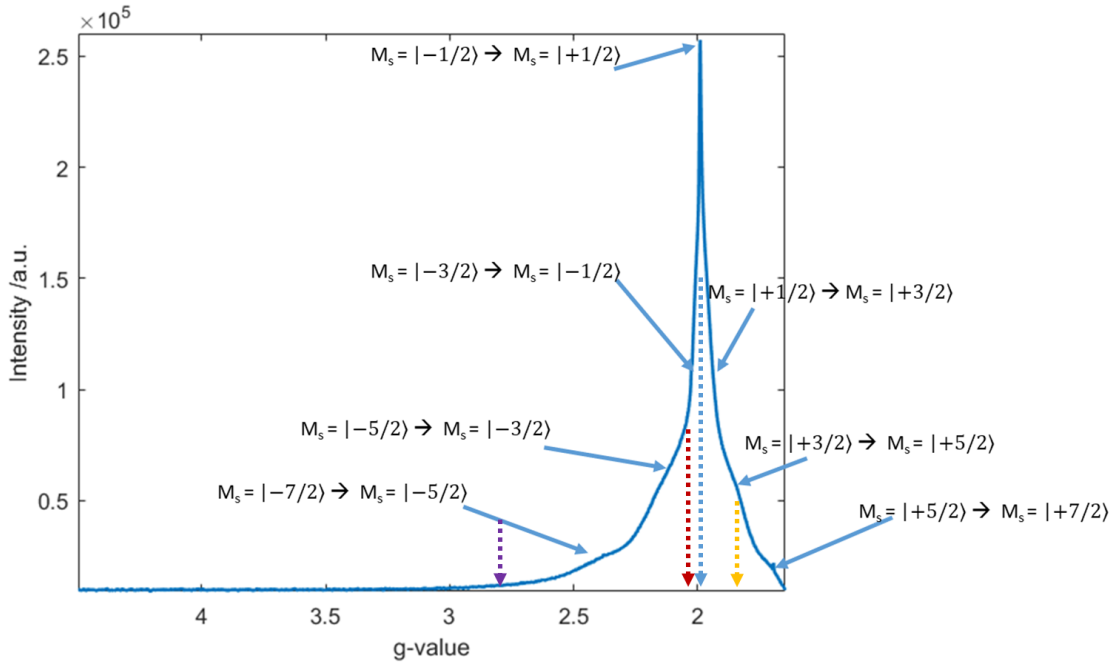

Figure 3.30: Q-band field sweep EPR echo detected spectra of benzylamine.Gd.DOTAMPh. .Blue arrows indicate positions of transitions within the Gd.DOTAMPh with benzylamine species spectrum. Coloured dotted arrows indicate the field values at which PEANUT experiments were recorded.

3.12 Luminescence Binding Studies

Binding studies were undertaken to observe how tightly donor species would bind to the ninth available axial coordination site to observe how the ligand field was affected. The Gadolinium(III) complex was not used in the luminescence binding studies. Gd(III) has completely half-filled 4*f* shells which leads to not only the transitions being Laporte forbidden but a spin-flip is also needed to make the transition possible due to the Pauli Exclusion Principle. As a result, the following study was undertaken using europium(III) analogues. Eu(III) was chosen due to its similarity in size, magnetism and because it is next to gadolinium in the periodic table.

On addition of benzylamine to Eu.DOTAMPh in 5:3 MeCN:^{t}BuOH by volume was a marked decrease in the intensity of the luminescence. From 0 to 1.25 equivalents the change in both the ΔJ = 1 and ΔJ = 2 transition changed drastically for europium emission **Figure 3.31**. The initial concentration of Eu.DOTAMPh was held constant at 2 x 10^{-5} M. The sample was excited at 270 nm.

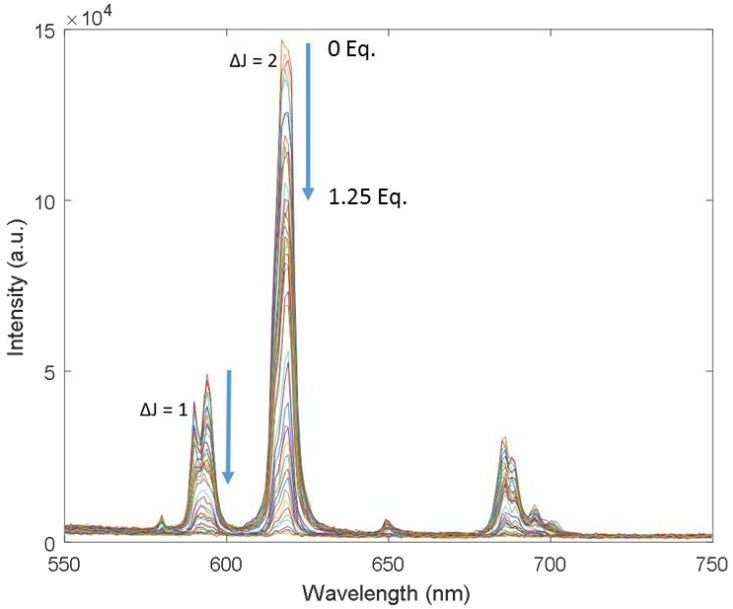

Figure 3.31. Emission Spectra for Eu.DOTAMPh showing the titration with Benzylamine from 0 equivalents to 1.25 equivalents.

The change was more pronounced for the hypersensitive Δ*J* = 2 transition and as a consequence there was also a marked change in the Δ*J* = 2 / ΔJ = 1 ratio. On increasing addition of benzylamine it can also be seen that the Δ*J* = 1 and ΔJ = 2 transitions changes in shape. This is consistent with there being a change in the ligand field splitting parameters on addition of benzylamine.

The K_a value for the system is 4.70 (±0.99) x 10^6 M^{-1} and obtained through luminescence titrations and using DynaFit® software which modelled the data using the ΔJ = 2 / ΔJ = 1 ratio **Figure 3.32**. [9] The data implies there is single binding event where the

benzylamine associates or dissociates with the 9th coordination site **Figure 3.32** and **Figure 3.33**.

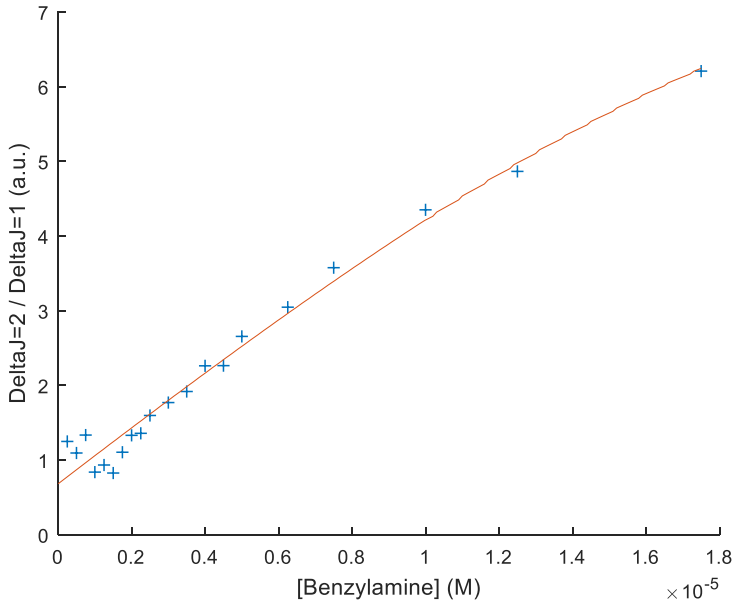

Figure 3.32: A plot of the change in the ratio of the ΔJ=2/ΔJ=1 transition intensity as a function of initial benzylamine concentration as titrated into Eu.DOTAMPh. The initial concentration of Eu.DOTAMPh was kept constant at 0.00002 M. The blue crosses indicate data and the red line is the model as described in the text.

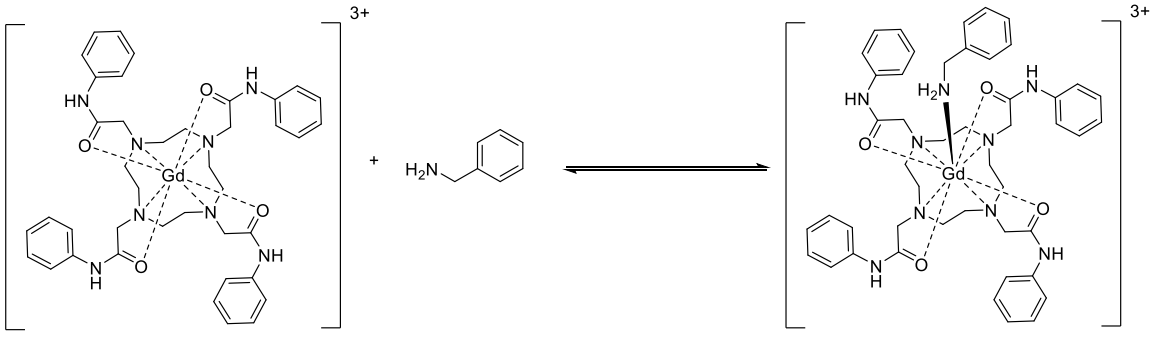

Figure 3.33: The equilibrium between bound and unbound Eu.DOTAMPh with benzylamine.

3.13 Conclusions to Chapter

This chapter has shown that *D* and *E* as well as *E*/*D* ratio can be varied hugely by ligation. The change in some cases is so great that we can completely change the form of our spectrum by changing the most dominant allowed transition.

In a crystal field model, both g-value and the ZFS splitting parameters are a result of the mixing of excited states into the ground state, and the form of that mixing is similar for both However, the effect is much greater for the splitting parameters than for the g-value. *D* and *E* for these systems change greatly and the *g*-value of the system also changes. We can therefore manipulate *g*-value by ligation which is essential in the application of DNP MRI. We need to be able to tune the *g*-values of two radical centers so that their difference in *g*-value is on the order of magnitude of the Larmor frequency of the nucleus we are trying to hyperpolarize. This is essential for the cross-effect mechanism to take place to enable DNP.

The fact that *E* and *D* can be manipulated is also of interest for potential future contrast agent design as it shows that the local environment the Gd(III) is held in is important. A better understanding of this will enable us to design more effective contrast agents for future use.

By using techniques such as PEANUT we can potentially determine the environments of polynuclear gadolinium(III) centered complexes and samples containing multiple gadolinium species.

This chapter demonstrates novel fundamental work that will be used as a foundation to build upon for application of metallodrugs for biomedical imaging techniques. It shows that crystal field effects are important for Gd(III) complexes. Understanding these effects are essential to developing contrast media for MRI and DNP MRI electron polarization agents and optimizing their effectiveness.

3.14 References

[1] O. A. Blackburn, R. M. Edkins, S. Faulkner, A. M. Kenwright, D. Parker, N. J. Rogers and S. Shuveav, Dalton Trans., vol. 45, pp. 6782-6800, 2016.

[2] O. A. Blackburn, N. F. Chilton, K. Keller, C. E. Tait, W. K. Myers, E. J. L. McInnes, A. M. Kenwright, P. D. Beer, C. R. Timmel and S. Faulkner, Angew. Chem. Int. Ed., vol. 54, pp. 10783-10786, 2015.

[3] L. Di Bari, G. Pintacuda, P. Salvadori, R. S. Dickens and D. Parker, J. Am. Chem. Soc., vol. 128, no. 38, pp. 9257-9264, 2000.

[4] S. Stoll and A. Schweiger, J. Magn. Reson., vol. 178, pp. 42-55, 2006.

[5] K. J. Miller, A. A. Saherwala, B. C. Webber, Y. Wu, A. D. Sherry and M. Woods, Inorg. Chem., vol. 49, pp. 8662-8664, 2010.

[6] J. A. Clayton, K. Keller, M. Qi, J. Wegner, K. Vanessa, H. Hintz, A. Godt, S. Han, G. Jeschke, M. S. Sherwin and M. Yulikov, Phys. Chem. Chem. Phys. , vol. 20, pp. 10470-10492, 2018.

[7] M. Benmelouka, J. Van Tol, A. Borel, S. Nellutla, M. Port, L. Helm, L.-C. Brunel and A. E. Merbach, Helv. Chim. Acta., vol. 92, pp. 2173-2185, 2009.

[8] S. Stoll, G. Jeschke, M. Willer and A. Schweiger, J. Magn. Reson., vol. 130, pp. 86-96, 1998.

[9] P. Kuzmic, Anal. Biochem., no. 237, pp. 260-273, 1996.

4 Using EPR to Explore Broken Symmetry Systems

4.1 Introduction

Once EPR of a C_4 symmetric complexes and their binding to various ligands had been explored using Gd.DOTAMPh, the EPR properties of Gd.pDO3A were explored. This was to partially test if the same approach could be applied to a non-C_4 symmetric system. The complex was dissolved in 65:35 water:glycerol mixture by volume to give a 5 mM solution. A MeCN:^{t}BuOH solvent mixture could no longer be used due to solubility issues with the complex. The complex was found to be highly soluble in the new solvent system. This solvent system has the advantage that it is already used in DNP MRI imaging as it forms a glass at low temperatures and is also non-toxic *in vivo*. [1] This could improve the application potential of the project. Measurements of the initial complex were initially taken using CW EPR using X-band (9 GHz) frequencies at 100 K and the ligands added were 100 equivalents (500 mM). These were then followed by Q-band (34 GHz) CW EPR also at 100 K using identical samples.

The macrocycle is a heptadentate ligand leaving two sites in which other ligands can bind; namely an equatorial site and an axial site **Figure 4.1**. The binding of the different ligands added will affect the ligand field splitting parameters in the form of *D* and *E*, subsequently leading to a potential change in *g*-value.

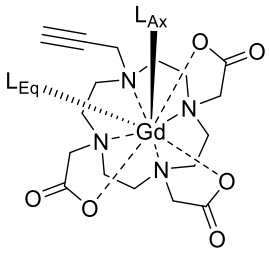

Figure 4.1: Schematic showing the potential equatorial and axial binding site of Gd.pDO3A

4.2 Experimental Conditions for CW EPR

As in **Chapter 3**, measurements were initially taken using CW EPR using X-band (9 GHz) frequencies followed by Q-band (34 GHz) at 100 K. Measurements were performed on a Bruker Biospin EMX spectrometer equipped with a high sensitivity Bruker probe head and an Oxford Instruments helium-flow cryostat. Modulation amplitudes and frequencies of 0.01 mT and 100 kHz, were used, respectively. The microwave power was adjusted in order to avoid spectral distortions.

4.3 Computational Analysis of Results

The spectra were processed using MATLAB® and EasySpin® software. [2] For the frozen solution CW EPR data the *pepper* function was used. [3] After the spectra were processed, using the software, parameters were extracted by fitting the real spectra using a non-linear least squares regression model where an overall RMSD value for the entire system is minimized to as close to zero as possible. Using the parameters extracted from the simulations, model spectra can be produced.

To obtain the best fit possible using the software, initial reasonable values are first approximated and simulated to see if they gave a model spectra with a similar profile and features to the data. After this has been established as a reasonable fit the simulation is undertaken for a set period before the results are examined. If the values are converging to a certain value and the model looks progressively like the data, then the simulation can be allowed to run until the software accesses that the best possible values have been reached. If it is clear that this is not the case or that for certain parameters, the values are converging far too slowly then the model with the initial values set for parameters will have to be adapted and reassessed.

Two different models were used to simulate the data. The first model was the same as the model used to fit the various Gd.DOTAMPh species spectra. In **Chapter 3** it was assumed there was one isomer present (distorted SAP). As discussed in **Chapter 2** this is not the case for Gd.pDO3A and the NMR shows both the SAP and TSAP isomers. This model also does not take into account the potential complexity added by equatorial and axial binding of different ligands. However, the model is relatively simple and the variations in *D* and *E* can to a certain degree be taken into account with the *D*-strain and *E*-strain values. The second model tested used the same parameters as the first but assumed that there were two major components to be fitted i.e. the two species accounting for the SAP and TSAP isomers. The *g*-value was still assumed to be isotropic due to the nature of the Gd(III) ground state.

4.4 One Component X-Band Fitting

4.4.1 Gd.pDO3A

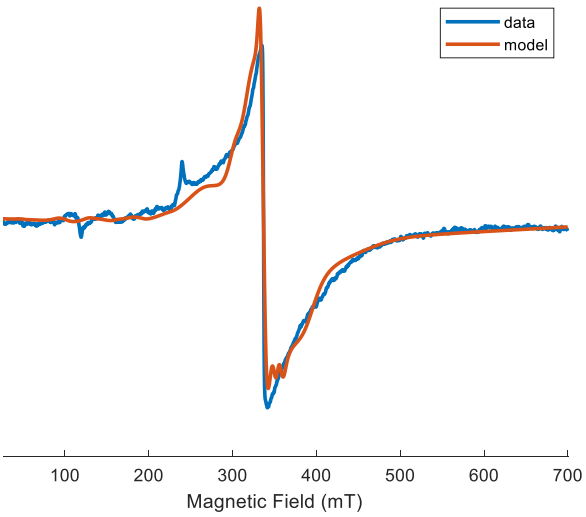

Figure 4.2: CW X-band frozen solution EPR spectrum of Gd.pDO3A at 100 K, experimental (blue) and simulated (red), using the parameters in Table 4.1.

Table 4.1: Parameters obtained from non-linear least square regression model at X-band.

g	2.002
D	-1112 MHz
E	157 MHz
D-Strain	1183 MHz
E-Strain	207 MHz
H-Strain 1	3 MHz
H-Strain 2	4 MHz
H-Strain 3	107 MHz

The EPR spectra of Gd.pDO3A proved far more difficult to model than Gd.DOTAMPh. Whilst the central feature is relatively well fitted the secondary features are not well registered. The *g*-value is around 2, which is a sensible value for Gd(III) complexes. The *D*-strain and *E*-strain values were about the same size as the *D* and *E* values themselves which suggest that there is a huge range of potential *D* and *E* values. This implies a potential flaw in the model. *H*-strain 3 is significantly larger than that of *H*-strain 1 and 2 suggesting the complex is potentially distorted in one direction suggesting that it may be to the nitrogen atoms and other nuclei in one direction more strongly than the others.

4.4.2 Benzylamine.Gd.pDO3A

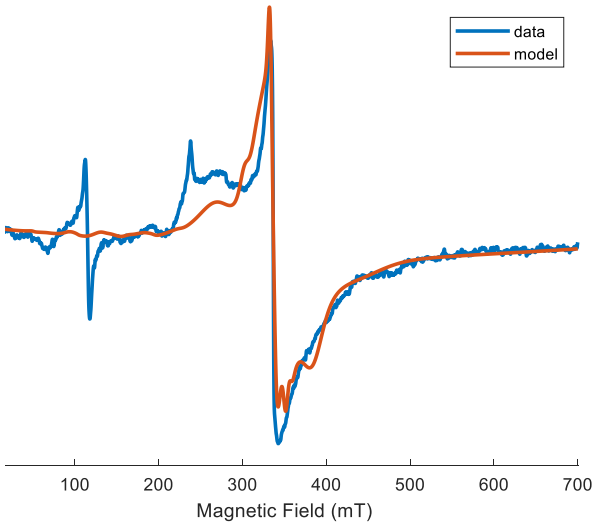

Figure 4.3: CW X-band frozen solution EPR spectrum of benzylamine.Gd.pDO3A at 100 K, experimental (blue) and simulated (red), using the parameters in Table 4.2.

Table 4.2: Parameters obtained from non-linear least square regression model for benzylamine.Gd.pDO3A at X-band.

g	2.003
D	-1131
E	158 MHz
D-Strain	110 MHz
E-Strain	330 MHz
H-Strain 1	1 MHz
H-Strain 2	1 MHz
H-Strain 3	107 MHz

The fitting proved even worse for benzylamine.Gd.pDO3A in comparison to Gd.pDO3A. The secondary features are poorly modelled. As a result, the size of the *D* and *E* values are comparable to Gd.pDO3A. The same pattern is also observed for the *H*-strain values. There is very little change in the *g*-value.

4.4.3 Phenol.Gd.pDO3A

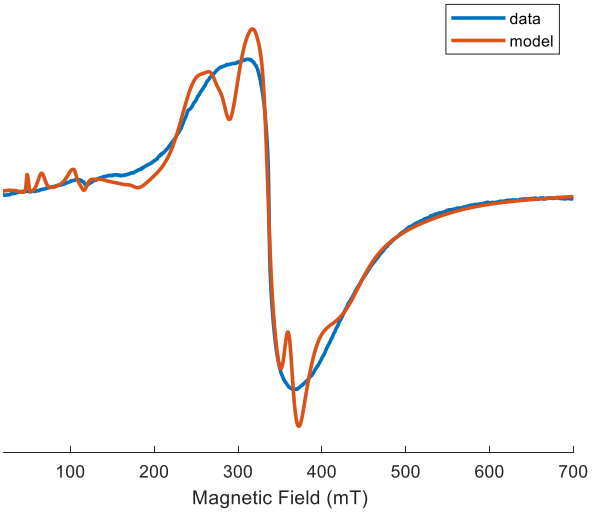

Figure 4.4: CW X-band frozen solution EPR spectrum of phenol.Gd.pDO3A at 100 K, experimental (blue) and simulated (red), using the parameters in Table 4.3.

Table 4.3: Parameters obtained from non-linear least square regression model for phenol.Gd.pDO3A at X-band.

g	2.001
D	-1525 MHz
E	310 MHz
D-Strain	1332 MHz
E-Strain	361 MHz
H-Strain 1	150 MHz
H-Strain 2	148 MHz
H-Strain 3	0 MHz

The spectrum distinctly changes form upon addition of phenol and the central feature greatly broadens. The model struggles to cope with the broadening of the central feature. It compensates by introducing potential additional features. The *D* and *E*-values also increase in magnitude. The distribution of *H*-values also completely changes with larger values for *H*-strain 1 and 2 with a value of zero for *H*-strain 3. This could suggest a significant change in shape upon binding of phenol. There are still issues with the magnitude of the *D*-strain and *E*-strain values.

4.4.4 DMSO.Gd.pDO3A

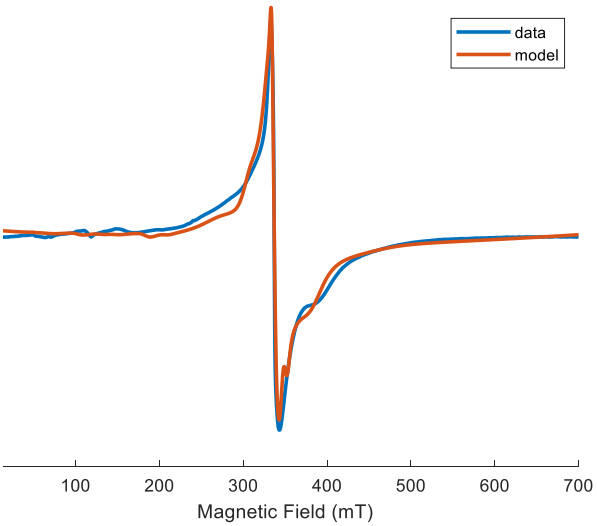

Figure 4.5: CW X-band frozen solution EPR spectrum of DMSO.Gd.pDO3A at 100 K, experimental (blue) and simulated (red), using the parameters in Table 4.4.

Table 4.4: Parameters obtained from non-linear least square regression model for benzyl DMSO.Gd.pDO3A at X-band.

g	1.997
D	-959 MHz
E	-152 MHz
D-Strain	1246 MHz
E-Strain	150 MHz
H-Strain 1	65 MHz
H-Strain 2	27 MHz
H-Strain 3	66 MHz

Upon addition of DMSO the central feature of the spectrum sharpens in comparison to Gd.pDO3A. There are also fewer secondary features. This proved much easier for the model to fit and acknowledges better the secondary features for instance the one at 400 mT. There is a significant change in *g*-value, the *D* value has decreased and there is a larger *E*/*D* ratio than Gd.pDO3A. The *H*-strain values are also more evenly distributed. However, the issues with *D*-strain and *E*-strain are still large and this is not yet resolved.

4.5 One Component Q-band Fitting

4.5.1 Gd.pDO3A

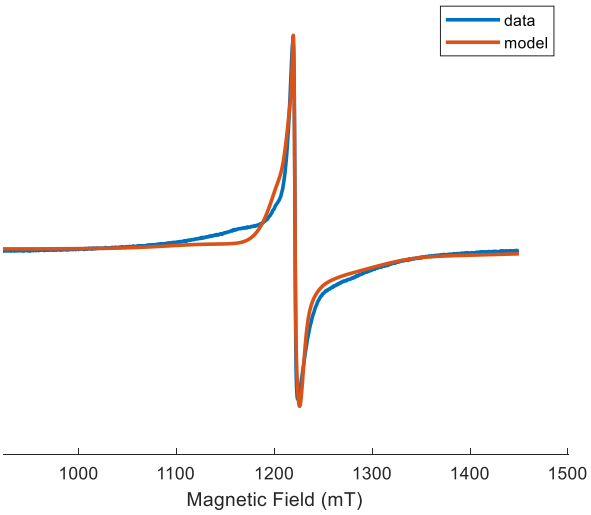

Figure 4.6: CW Q-band frozen solution EPR spectrum of Gd.pDO3A at 100 K, experimental (blue) and simulated (red), using the parameters in Table 4.5.

Table 4.5: Parameters obtained from non-linear least square regression model for Gd.pDO3A at Q-band.

g	1.990
D	-1785 MHz
E	218 MHz
D-Strain	2283 MHz
E-Strain	310 MHz
H-Strain 1	28 MHz
H-Strain 2	0 MHz
H-Strain 3	0 MHz

It was easier to fit the Q-band spectrum for Gd.pDO3A than for the X-band spectrum. However, the fit is still not entirely adequate. To the right of the feature at 1200 mT the fit is far better than to the left of 1200 mT. The *g*-value is significantly different to that of the X-band data though the *D* and *E*-values are similar order of magnitude. The *H*-strain 3 value is also very different from the X-band data suggesting that the coupling differs with other nuclei. This suggests that a one component model may not be ideal to fit the data and another model is needed.

4.5.2 Benzylamine.Gd.pDO3A

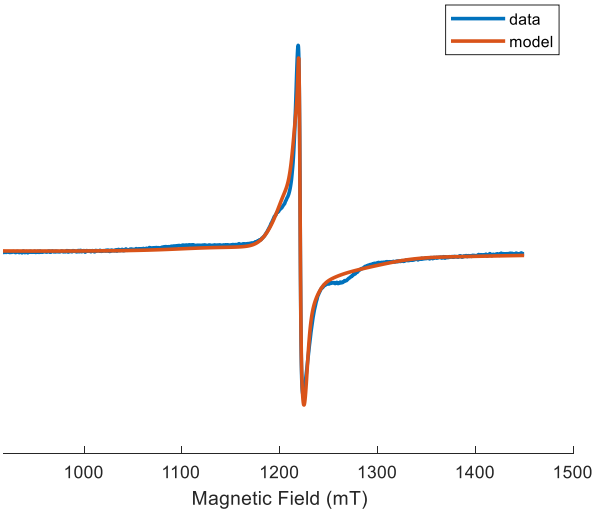

Figure 4.7: CW Q-band frozen solution EPR spectrum of benzylamine.Gd.pDO3A at 100 K, experimental (blue) and simulated (red), using the parameters in Table 4.6.

Table 4.6: Parameters obtained from non-linear least square regression model for benzylamine.Gd.pDO3A at Q-band.

g	1.990
D	-1672 MHz
E	189 MHz
D-Strain	2323 MHz
E-Strain	244 MHz
H-Strain 1	0 MHz
H-Strain 2	0 MHz
H-Strain 3	1 MHz

The data proved much easier to fit for this spectrum. However, now the spectrum is not well fit for values greater than 1200 mT. The *g*-value varies again from that of the X-band data but follows the same pattern that it is the same variation as for the Gd.pDO3A species. The *D* and *E* values are of a similar order of magnitude to that of the X-band data and the *H*-strain values are also more similar.

4.5.3 Phenol.Gd.pDO3A

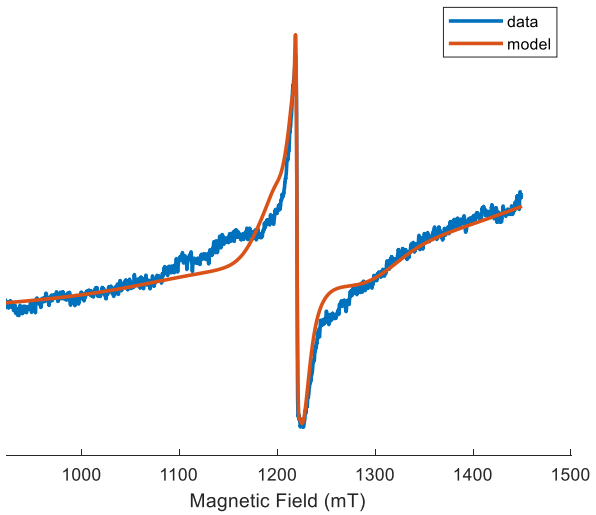

Figure 4.8: CW Q-band frozen solution EPR spectrum of phenol.Gd.pDO3A at 100 K, experimental (blue) and simulated (red), using the parameters in Table 4.7.

Table 4.7: Parameters obtained from non-linear least square regression model for phenol.Gd.pDO3A at Q-band.

g	1.991
D	-2099 MHz
E	116 MHz
D-Strain	2800 MHz
E-Strain	500 MHz
H-Strain 1	0 MHz
H-Strain 2	0 MHz
H-Strain 3	0 MHz

The fit again upon addition of phenol is very poor to the point where a false minimum may have been reached. There is once again a significant broadening of the spectrum. The *g*-value once again is significantly different to that of the X-band data. The *H*-strain values are also vastly different and the magnitude of the *D* value here is far greater.

4.5.4 DMSO.Gd.pDO3A

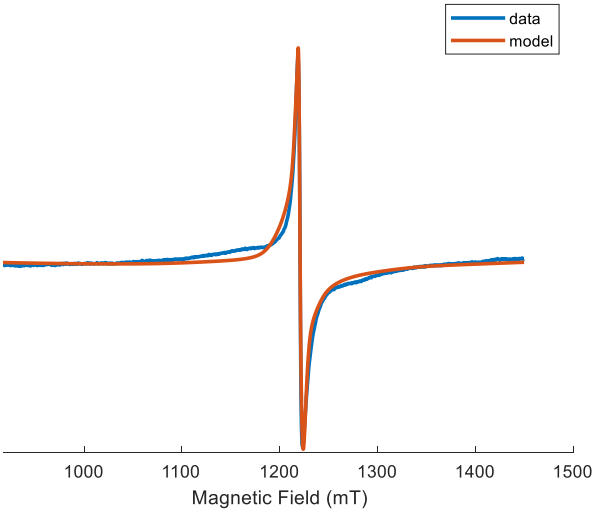

Figure 4.9. CW Q-band frozen solution EPR spectrum of DMSO.Gd.pDO3A at 100 K, experimental (blue) and simulated (red), using the parameters in Table 4.8.

Table 4.8. Parameters obtained from non-linear least square regression model for DMSO.Gd.pDO3A at Q-band.

g	1.990
D	-1305 MHz
E	217 MHz
D-Strain	2482 MHz
E-strain	198 MHz
H-Strain 1	0 MHz
H-Strain 2	1 MHz
H-Strain 3	1 MHz

DMSO.Gd.pDO3A proved by far the easiest to fit though the *g*-value is still significantly different to that at X-band. *D* is also significantly larger here and the *D*-strain value is huge indicating that there is a very large variation in *D* value. There has been no variation in *g*-value from the Gd.pDO3A species which is a different trend to that for the X-band data.

4.6 Summary of One Component Model

The fitting of the spectra as whole has proved difficult using a one component model and the parameters obtained for X-band and Q-band were, as a whole, very different. This should be improved using global fitting. Generally, the *D*-strain and *E*-strain values were on the same order of magnitude of *D* and *E* themselves which suggests a huge possible variation in these values and therefore the accuracy of these values can be questioned. A summary of the spectra is shown in **Figure 4.10**.

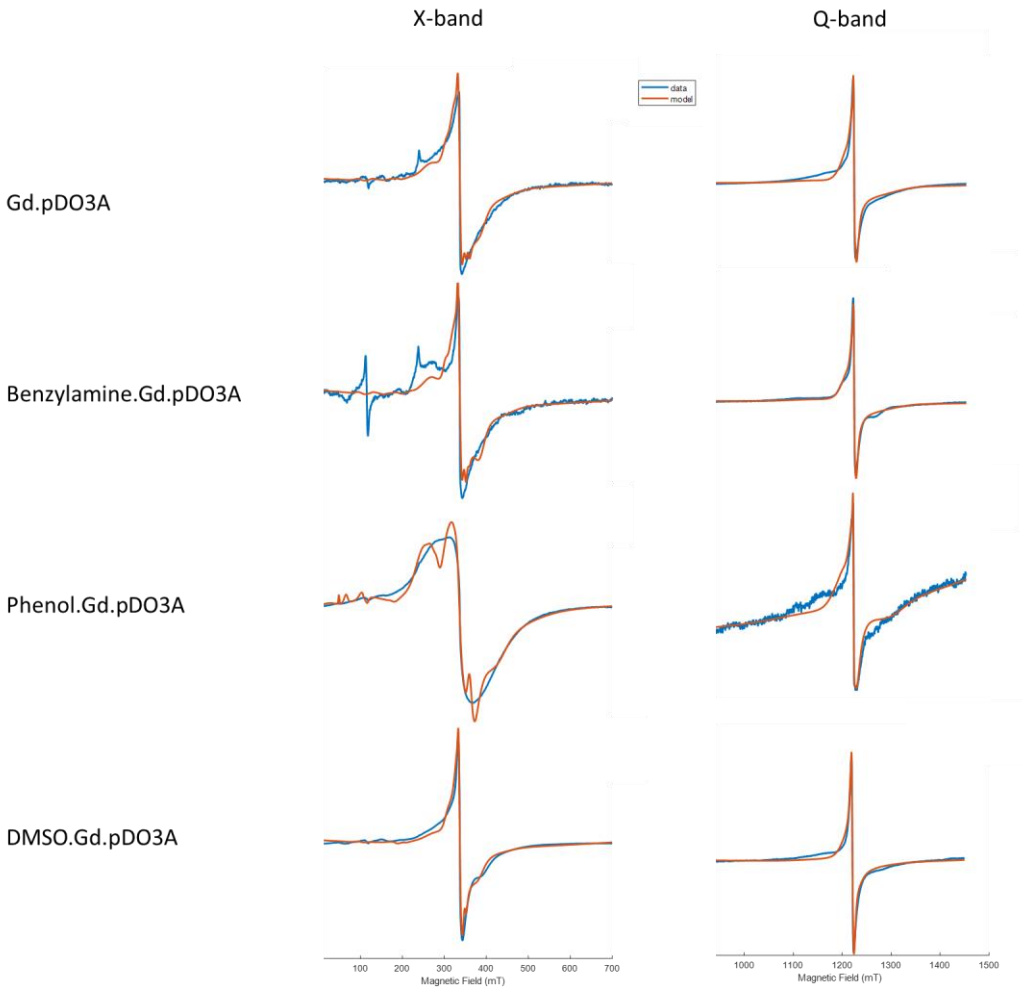

Figure 4.10: A summary of the spectra CW X-band and Q-band frozen solution EPR spectrum of the different species at 100 K, experimental (blue) and simulated (red), using a one component model.

4.7 Global Fitting for One Component Model

After the X-band and Q-band spectra were individually fitted a global fit was established of the two spectra. This is where the two spectra are normalised and concatenated together. They are then fit simultaneously by the EasySpin® package with initial estimates established using the individual fittings. The parameters *D* and *E* where extracted using this method to give us a better understanding of the ligand field splitting of the system. An approximate *E*/*D* ratio was also calculated to establish a relative measure of anisotropy of the system. These values are shown in **Table 4.9**.

Table 4.9: Important parameters obtained from global fitting of CW frozen solution EPR spectrum of the different species at 100 K.

Species	*g*	*D* (MHz)	*E* (MHz)	*E*/*D* ratio	Anisotropy of the system
Gd.pDO3A	1.999	-1184	190	~1/6	Rhombohedral distortion from prolate
Benzylamine.Gd.pDO3A	2.002	-1501	229	~1/7	Small rhombohedral distortion from prolate
Phenol.Gd.pDO3A	2.021	-1447	467	~1/3	Large rhombohedral distortion from prolate
DMSO.Gd.pDO3A	1.995	-864	123	~1/8	Small rhombohedral distortion from prolate

4.8 Discussion of Global Fitting for One Component Model

Despite the problems in the model, the variation in parameters and form of the spectra show that once again the anisotropy of the system can be controlled by binding different

ligands to Gd.pDO3A. There is a significant change in magnitude of *D* and *E* as well as *E*/*D* ratio depending on the species. The most dramatic changes comes from upon addition of DMSO where the *D* value is significantly smaller in magnitude than the other ligands and the *E*/*D* ratio is far smaller as a result. There is a relatively large variation in *g*-value which could prove useful for application to DNP-MRI (from 1.995 for DMSO.Gd.pDO3A to 2.021 for phenol.Gd.pDO3A).

4.9 Two Component X-band Fitting

4.9.1 Gd.pDO3A

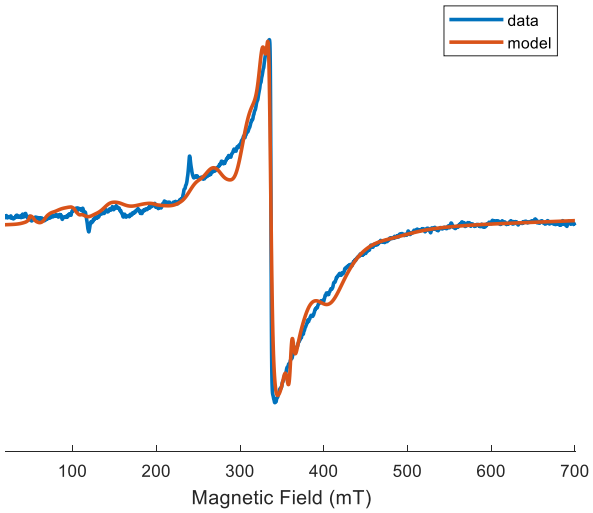

Figure 4.10: CW X-band frozen solution EPR spectrum of Gd.pDO3A at 100 K, experimental (blue) and simulated (red), using the parameters in Table 4.10 for a two component model.

Table 4.10: Parameters obtained from non-linear least square regression model at X-band.

Component 1	58 %
g	1.987
D	-3424 MHz
E	666 MHz
D-Strain	2422 MHz
E-Strain	464 MHz
H-Strain 1	50 MHz
H-Strain 2	61 MHz
H-Strain 3	50 MHz
Component 2	42 %
g	1.984
D	-1151 MHz
E	281 MHz
D-Strain	600 MHz
E-Strain	219 MHz
H-Strain 1	45 MHz
H-Strain 2	49 MHz
H-Strain 3	46 MHz

Whilst the fitting is still not optimal, it is much better than for the one component model. The model gives the parameters for two different components of which there is slightly more of component 1 than component 2. Component 1 has a much higher *D* and *E* value than component 2. Component 2 has a greater *E*/*D* ratio though both are quite large showing rhombohedral distortion. The *g*-values are fairly similar and the *H*-strain values are also very similar for both components.

4.9.2 Benzylamine.Gd.pDO3A

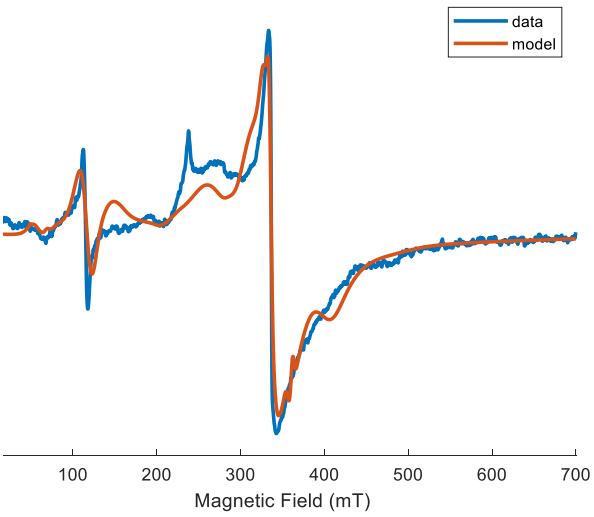

Figure 4.11: CW X-band frozen solution EPR spectrum of benzylamine.Gd.pDO3A at 100 K, experimental (blue) and simulated (red), using the parameters in Table 4.11 for a two component model.

Table 4.11: Parameters obtained from non-linear least square regression model for benzylamine.Gd.pDO3A at X-band.

Component 1	60 %
g	1.988
D	-3374 MHz
E	495 MHz
D-Strain	2521 MHz
E-Strain	454 MHz
H-Strain 1	58 MHz
H-Strain 2	61 MHz
H-Strain 3	51 MHz
Component 2	40 %
g	1.984
D	-1162 MHz
E	291 MHz
D-Strain	672 MHz
E-Strain	210 MHz
H-Strain 1	45 MHz
H-Strain 2	48 MHz
H-Strain 3	46 MHz

The fitting of this spectrum is much better for this model than the one component model. Some of the secondary features have been taken into account, for example at 100 mT. The two different components again have two significantly different *D* and *E* values. The values vary only a little between the Gd.pDO3A and benzylamine.Gd.pDO3A species. The *H*-strain values do not vary significantly between the species. There is slightly more of one component than the other.

4.9.3 Phenol.Gd.pDO3A

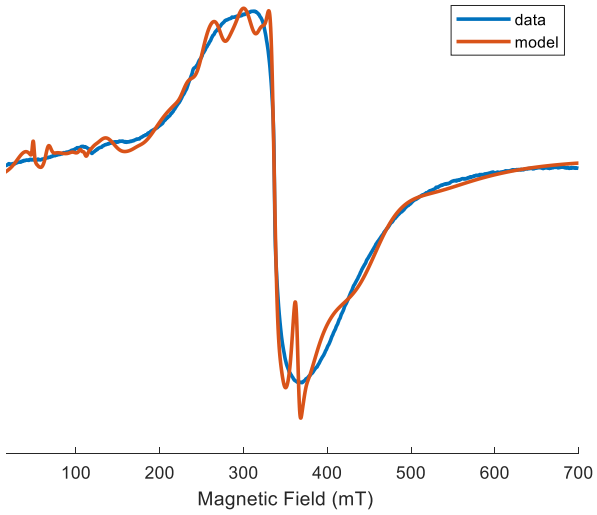

Figure 4.12: CW X-band frozen solution EPR spectrum of phenol.Gd.pDO3A at 100 K, experimental (blue) and simulated (red), using the parameters in Table 4.12 for a two component model.

Table 4.12: Parameters obtained from non-linear least square regression model for phenol.Gd.pDO3A at X-band.

Component 1	53 %
g	2.012
D	-2973 MHz
E	793 MHz
D-Strain	2661 MHz
E-Strain	300 MHz
H-Strain 1	52 MHz
H-Strain 2	40 MHz
H-Strain 3	37 MHz
Component 2	47 %
g	1.989
D	-1405 MHz
E	346 MHz
D-Strain	756 MHz
E-Strain	384 MHz
H-Strain 1	50 MHz
H-Strain 2	38 MHz
H-Strain 3	17 MHz

The fitting of this spectrum has been the poorest of the spectra for the two component model thus far. However, this fit is still far better than the previous model for phenol.Gd.pDO3A. There is a similar trend for the component 1 fitting to the other

component 1 complexes that they have a significantly larger *D*-value and smaller *E*/*D* ratio than that of component 2. For this complex there is a vast difference in the two *g*-values of the two different components. The *H*-values are relatively similar for both components. There is slightly more of one component than the other according to the fitting of this spectra.

4.9.4 DMSO.Gd.pDO3A

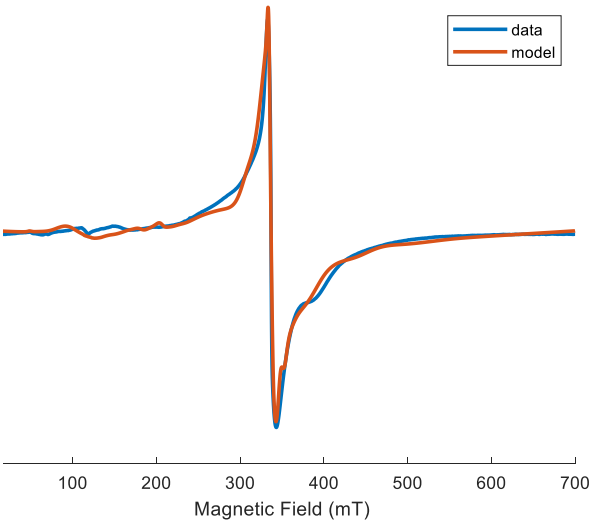

Figure 4.13: CW X-band frozen solution EPR spectrum of DMSO.Gd.pDO3A at 100 K, experimental (blue) and simulated (red), using the parameters in Table 4.13 for a two component model.

Table 4.13: Parameters obtained from non-linear least square regression model for benzyl DMSO.Gd.pDO3A at X-band.

Component 1	51 %
g	2.012
D	-2161 MHz
E	855 MHz
D-Strain	2512 MHz
E-Strain	181 MHz
H-Strain 1	57 MHz
H-Strain 2	51 MHz
H-Strain 3	61 MHz
Component 2	49 %
g	1.995
D	-924 MHz
E	159 MHz
D-Strain	1175 MHz
E-Strain	172 MHz
H-Strain 1	46 MHz
H-Strain 2	55 MHz
H-Strain 3	46 MHz

According to this model at X-band, DMSO.Gd.pDO3A has a significantly smaller *D*-value for both components when compared to the other complexes studied in this chapter. The two components still follow the same trend that for component 1 the *D* value is larger

than for component 2. The fitting on the whole is very pleasing and better than that of the one component model.

4.10 Two Component Q-Band Fitting

4.10.1 Gd.pDO3A

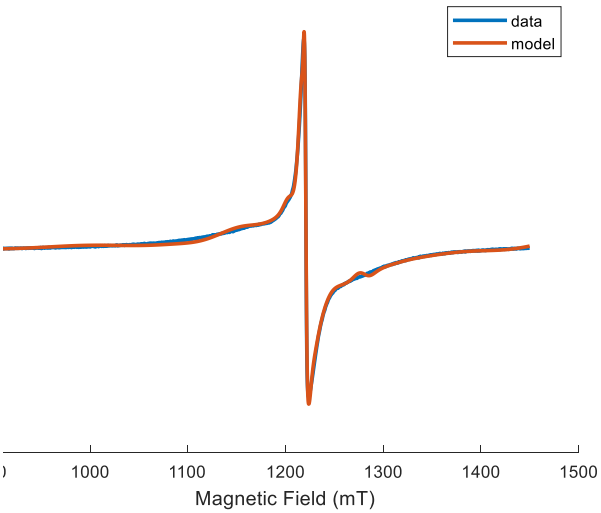

Figure 4.14: CW Q-band frozen solution EPR spectrum of Gd.pDO3A at 100 K, experimental (blue) and simulated (red), using the parameters in Table 4.14 for a two component model.

Table 4.14: Parameters obtained from non-linear least square regression model for Gd.pDO3A at Q-band.

Component 1	90 %
g	1.993
D	-3176 MHz
E	985 MHz
D-Strain	2045 MHz
E-Strain	468 MHz
H-Strain 1	52 MHz
H-Strain 2	59 MHz
H-Strain 3	40 MHz
Component 2	10 %
g	1.990
D	-1145 MHz
E	259 MHz
D-Strain	817 MHz
E-Strain	312 MHz
H-Strain 1	37 MHz
H-Strain 2	36 MHz
H-Strain 3	7 MHz

Whilst the fit is very good for this spectrum it yields very different results to the X-band spectrum. There is still one component which has a significantly larger *D* and *E* than the other which is promising. However, there is a notable difference in the *g*-values. There is not a great differentiation in the *H*-strain values. The results suggest that while the fit is good, the model still may not be entirely correct for the system.

4.10.2 Benzylamine.Gd.pDO3A

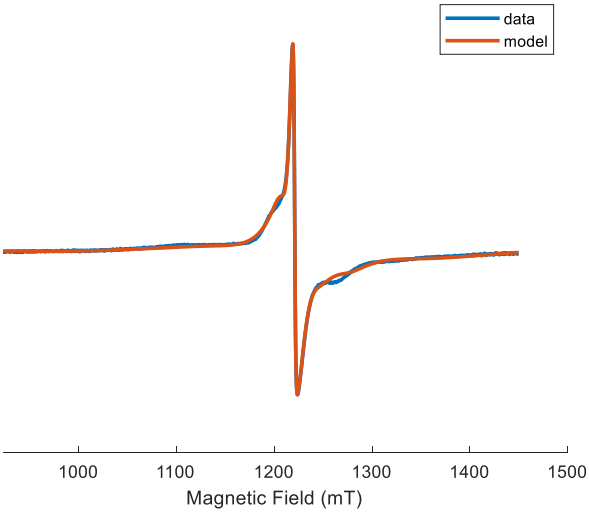

Figure 4.15: CW Q-band frozen solution EPR spectrum of benzylamine.Gd.pDO3A at 100 K, experimental (blue) and simulated (red), using the parameters in Table 4.15 for a two component model.

Table 4.15: Parameters obtained from non-linear least square regression model for benzylamine.Gd.pDO3A at Q-band.

Component 1	87 %
g	1.993
D	-1864 MHz
E	793 MHz
D-Strain	1909 MHz
E-Strain	664 MHz
H-Strain 1	44 MHz
H-Strain 2	100 MHz
H-Strain 3	87 MHz
Component 2	13 %
g	1.990
D	-793 MHz
E	216 MHz
D-Strain	619 MHz
E-Strain	289 MHz
H-Strain 1	5 MHz
H-Strain 2	90 MHz
H-Strain 3	29 MHz

The fitting for the two component model is much better than for the one component model for benzylamine.Gd.pDO3A. However, we observe a very similar results for this and the Gd.pDO3A. Again, the results are quite different to the X-band. However, consistently, there is one species with a much larger *D* value than the other species.

4.10.3 Phenol.Gd.pDO3A

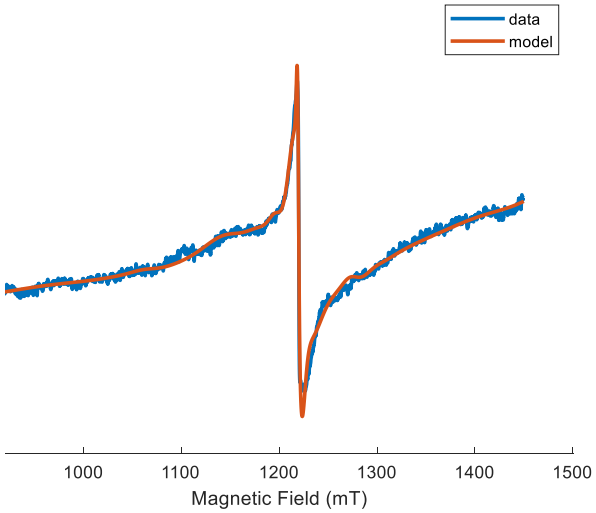

Figure 4.16: CW Q-band frozen solution EPR spectrum of phenol.Gd.pDO3A at 100 K, experimental (blue) and simulated (red), using the parameters in Table 4.16 for a two component model.

Table 4.16: Parameters obtained from non-linear least square regression model for phenol.Gd.pDO3A at Q-band.

Component 1	90 %
g	2.004
D	-3823 MHz
E	1092 MHz
D-Strain	2694 MHz
E-Strain	369 MHz
H-Strain 1	64 MHz
H-Strain 2	24 MHz
H-Strain 3	42 MHz
Component 2	10 %
g	1.990
D	-1469 MHz
E	248 MHz
D-Strain	1289 MHz
E-Strain	314 MHz
H-Strain 1	84 MHz
H-Strain 2	61 MHz
H-Strain 3	10 MHz

Although the *g*-values are not the same as for the X-band values obtained, they follow the same trend. The g-value for component 1 is larger than for component 2. The main difference between this fit and the previous, is the difference in the amount of each component. For Q-band, there is considerably more of one component than the other. The *D*, *E* and *E*/*D* ratio for each component follows the same trend as for the X-band data although the values given show some variation.

4.10.4DMSO.Gd.pDO3A

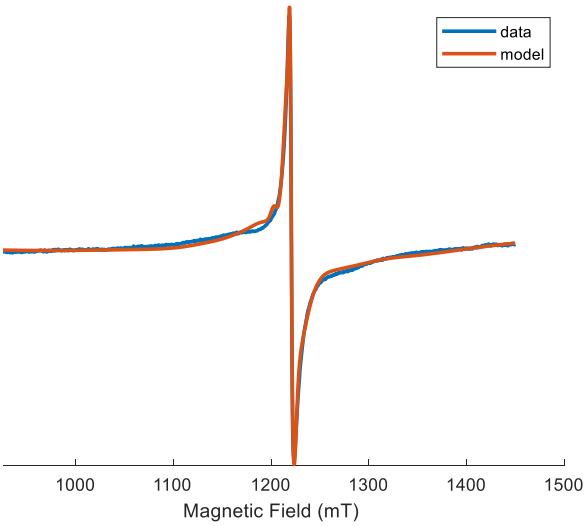

Figure 4.17: CW Q-band frozen solution EPR spectrum of DMSO.Gd.pDO3A at 100 K, experimental (blue) and simulated (red), using the parameters in Table 4.17 for a two component model.

Table 4.17: Parameters obtained from non-linear least square regression model for DMSO.Gd.pDO3A at Q-band.

Component 1	73 %
g	2.011
D	-2818 MHz
E	549 MHz
D-Strain	3052 MHz
E-Strain	411 MHz
H-Strain 1	48 MHz
H-Strain 2	43 MHz
H-Strain 3	4 MHz
Component 2	27 %
g	1.990
D	-1221 MHz
E	275 MHz
D-Strain	1172 MHz
E-Strain	275 MHz
H-Strain 1	35 MHz
H-Strain 2	54 MHz
H-Strain 3	38 MHz

For DMSO.Gd.pDO3A the values given at Q-band are similar to those given at X-band, matching far better than the other complexes. There is once again a difference between the percentage of each component between the X-band and Q-band but this is less exaggerated than for the other complexes. The fit for the two component model for this species is very pleasing.

4.11 Summary of Spectra for Two Components

For all the given spectra there is quite a large difference in the percentage of each component going from X-band to Q-band, however, this is less exaggerated for DMSO.Gd.pDO3A. The consistent nature of this suggests there is a systematic error in the model. However, the two component model routinely fits the data well in comparison to the one component model.

There is also the consistent general trend that for component 1 there is a far greater *D* value. This suggests that Component 1 is the SAP isomer, which would be consistent with there being a higher percentage. This is understandable, as the TSAP isomer has much poorer alignment between the ligand orbitals and the *f*-orbitals on the lanthanide. It would therefore be expected that B_2^0 would be smaller for TSAP which correlates to the *D* value.

Once again, the form of the spectra dramatically changes according to the ligand that is bound. However, fitting this set of spectra compared to fitting the changes for Gd.DOTAMPh has been consistently more difficult. The largest variations come from phenol.Gd.pDO3A where the spectra dramatically broadens and DMSO.Gd.pDO3A where the main spectral feature becomes much sharper. Whilst difficult to quantify, again it can be observed that ligation can dramatically change the form of the spectra and hence the properties of the system. Global fitting will aid this quantification making it easier to interpret.

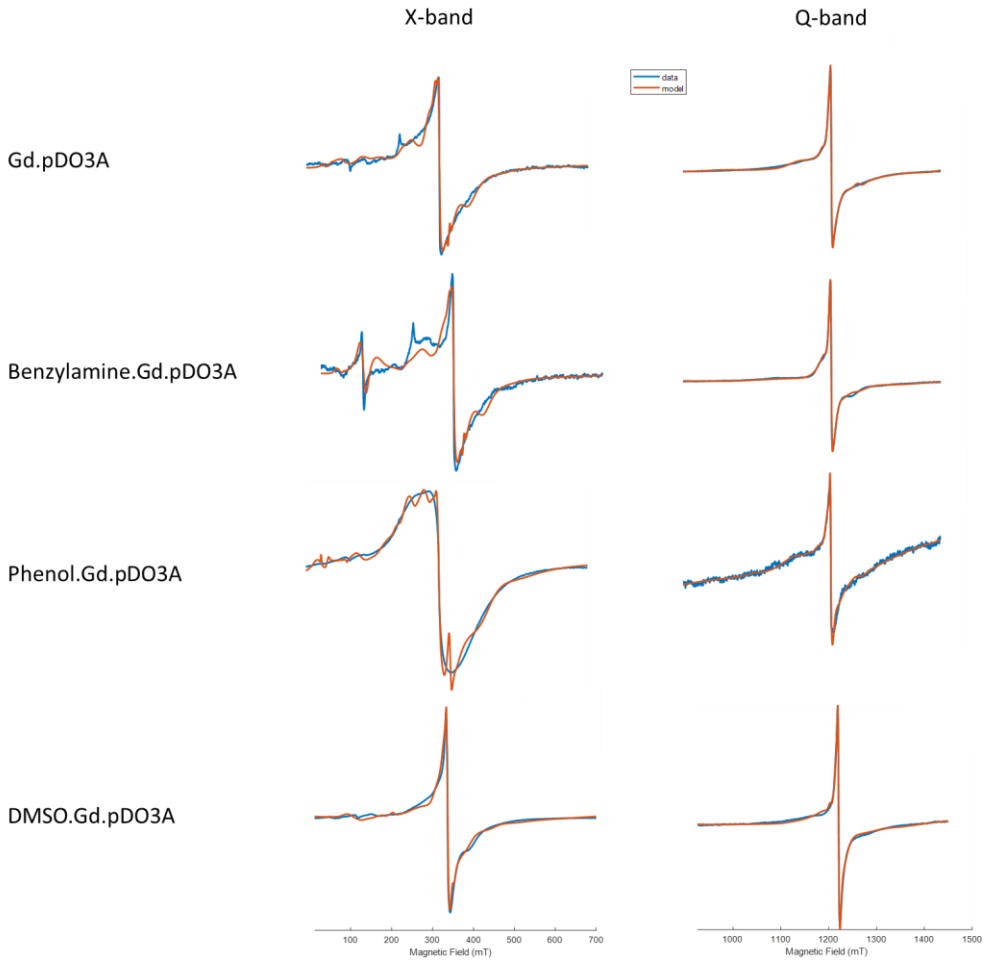

Figure 4.18: A summary of the spectra CW X-band and Q-band frozen solution EPR spectrum of the different species at 100 K, experimental (blue) and simulated (red), using a two component model

4.12 Global Fitting for Two Component Model

After the X-band and Q-band spectra were individually fitted a global fit was established of the two spectra. Again, the two spectra were normalized and concatenated together. They were then fitted simultaneously by the EasySpin® package with initial estimates established using the individual fittings. The parameters *g*, *D* and *E* where extracted using this method. An approximate *E*/*D* ratio was also calculated to establish a relative measure of anisotropy of the system.

Table 4.18. Fitting parameters for simulation of frozen solution (100 K) X- and Q-band EPR spectra of the different Gd.pDO3A and ligand complexes, using a global fitting method and two component model (see text for details).

Species		*g*	*D*(MHz)	*E*(MHz)	*E*/*D* ratio	Anisotropy of the system
Gd.pDO3A Component 1	53 %	1.983	-4082	409	~1/10	Small rhombohedral distortion from prolate
Gd.pDO3A Component 2	47 %	1.991	-1000	185	~1/5	Rhombohedral distortion from prolate
Benzylamine.Gd.pDO3A Component 1	60 %	1.976	-4140	388	~1/10	Small rhombohedral distortion from prolate
Benzylamine.Gd.pDO3A Component 2	40 %	2.009	-1102	174	~1/7	Rhombohedral distortion from prolate
Phenol.Gd.pDO3A Component 1	56 %	2.003	-3291	367	~1/10	Small rhombohedral distortion from prolate
Phenol.Gd.pDO3A Component 2	44 %	2.040	-1138	253	~1/5	Rhombohedral distortion from prolate
DMSO.Gd.pDO3A Component 1	68 %	2.017	-2871	511	~1/5	Rhombohedral distortion from prolate
DMSO.Gd.pDO3A Component 2	32 %	1.991	-440	164	~1/3	Rhombohedral distortion from prolate

4.13 Discussion of Global Fitting for Two Component Model

For component 1 in each case *D* is much larger than for all the species in this chapter compared to the Gd.DOTAMPh species in **Chapter 3**. This can be explained if component 1 is SAP whereas Gd.DOTAMPh is a distorted SAP isomer. Therefore, if taking a crystal field approach, Gd.DOTAMPh has worse overlap of *f*-orbitals than the SAP isomer of Gd.pDO3A. Each component 2 species has *D* values smaller or comparable to that of the Gd.DOTAMPh species in **Chapter 3** which is consistent with the TSAP isomer. Overall, using this model we can observe that whether we have the SAP or TSAP isomer has a considerable effect on ligand field splitting parameters and therefore the properties of the molecule.

Varying the ligand has a significant effect on both components with the *D*, *E* and *E*/*D* ratios changing significantly depending on the ligand. This in turn will affect the *g*-value. However, the trend is far more complex than the trends discussed for the Gd.DOTAMPh species in **Chapter 3**. For example, DMSO no longer appears to reduce *E*/*D* ratio but rather enlarges it in this scenario. The complexity of the parameter values obtained could be due to the fact there are two possible binding sites (axial and equatorial). This would also explain the large *D*-strain and *E*-strain values as they are the same order of magnitude as *D* and *E* in nearly every case.

4.14 Conclusions to Chapter

Both models are not ideal for describing the systems studied in this chapter. However, the two component model gave far better results and fits than the one component model.

What is obvious from the spectra is that once again, the form of the spectra can be varied dramatically depending on the ligand bound. It has also been demonstrated through the two component model that SAP and TSAP have very different parameters such as *D* and *E* impacting the ligand field parameters of our system. The *g*-value can also be manipulated which could prove useful for DNP applications.

4.15 References

[1] V. K. Michaelis, R. G. Griffin, B. Corzilius and S. Vega, High Field Dynamic Nuclear Polarisation, Chichester, West Sussex: WILEY, 2020.

[2] S. Stoll and A. Schweiger, J. Magn. Reson., vol. 178, pp. 42-55, 2006.

[3] S. Stoll and A. Schweiger, Chem. Phys. Lett., vol. 380, no. 3-4, pp. 464-470, 2003.

5 Using EPR to Explore Polymetallic Complexes and DNP NMR Study

5.1 Introduction

CW EPR spectra of GdGd.p2DO3A complexes were used to explore once again how *g*-value and ligand field splitting parameters varied upon ligation. If this could be demonstrated there is the potential application of these complexes to be used in DNP MRI. This is because if each individual center has a different *g*-value with a small difference between the two on the order of the Larmor frequency of ^{13}C (or another NMR active nucleus that could be used in hyperpolarization) then the cross effect would be initiated as well as hyperpolarization through other mechanisms such as the solid effect. [1,2] Corzelius *et al.* has already demonstrated that linear bis-Gd(III) complexes have potential for DNP NMR, although ligation was not explored. [3]

The study in this thesis uses polymetallic complexes based on $GdDOTA^-$ to see if they are suitable for DNP application. As discussed in **Chapter 1**, $GdDOTA^-$ has high stability kinetically and thermodynamically rendering it non-toxic and it is useful as a commercial contrast agent. It is therefore hoped that if these complexes have good potential as hyperpolarization agents, that there would be easier translation for clinical practice.

Due to there being two Gd(III) centers with various enantiomers, diastereomers and much rotation in each part of the complex it will be very difficult to take all these factors into account with a single model. There are many isomers that could be formed through the

multiple rotations and conversions; too many to be modelled simply by a multicomponent system effectively. Therefore whilst **Chapter 4** may give us some perspective on what is happening the system is far more complex in this chapter.

The complex was 3.6 mM dissolved in 6.0 M urea in a 60:40 water:glycerol mixture by weight. This solvent system was selected due to solubility compatibility with the complex and urea. Urea was added as ^{13}C-urea in order to be used as the hyperpolarisation agent for our DNP NMR studies. The complex is highly soluble in the new solvent system and also this solvent system has the advantage that it is already used in DNP MRI imaging as it forms a glass at low temperatures and is also non-toxic *in vivo*. This solvent system has already been used in *in vivo* DNP studies. This could improve the application potential of the project. [4, 5]

Measurements of the initial complexes were taken using CW EPR using X-band (9 GHz) frequencies at 100 K and the ligands added were 100 equivalents (360 mM). These were then followed by Q-band CW EPR measurements that also took place at 100 K. The structure of the three bidentate bridging ligands are shown in **Figure 5.1**.

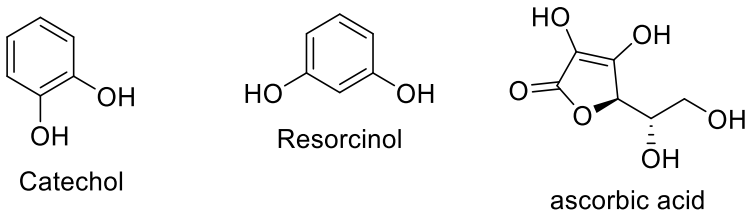

Figure 5.1: Structures of bidentate bridging proligands used in this study. Note: The exact sites of binding for ascorbic acid to the GdGd.p2DO3A species are unknown but what is important is the asymmetry.

5.2 Experimental Conditions for CW EPR

As in Chapter 3 and Chapter 4 measurements were initially taken using CW EPR using X-band (9.5 GHz) frequencies followed by Q-band (34 GHz) at 100 K. Measurements took place on a Bruker Biospin EMX spectrometer equipped with a high sensitivity Bruker probe head and an Oxford Instruments helium-flow cryostat. Modulation amplitudes and frequencies of 0.01 mT and 100 kHz were used, respectively. The microwave power was adjusted in order to avoid spectral distortions.

5.3 Computational Analysis of Results

The spectra were processed using MATLAB® and EasySpin® software. [6] For the frozen solution CW EPR data the *pepper* function was used. After the spectra were processed, using the software, parameters were extracted by fitting the data using a non-linear least squares regression model where an overall RMSD value for the entire system is minimized to as close to zero as possible. Using the parameters extracted from the simulations, model spectra can be produced.

To obtain the best fit possible using the software, initial reasonable values are first approximated and simulated to see if they give a model with a similar profile and features to the data. After this has been established as a reasonable fit the simulation is undertaken for a set period before the results are examined. If the values are converging to a certain value and the model looks progressively like the data, then the simulation can be allowed to run until the software accesses that the best possible values have been reached. If it is obvious that this is not the case or that for certain parameters, the values are converging

far too slowly then the model with the initial values set for parameters will have to be adapted and reassessed.

A one component model was used to fit these spectra. This is because the system is complex and it was decided the best approach was to use a one component model where the variation in *D* and *E* values should be taken into account by the *D*-strain and *E*-strain values. Whilst this is not ideal it would be computationally too expensive to use up to a multicomponent component model which would potentially be a better representation for this system. It is also difficult to know the exact number of components the multicomponent system would have without further understanding of the system itself.

5.4 X-Band Spectra

5.4.1 GdGd.p2DO3A

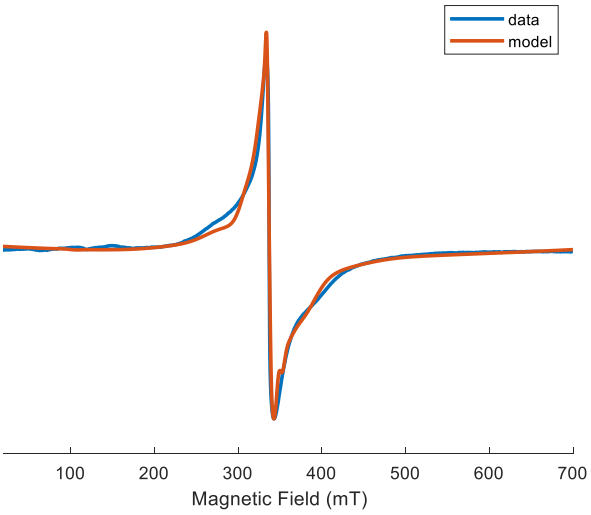

Figure 5.2: CW X-band frozen solution EPR spectrum of GdGd.p2DO3A at 100 K, experimental (blue) and simulated (red), using the parameters in Table 5.1.

Table 5.1: Parameters obtained from non-linear least square regression model at X-band.

g	1.994
D	-929 MHz
E	155 MHz
D-Strain	1200 MHz
E-Strain	182 MHz
H-Strain 1	51 MHz
H-Strain 2	3 MHz
H-Strain 3	40 MHz

The spectrum is fitted well with the main spectral feature taken into account. However, there are finer details which are not fitted as well, such as the feature at about 300 mT. There are also additional features added to the latter part of the turning point of the spectra at about 350 mT. The *D* value is not as large for this bis-complex as for the mono analogue given in **Chapter 4** even when taking into account the different SAP and TSAP isomers for Gd.pDO3A. Both the *D*-strain values and *E*-strain values are large which is to be expected as we know the system is complex due to there being a vast number of possible isomers and therefore a large number of potential *D* and *E* values. The *E*/*D* ratio is relatively large for the X-band data with a value of about 1/6 indicating there is some rhombohedral distortion.

5.4.2 Resorcinol GdGd.p2DO3A

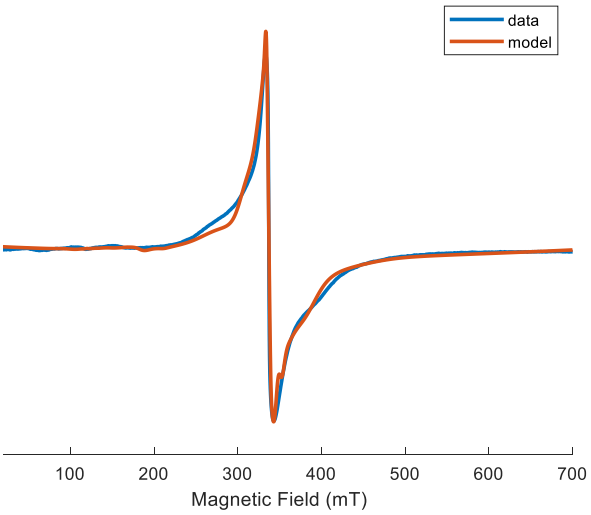

Figure 5.3: CW X-band frozen solution EPR spectrum of resorcinol.GdGd.p2DO3A at 100 K, experimental (blue) and simulated (red), using the parameters in Table 5.2.

Table 5.2: Parameters obtained from non-linear least square regression model for resorcinol.GdGd.p2DO3A at X-band.

g	1.995
D	-940 MHz
E	154 MHz
D-Strain	1254 MHz
E-Strain	180 MHz
H-Strain 1	1 MHz
H-Strain 2	0 MHz
H-Strain 3	49 MHz

This spectrum is incredibly similar to that of GdGd.p2DO3A which suggests weak ligand binding. The additional features added to the latter part of the turning point of the spectra at about 350 mT are more exaggerated in the fitting of this spectrum. The *D* and *E* values are almost identical and differences in the values could merely be due to artefacts. There are however, significant differences in the *H*-strain values and there is a slight change in the *g*-value which gives some evidence for binding and that there is some minimal change within the molecule. However, we must take into account that this slight change in *g*-value could be within error.

5.4.3 Catechol.Gd.Gd.p2DO3A

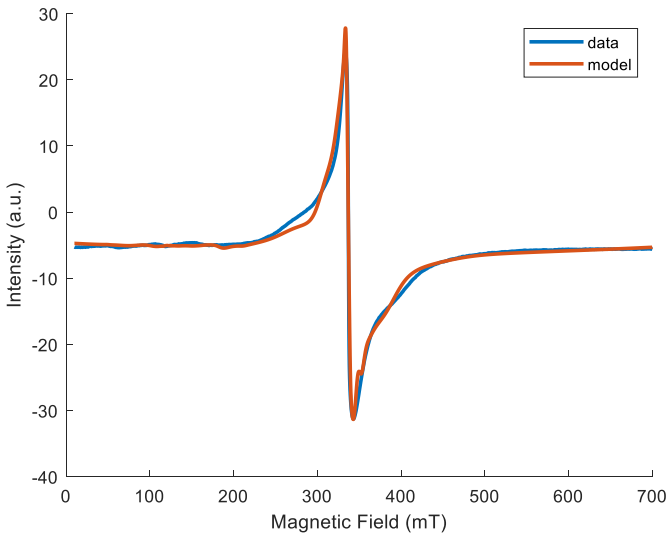

Figure 5.4: CW X-band frozen solution EPR spectrum of catechol.GdGd.p2DO3A at 100 K, experimental (blue) and simulated (red), using the parameters in Table 5.3.

Table 5.3: Parameters obtained from non-linear least square regression model for catechol.GdHd.p2DO3A at X-band.

g	1.994
D	-936 MHz
E	154 MHz
D-Strain	1250 MHz
E-Strain	180 MHz
H-Strain 1	0 MHz
H-Strain 2	0 MHz
H-Strain 3	46 MHz

The same response can be made for this spectra as for resorcinol.GdGd.p2DO3A. The changes in *D* and *E* values are minimal. There is once again some change in *H*-strain values which could mean there is slight change in structure. The results as a whole are almost identical to those of GdGd.p2DO3A. There is a very small change in *g*-value. However, we must take into account that this slight change in *g*-value could be within error.

5.4.4 Ascorbic acid.GdGd.p2DO3A

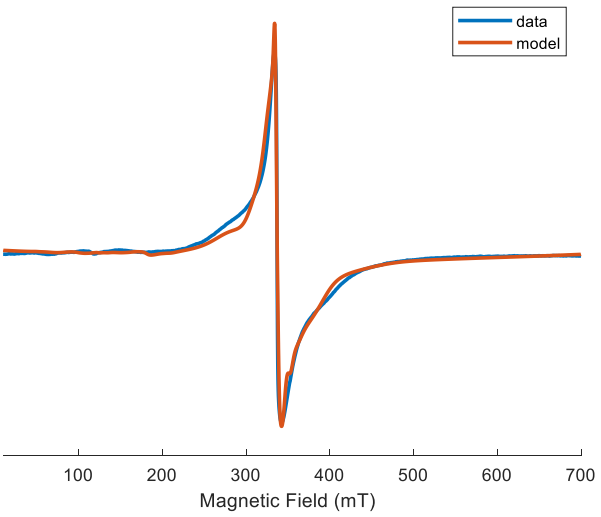

Figure 5.5: CW X-band frozen solution EPR spectrum of ascorbic acid.GdGd.p2DO3A at 100 K, experimental (blue) and simulated (red), using the parameters in Table 5.4.

Table 5.4: Parameters obtained from non-linear least square regression model for ascorbic acid.GdGd.p2DO3A at X-band.

g	1.993
D	-901 MHz
E	158 MHz
D-Strain	1081 MHz
E-Strain	191 MHz
H-Strain 1	80 MHz
H-Strain 2	0 MHz
H-Strain 3	1 MHz

Very little difference can once again be seen between this species and the EPR spectra for GdGd.p2DO3A. The main difference is that there is some variation in the *H*-strain.

The similarities throughout the series of complexes show that the binding must be weak especially when compared to how the spectra can change upon ligation for the mono-analogue (**Chapter 4**). We would expect stronger binding for the mono-analogue as there is less steric hinderance and the ligands were smaller. It is difficult to make a direct comparison as the ligands here are different to those in **Chapter 4**.

5.5 Q-band Spectra

5.5.1 GdGd.p2DO3A

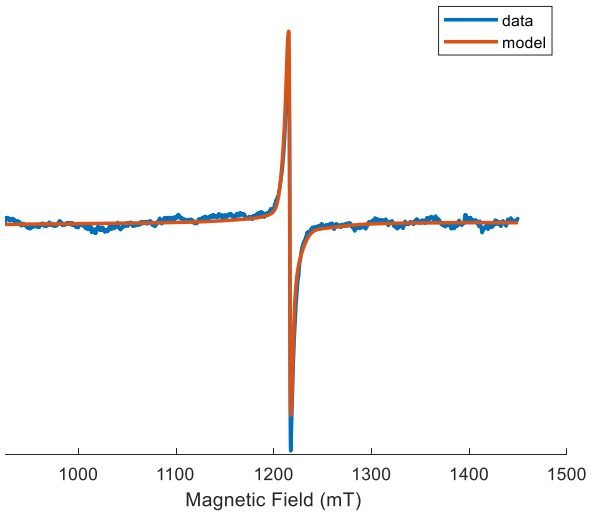

Figure 5.6: CW Q-band frozen solution EPR spectrum of GdGd.p2DO3A at 100 K, experimental (blue) and simulated (red), using the parameters in Table 5.5.

Table 5.5: Parameters obtained from non-linear least square regression model for GdGd.p2DO3A at Q-band.

g	1.991
D	-833 MHz
E	55 MHz
D-Strain	1600 MHz
E-Strain	332 MHz
H-Strain 1	79 MHz
H-Strain 2	1 MHz
H-Strain 3	24 MHz

The fitting for this spectrum is pleasing. The *D*-strain value is sizeable which is again to be expected. The *E*/*D* ratio is smaller than that given for the X-band. The *g*-value is also

smaller than the one given at X-band though again this is not a significant difference and could just be within error. *D*-strain and *E*-strain values are significantly large (*D*-strain is nearly twice that of the *D* value itself) and suggests a large amount of error in the given *D*-value.

5.5.2 Resorcinol.GdGd.p2DO3A

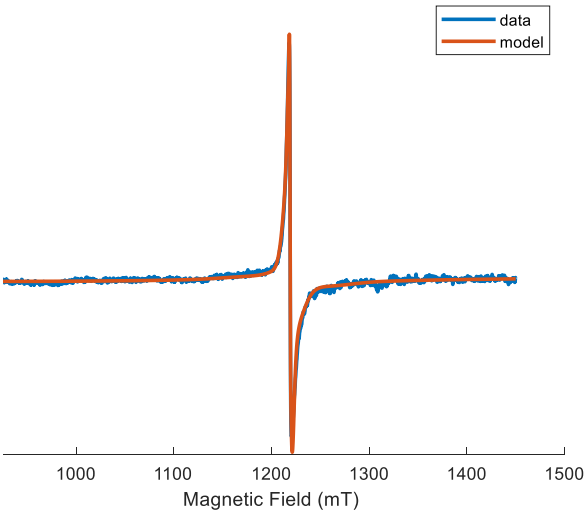

Figure 5.7: CW Q-band frozen solution EPR spectrum of resorcinol.GdGd.p2DO3A at 100 K, experimental (blue) and simulated (red), using the parameters in Table 5.6.

Table 5.6: Parameters obtained from non-linear least square regression model for resorcinol.Gd.Gd.p2DO3A at Q-band.

g	1.990
D	-1000 MHz
E	170 MHz
D-Strain	1455 MHz
E-Strain	177 MHz
H-Strain 1	80 MHz
H-Strain 2	0 MHz
H-Strain 3	1 MHz

Here resorcinol.GdGd.p2DO3A has a *D* and *E* value which is significantly different to that at for GdGd.p2DO3A. This is a different trend to that observed for X-band. The *g*-value varies only slightly between the two species. These values are very similar to that of the X-band values.

5.5.3 Catechol.GdGd.DO3A

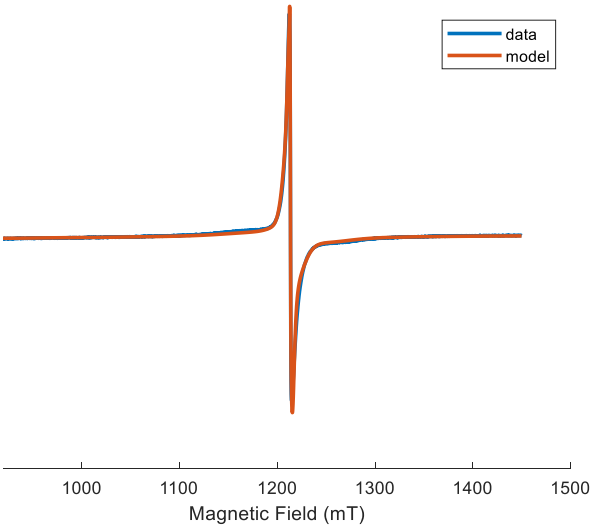

Figure 5.8: CW Q-band frozen solution EPR spectrum of catechol.GdGd.p2DO3A at 100 K, experimental (blue) and simulated (red), using the parameters in Table 5.7.

Table 5.7: Parameters obtained from non-linear least square regression model for catechol.GdGd.pDO3A at Q-band.

g	1.990
D	-973 MHz
E	147 MHz
D-Strain	1532 MHz
E-strain	205 MHz
H-Strain 1	80 MHz
H-Strain 2	3 MHz
H-Strain 3	1 MHz

These values, with the exception of the *H*-strain are almost identical to that found for resorcinol.GdGd.p2DO3A and the *g*-values given are identical. The spectral features are also almost identical. The *D* and *E* values are very similar to those given at X-band.

5.5.4 Ascorbic acid.GdGd.p2DO3A

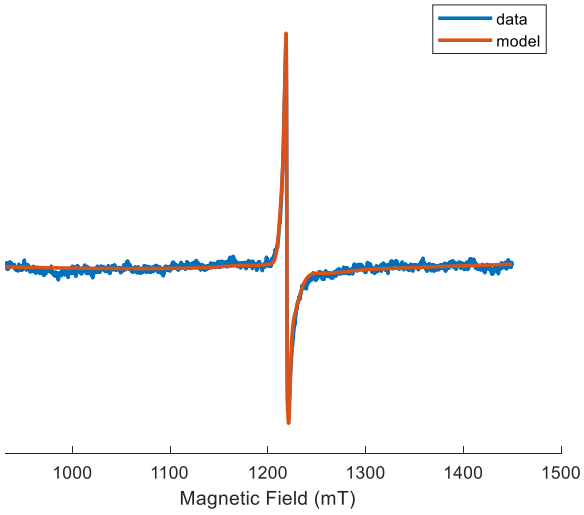

Figure 5.9: CW Q-band frozen solution EPR spectrum of ascorbic acid.GdGd.p2DO3A at 100 K, experimental (blue) and simulated (red), using the parameters in Table 5.8.

Table 5.8: Parameters obtained from non-linear least square regression model for ascorbic acid.GdGd.p2DO3A at Q-band.

g	1.990
D	- 993 MHz
E	-161 MHz
D-Strain	1102 MHz
E- Strain	113 MHz
H-Strain 1	80 MHz
H-Strain 2	0 MHz
H-Strain 3	19 MHz

The same trends can be observed for this spectrum as the previous two spectra. There is a little less uncertainty in the *D*-strain value for this species than for catechol.GdGd.p2DO3A. However, for the *g*, *D* and *E* values there is no significant change. There is also very little change in the *H*-strain values.

5.6 Summary of Spectra

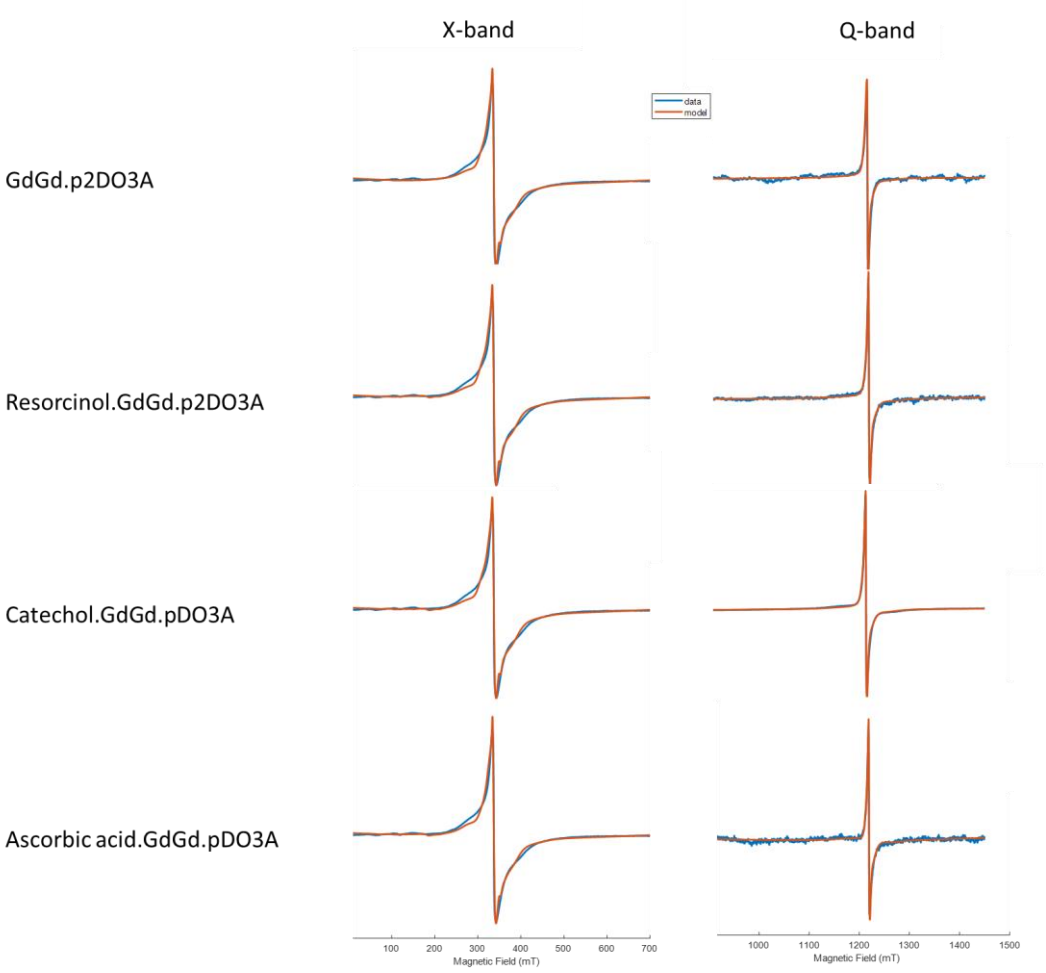

Figure 5.10: A summary of the spectra CW X-band and Q-band frozen solution EPR spectrum of the different species at 100 K, experimental (blue) and simulated (red).

As can be seen from the summary of spectra in Figure 5.10 there is very little variation from species to species. This suggests the binding of the bidentate ligand is very weak and/or has very little effect on the ligand field splitting. The fitting itself was adequate but the model is a huge simplification of the system studied as there could be multiple isomers present. As shown in **Chapter 4** with a simpler SAP/TSAP system, each of these

could have a vastly different *g*, *D* and *E* value and therefore a different *E*/*D* ratio. One indication that the model is not sufficient here is the fact that for each species the X-band and Q-band parameters obtained are on the whole different from one another. Other ligands were tested such as benzene-1,3-diamine, benzene-1,2,-diamine, 3-amniophenol and 2-aminophenol but could not be used due to either solubility or glassing at low temperature issues.

5.7 Global Fitting

After the X-band and Q-band spectra were individually fitted, a global fit was established of the two spectra. This is where the two spectra are normalised and concatenated together and then fitted simultaneously by the EasySpin® package with initial estimates established using the individual fittings. The parameters *g*, *D* and *E* where extracted using this method to give us a better understanding of the system. An approximate *E*/*D* ratio was also calculated to establish a relative measure of the anisotropy of the system. These values are shown in **Table 5.9**.

Table 5.9: Fitting parameters for simulation of frozen solution (100 K) X-band and Q-band EPR spectra of GdGd.p2DO3A complexes and ligands, using a global fitting method (see text for details).

Species	*g*	*D*(MHz)	*E*(MHz)	*E*/*D* ratio	Anisotropy of the system
GdGd.p2DO3A	1.994	-1074	355	~1/3	Maximum rhombohedral distortion from prolate
Resorcinol.GdGd.p2DO3A	1.995	-1087	360	~1/3	Maximum rhombohedral distortion from prolate
Catechol.GdGd.p2DO3A	1.995	-1057	322	~1/3	Maximum rhombohedral distortion from prolate
Benzoic acid.Gd.DOTAMPh	1.996	-996	363	~1/3	Maximum rhombohedral distortion from prolate

5.8 Discussion of Global Fitting Results

It can be seen from the global fitting that in each case there is a small variation in g value and a small variation in the *D* and *E* values. In every case *E*/*D* is about a third. There is very little change to system upon addition of each ligand.

5.9 CW EPR Conclusions

In previous chapters it was shown that upon addition of an excess of ligand there was a dramatic change to the form of the spectrum as well as *g*, *D* and *E* values. In this chapter we see that there is very little change in this system upon addition of an excess of ligand. The most likely explanation for this is that there is very little binding occurring. A reason

for this could be that the urea present as the species to be polarized may be binding too competitively with the Gd(III) stopping the bidentate ligand from binding into the two sites. This is a possibility, as there is over ten times the amount of ^{13}C-urea than our bridging ligand. Whatever the reason, this is a little disappointing as it was it hoped that ligand binding of an asymmetric ligand such as ascorbic acid would aid in the process of DNP MRI. However, it was decided to take these complexes and see if hyperpolarization could occur i.e. that there was some potential in the species for application to DNP anyway.

5.10 ^{13}C Hyperpolarisation Studies

Our system to be studied for DNP consisted of 6.0 M ^{13}C-urea doped with 3.6 mM GdGd.p2DO3A along with 360 mM of each appropriate bridging ligand. The solvent was 40:60 water:glycerol by weight. ^{13}C-pyruvate was tested with the complexes as this would have been the ideal agent (**Chapter 1**) but unfortunately a crystalline solid formed upon freezing rendering it useless for application to DNP. Other bridging ligands were also tested (previously listed) but could not be used due to either solubility or glassing issues at low temperature.

As described in **Chapter 1** various processes can lead to DNP; the primary mechanism here is assumed to be the cross-effect as the system contains two centres with unpaired electrons. In order to pump a high enough proportion of nuclear spins in our ^{13}C-urea into a given state, we required a super-conducting cryostat with a high microwave power

source **Figure 5.11**. Experiments were conducted on the a commercially available Hypersense by Oxford Instruments.

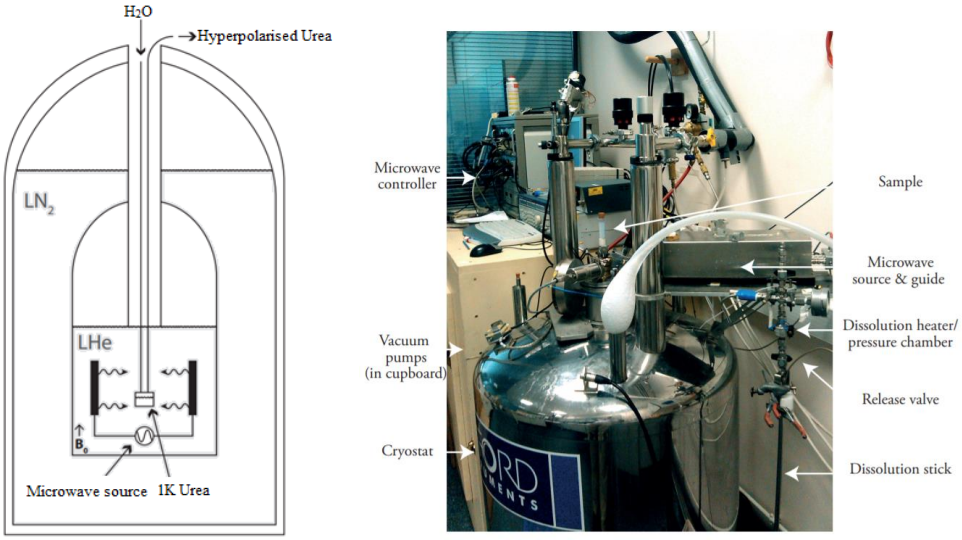

Figure 5.11: Left: Schematic of the inside of a hyperpolariser. Right: Photograph of a hyperpolariser. Figure adapted with permission from Jack Miller DPhil thesis.

Before hyperpolarising our sample we ran a microwave sweep. This consisted of the NMR signal build-up after every 5 minutes due to DNP against microwave frequency to find the optimum frequency for building up our NMR signal. The relationship proved to be complex and not like that of ^{13}C-pyruvate with OX063 **Figure 5.12** and Gd.DOTA^{-}.



Figure 5.12: Examples of organic radicals for use in DNP MRI.

The microwave sweep and subsequent build-up of ^{13}C-pyrvate signal can be seen in **Figure 5.13**. There is some evidence in the literature that this is due to the multiple spin-manifolds within our complex though it is the $\mathbf{M}_s$ = -1/2 ↔ +1/2 transition that is responsible for DNP NMR signal. [7]

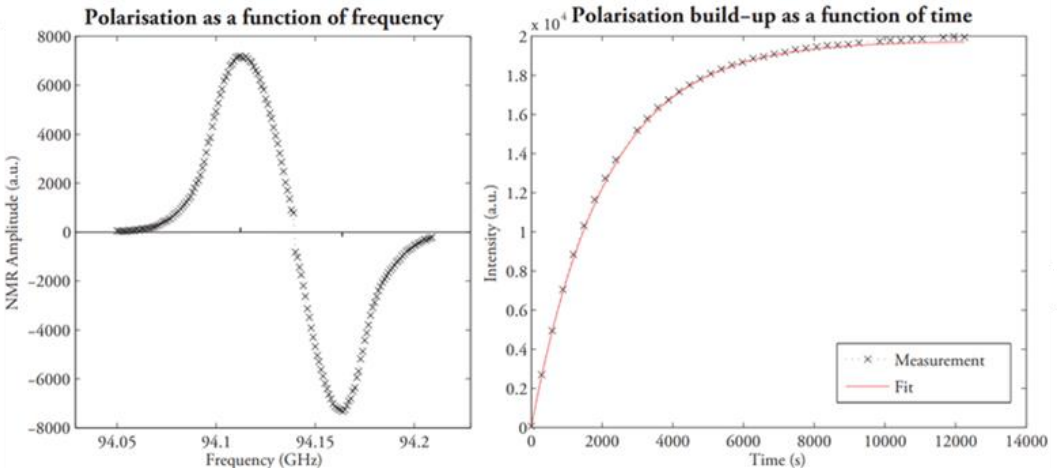

Figure 5.13: Left: Microwave sweep for ^{13}C-pyruvate. Right: Build-up of hyperpolarization for ^{13}C-pyruvate. Figure adapted with permission from Jack Miller DPhil thesis.

Our solutions were hyperpolarised in a prototype DNP hyperpolariser at 94.020 GHz for 14 hours with a microwave power of 100 mW. After obtaining the build-up data, the spectrum was fitted with a first order exponential using MATLAB® and **Equation 5.1**.

$$NMR\ Signal = A(1 - e^{\frac{t}{\tau}}) \qquad \text{Equation 5.1}$$

The build-up time constant, τ and maximum polarisation, A were calculated for each species **Figure 5.14** and **Table 5.10**.

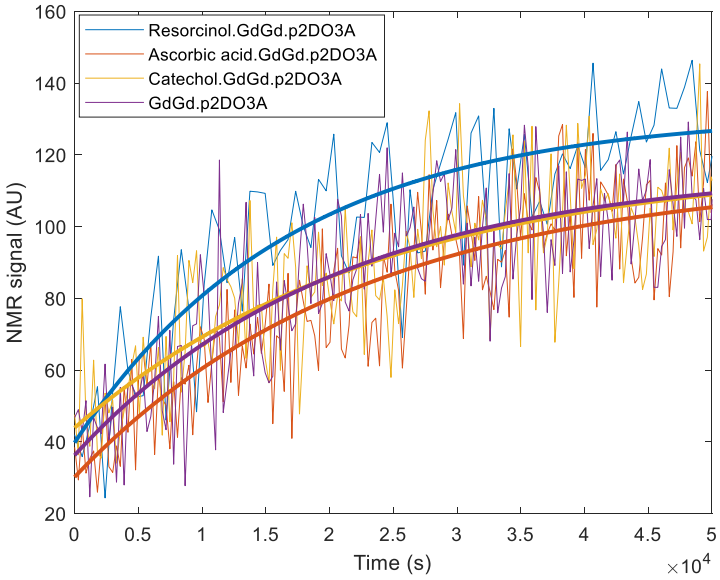

Figure 5.14: Fitting of hyperpolarisation build-up over time for different GdGd.p2DO3A species.

Table 5.10: Table indicating build-up time constants and maximum NMR signal for different GdGd.p2DO3A species.

Species	Build-up Time Constant (s)	Maximum NMR Signal (A.U.)
GdGd.p2DO3A	20611	80
Resorcinol.GdGd.p2DO3A	16883	92
Catechol.GdGd.p2DO3A	23959	74
Ascorbic Acid.GdGd.p2DO3A	225145	84

5.11 Discussion of ^{13}C Hyperpolarisation Results

The graph shows us that there is some potential for hyperpolarisation. The resorcinol.GdGd.p2DO3A gave us the best results in terms of having the shortest time constant, i.e. the quickest build-up, and the highest maximum NMR signal, i.e. the best polarisation. However, all the complexes as a whole gave very similar results which is

consistent with their EPR CW spectra being very similar. As previously discussed this could be because the ^{13}C-urea itself is binding to the complex or our ligands are making very little difference to the ligand field splitting as they do not have a sufficiently high enough binding constant.

The fact we are seeing the DNP effect with even the symmetric ligands and no ligand at all may be due to the fact that the cross effect can still occur as the two Gd(III) centres could be in different environments such as SAP or TSAP and their enantiomers frozen in solution at different times. For example one centre could be frozen as Δ-SAP and the other as Λ-TSAP and if we are to believe the results from mono analogue in **Chapter 4** this would put both in different environments with differing *g*-values.

The other issue is that these results do not compare favourably to the "gold standard" which is ^{13}C-pyruvate doped with OX063 and a small amount of Gd.DOTA^{-} (for which the time constant is about 2000 s and maximum build-up is about 20000 A.U). [9] **Figure 5.13**. This shows that whilst our complex has some potential and that DNP is occurring, there is a long way to go in terms of development before we reach similar values to that of the "gold-standard" for DNP.

5.12 Conclusions to Chapter

Overall, there is some potential for developing these complexes for application to DNP. In published work by Corzelius *et al.* other linear bis-Gd(III) complexes have undergone study and also have some potential for DNP NMR. [3] However, current results are not

as good as the “gold-standard” and these lack stability if the technique was to be translated for application *in vivo*. [8]

There are also issues that ^{13}C-pyruvate could not be used with our complexes as it bound to the complex and would not form a glass stopping the DNP mechanism from occurring. There are major issues generally that the species to be hyperpolarised will always be in excess which will potentially compete to bind to the hyperonization agent itself. This could stop potential ligands from binding which otherwise would have aided the cross effect mechanism.

5.13 References

[1] B. Corzilius, Phys. Chem. Chem. Phys., vol. 276, pp. 27190-27204, 2016.

[2] L. F. Pinto, I. Marin-Montesinos, J. L. Monez-Gomez, M. Pons, J. Veciana and J. Vidal-Gancedo, ChemComm, vol. 53, pp. 3757-3760, 2017.

[3] M. Kaushik, M. Qi, A. Godt and B. Corzilius, Angew. Chem., vol. 129, no. 15, pp. 4359-4363, 2017.

[4] A. Z. Lau, J. J. Miller, M. D. Robson and D. J. Tyler, Magn. Reson. Med., vol. 75, pp. 1474-1483, 2016.

[5] V. K. Michaelis, R. G. Griffin, B. Corzilius and S. Vega, High Field Dynamic Nuclear Polarisation, Chichester, West Sussex: Wiley, 2020.

[6] S. Stoll and A. Schweiger, J. Magn. Reson., vol. 178, pp. 42-55, 2006.

[7] B. Corzilius, A. A. Smith, A. B. Barnes, C. Luchinat, I. Bertini and R. G. Griffin, J. Am. Chem. Soc., vol. 133, pp. 5648-5651, 2011.

[8] K. R. Keshari and D. M. Wilson, Chem. Soc. Rev., vol. 43, no. 5, pp. 1627-1659, 2014.

[9] J. Miller , "DPhil Thesis," University of Oxford, 2014.

6 Conclusions and Future Work

6.1 Thesis Conclusions

The aim of this thesis was to develop new biomedical imaging applications for metallodrugs based on an improved understanding of their magnetic and electronic properties.

The thesis first set out to explore in detail how properties of metallodrugs can be varied based on their environment. It was shown in **Chapter 3** for a simple C_4 symmetric system containing a single isomer that ligand field splitting parameters could be greatly influenced by ligation. This finding is important for application to the development of new contrast media as these properties influence relaxivity. It was also shown that *g*-value could be greatly varied which in turn showed promise development for DNP MRI.

In **Chapter 4** and **Chapter 5** more complex systems were studied. In **Chapter 4** when studying systems with broken symmetry it was shown that SAP and TSAP had an influence over both the ligand field splitting parameters and *g*-value. Ligation was once again shown to also impact the form of EPR spectra and effect parameters accordingly as seen in **Chapter 3**. However, the fitting of the data proved to be different with the two models used to fit the data. An ideal was not found to model the data accurately which would have taken into account the variation in axial and equatorial binding of the ligand.

Chapter 5 was a complex system and large simplifications had to be made in order to fit the spectra. As the system studied was the same as that used to test application of the principles to DNP, the ^{13}C-urea was 6.0 M in the solution which may have proved problematic. The *D*, *E* and *g*-values were all very similar when modelling the data. Unlike the other complexes to be studied there was very little difference in the EPR spectra from species to species suggesting that the binding constants of our bridging ligands were weak. There also could have been competitive binding to the ^{13}C-urea itself. This presents a practical problem for application of these systems to DNP.

Application to DNP NMR was trialed to explore if there was variation in the different species including the asymmetric system involving ascorbic acid (vitamin C) as a bridging ligand. The DNP MRI studies showed that DNP was possible for these compounds and that the system had some potential. Unfortunately, there was very little difference in the build-up of NMR signal from species to species. This reinforced what the EPR demonstrated, that there was very little difference between the samples tested.

Overall, it has been demonstrated that based on our deeper understanding of the magnetic and electronic properties of our system we can apply our knowledge for use in applications such as DNP MRI and also potentially in the use of future development of contrast media.

6.2 Future Work

There is still much work to be done to improve our understanding of how exactly ligation effects ligand field splitting. We have seen a potential trend in the results given in **Chapter 3** but need further explanation of why this is the case i.e. is this due to proximity of the ligand to the Gd(III) centre or is it due to the amount whether the ligand is a weak or strong field ligand (π donor/acceptor) or is it a combination of the two factors. One way this could be explored is by computational modelling which is beyond the scope of this thesis.

Another piece of future work would involve a study of other lanthanide systems which again have varying amounts of SAP and TSAP to explore further how this effects ligand field splitting exactly and how the relative amounts of each effect the form of the spectra. It would be interesting to see if similar results were obtained across different Gd(III) species.

Finally, more exploration needs to be done into the potential application for DNP MRI. Different ligands with higher binding constants should potentially be trialed. However, this has already proved difficult due to solubility issues and issues with glassing at low temperature.

Another idea is to develop the bimetallic complex itself so that the each Gd(III) is surrounded by a different macrocycle and therefore the use of a bridging ligand is redundant **Figure 6.1**. However, the synthesis for these complexes would prove more challenging.

Overall, the project has great potential to be further developed and make considerable contributions to various areas of research within the field of medical imaging.

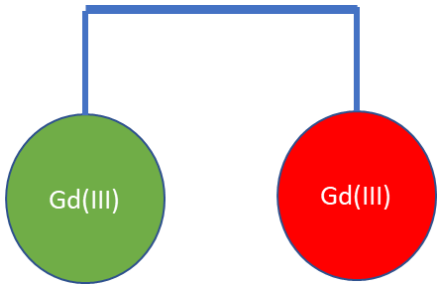

Figure 6.1: Schematic of a bis-Gd(III) complex with the Gd(III) ions in different environments due to different macrocycles being used.

7 Experimental

7.1 General Experimental Information

Commercially available solvents and reagents were used without further purification. All NMR spectra were recorded on a Bruker Avance III HD nanobay 400 MHz spectrometer. ^{1}H shifts are reported as chemical shifts (δ) in parts per million (ppm) relative to the residual undeuterated solvent peak using the Bruker internal referencing procedure (edlock). The following abbreviations are used to describe multiplicities s (singlet), br s (broad singlet), d (doublet), t (triplet), q (quartet), m (multiplet), br m (broad multiplet). Mass spectra were obtained using either Agilent Technology 1260 Infinity or a Waters LCT Premier XS. High resolution mass spectra were recorded on a Bruker μTOF mass spectrometer using positive electrospray ionisation. MALDI mass spectra were obtained on a Waters MALDI MicroMX spectrometer. Unless stated, all reactions were performed in oven-dried apparatus with magnetic stirring. Thin-layer chromatography (TLC) were performed using Merck aluminium-foil backed plates pre-coated with Kieselgel 60 K_{245}. The products were visualised using UV fluorescence (254 nm) or potassium permanganate stain. Silica gel column chromatography was performed over Merck silica gel C60 (40-60 μm) using eluent systems as described in each experimental procedure. Anhydrous solvents were obtained from an MBraun MB SPS-800. All UV/Vis spectra was obtained on a T60U Spectrophotometer, PG Instruments LTD. All luminescence

data for lanthanide compounds was obtained on a Horiba Fluorolog 3. Known compounds have been checked against literature references.

7.2 Characterisation of Compounds

2,2',2'',2'''-(1,4,7,10-tetraazacyclododecane-1,4,7,10-tetrayl)tetrakis(N-phenylacetamide) [1]

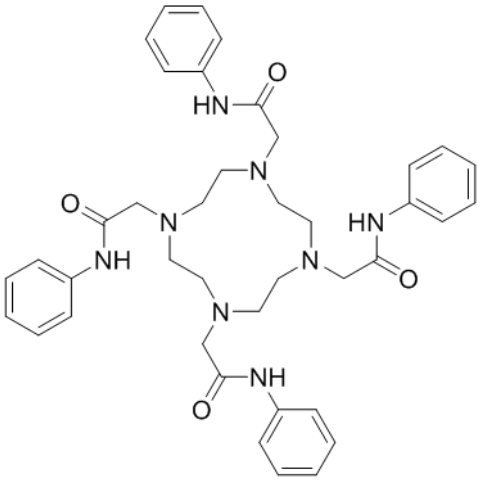

A mixture of cyclen (104 mg, 0.6 mmol, 1 Eq) and N-(phenyl)bromoactamide (513.8 mg, 2.4 mmol, 4 Eq) were stirred at room temperature in THF (10 mL). TEA (418 µL, 3 mmol, 5 Eq) was added dropwise. On completion of the addition, the reaction mixture was heated to reflux for 20 hours. The reaction mixture was concentrated i*n vacuo* and then portioned between 100 mL of water and 100 mL of DCM. The organic phase was concentrated and the remaining solid recrystallized using hot DMF. After drying using high vacuum the product afforded a white solid (88 mg, 0.12 mmol, 21 % yield). **^{1}H NMR (400 MHz, $CDCl_3$):** 2.83 (m, 16 H), 3.19 (s, 8H), 6.95-7.50 (br m, 20H), 8.79 (br s, 4H). **LRMS (ESI):** m/z $[M+H]^+$ required 705.4, found 705.4.

Gd.DOTAMPh [1]

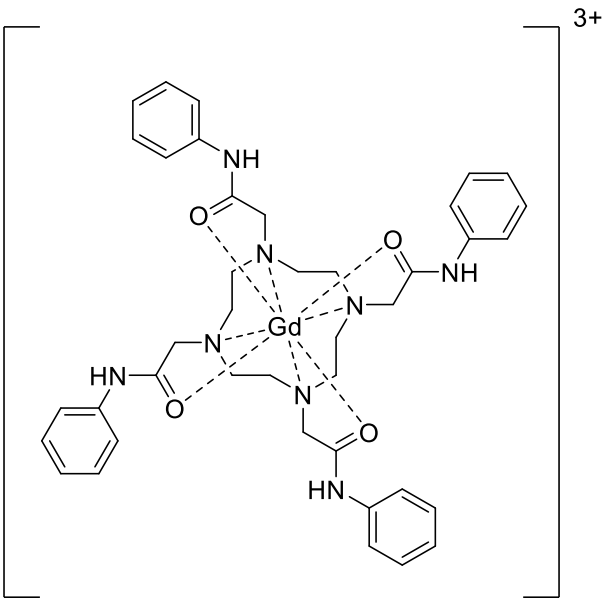

$Gd(OTf)_3$ (39.3 mg, 0.125 mmol, 1 Eq) and DOTAMPh (88 mg, 0.125 mmol, 1 Eq) were stirred for 30 minutes at 60 ° C. 1 M NaOH was then added dropwise until a pH of 4 was reached. The reaction mixture was stirred at 60 ° C for 3 days with the pH regularly monitored to make sure it remained at about pH 4. The reaction was then cooled and the pH adjusted to 7 before the solvent was removed *in vacuo*. The crude product was then dissolved in 2 mL of distilled water and purified by an Amberlite XAD16N column. The product afforded an orange solid (224 mg, 0.26 mmol, 50 % yield). **LRMS (ESI):** m/z [M+H]+ required 862.3, found 862.3.

Eu.DOTAMPh [1]

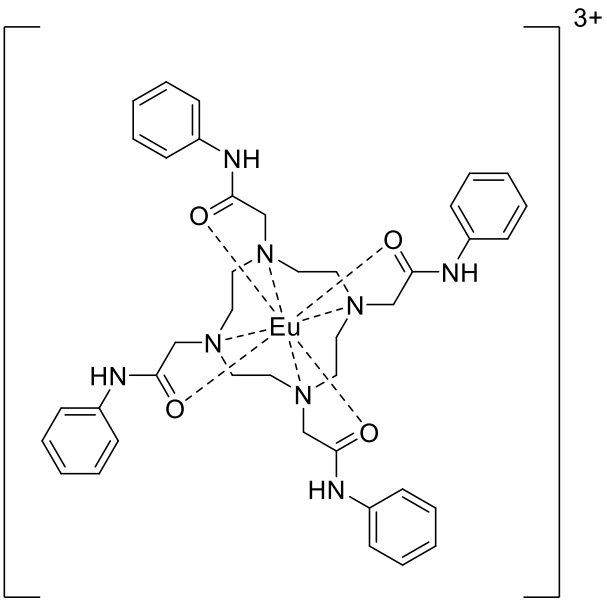

$Eu(OTf)_3$ (74.9 mg, 0.125 mmol, 1 Eq) and DOTAMPh (88 mg, 0.125 mmol, 1 Eq) where stirred for 30 minutes at 60 ° C. 1 M NaOH was then added dropwise until a pH of 4 was reached. The reaction stirred at 60 ° C for 3 days with the pH regularly monitored to make sure it remained at about pH 4. The reaction was then cooled and the pH adjusted to 7 before the solvent was removed i*n vacuo*. The crude product was then dissolved in 2 mL of distilled water and purified by an Amberlite XAD16N column. The product afforded an orange solid (222.8 mg, 0.26 mmol, 50 % yield). **^{1}H NMR (400 MHz, CD_3CN):** 20.26 (s), 7.75 (s), 7.45 (s), 7.10 (s), -3.04 (s), -5.32 (s), -6.06 (s), -8.30 (s), -9.96 (s). Only peaks that can be resolved are recorded. **LRMS (ESI):** m/z $[M+H]^+$ required 857.3, found 857.4.

Triester: Tri-*tert*-butyl 2,2',2''-(1,4,7,10-tetraazacyclododecane-1,4,7-triyl)triacetate [2]

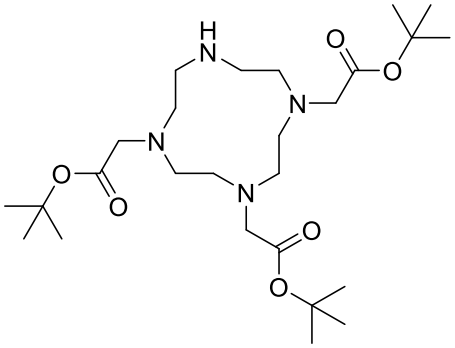

Sodium bicarbonate (9.66 g, 115 mmol, 3.3 Eq.) and cyclen (6.00 g, 38.4 mmol, 1 Eq.) were allowed to stir in anhydrous acetonitrile (210 mL) for 30 minutes at 20 ° C. The reaction was cooled to 0 °C before addition of tert-butyl bromoacetate (115 mL of 1 M in anhydrous acetonitrile, 115 mmol, 3.3 Eq.) dropwise over 30 minutes. The ice bath was removed and the reaction left to stir at 20 ° C for 2 days. The reaction was filtered using filter paper and the filtrate collected before being concentrated *in vacuo*. The crude product was recrystallized using toluene. The recrystallization afforded a white solid (9.68 g, 18.8 mmol, 49 % yield). **^{1}H NMR (400 MHz, $CDCl_3$):** δ = 1.45 (s, 9H), 1.47 (s, 18H), 2.88 (m, 4H), 2.93 (m, 8H), 3.11 (m, 4H), 3.30 (s, 2H), 3.38 (s, 4H), 10.04 (br s, 2H); **^{13}C NMR (100 MHz, $CDCl_3$):** δ = 28.1, 28.2, 47.5, 48.8, 49.2, 51.3, 51.4, 58.2, 81.7, 81.8, 169.6, 170.5.

tri-tert-butyl 2,2',2''-(10-(prop-2-yn-1-yl)-1,4,7,10-tetraazacyclododecane-1,4,7-triyl)triacetate [3]

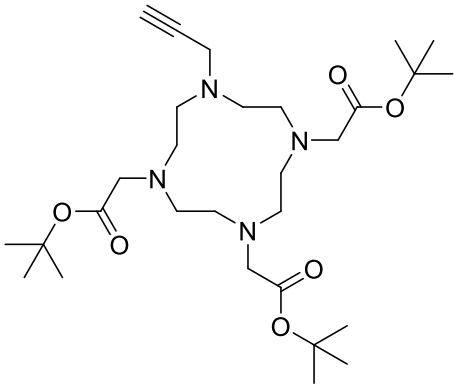

Triester (1.00 g, 1.95 mmol, 1 Eq.) was allowed to dissolve in 20 ml anhydrous MeCN. Caesium carbonate (667.0 mg, 3.90 mmol, 2 Eq.) was added and the resulting mixture was allowed to stir for 20 mins at 0 ° C. Propargyl bromide was added dropwise and the resulting mixture was left to stir for 24 hours under nitrogen. The resulting mixture was concentrated *in vacuo* and then dissolved in toluene. This was then washed 3 times with water, dried with magnesium sulfate and concentrated *in vacuo*. This afforded an orange oil (584 mg, 1.04 mmol, 53 % yield). **^{1}H NMR (400 MHz, $CDCl_3$):** δ = 1.38 (s, 27 H), 2.07 (t, 1H, *J* = 2.3 Hz), 2.58-2.76 (m, 16H), 3.22 (s, 6H), 3.37 (d, 2H, *J* = 2.3 Hz). **LRMS (ESI):** m/z $[M+H]^+$ required 553.4, found 553.4.

pDO3A: tri-tert-butyl 2,2',2''-(10-(prop-2-yn-1-yl)-1,4,7,10-tetraazacyclododecane-1,4,7-triyl)triacetate [3]

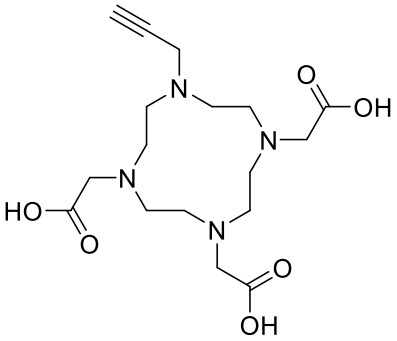

tri-tert-butyl 2,2',2''-(10-(prop-2-yn-1-yl)-1,4,7,10-tetraazacyclododecane-1,4,7-triyl)triacetate (558 mg, 1.04 mmol, 1 Eq) was stirred with 5 ml TFA in 5 mL DCM for 1 day at room temperature. The solvent was removed *in vacuo*. 10 ml methanol was added and then removed *in vacuo*. This was repeated an additional 5 times to ensure removal of TFA. The product afforded a white solid in quantitative yield. **^{1}H NMR (400 MHz, D_2O):** 2.77 (br s, 1H), 3.18 (br s, 8H), 3.33-3.44 (m, 8H), 3.61 (s, 2H), 3.85 (m, 6H). **LRMS (ESI):** m/z $[M+H]^+$ required 385.2, found 385.2.

Eu.pDO3A [3]

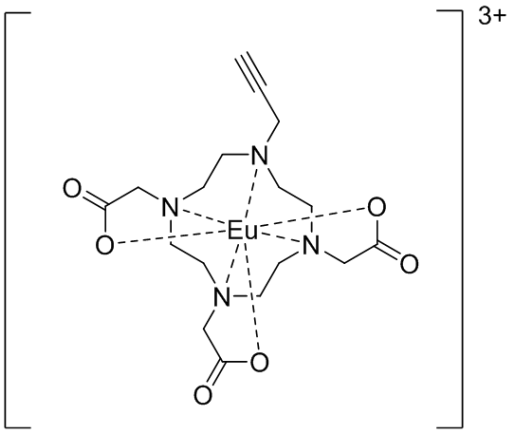

$Eu(OTf)_3$ (311.6 mg, 0.52 mmol, 1 Eq) and pDO3A (192.6 mg, 0.52 mmol, 1 Eq) were stirred for 30 minutes at 60 ° C. 1 M NaOH was then added dropwise until a pH of 4 was reached. The reaction stirred at 60 ° C for 3 days with the pH regularly monitored to make sure it remained at about pH 4. The reaction was then cooled and the pH adjusted to 7 before the solvent was removed *in vacuo*. The crude product was then dissolved in 2 ml of distilled water and purified by an Amberlite XAD16N column. The product afforded an orange solid (140 mg, 0.26 mmol, 50 % yield). **^{1}H NMR (400 MHz, D_2O):** 26.67 (s), 18.61 (s), 15.67 (s), 10.26 (s), 3.24 (s), 0.99 (s) -1.96 (s), -5.98 (s), -9.12 (s), -10.32(s), -11.25 (s), -12.16 (s), -13.76 (s), -15.28 (s), -16.26 (s), -19.42 (s). Only peaks that can be resolved are recorded. **LRMS (ESI):** m/z $[M+H]^+$ required 535.1, found 535.8.

Gd.pDO3A [3]

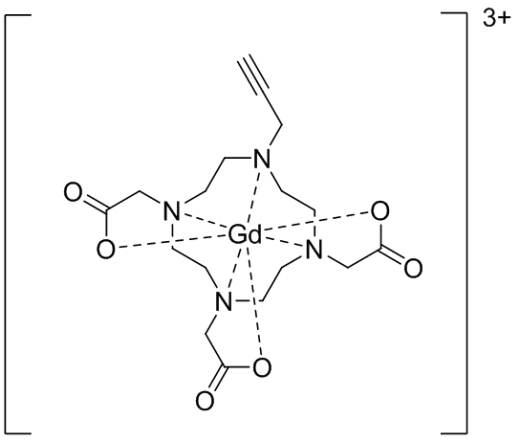

$Gd(OTf)_3$ (314.3 mg, 0.52 mmol, 1 Eq) and pDO3A (192.6 mg, 0.52 mmol, 1 Eq) were stirred for 30 minutes at 60 ° C. 1 M NaOH was then added dropwise until a pH of 4 was reached. The reaction stirred at 60 ° C for 3 days with the pH regularly monitored to make sure it remained at about pH 4. The reaction was then cooled and the pH adjusted to 7 before the solvent was removed *in vacuo*. The crude product was then dissolved in 2 ml of distilled water and purified by an Amberlite XAD16N column. The product afforded an orange solid (121.0 mg, 0.22 mmol, 43 % yield). **LRMS (ESI):** m/z $[M+H]^+$ required 540.1, found 540.8.

1,4-bis-(Tri-*tert*-butyl 2,2',2''-(1,4,7,10-tetraazacyclododecane-1,4,7-triyl)triacetate)- but-2-yne. [4]

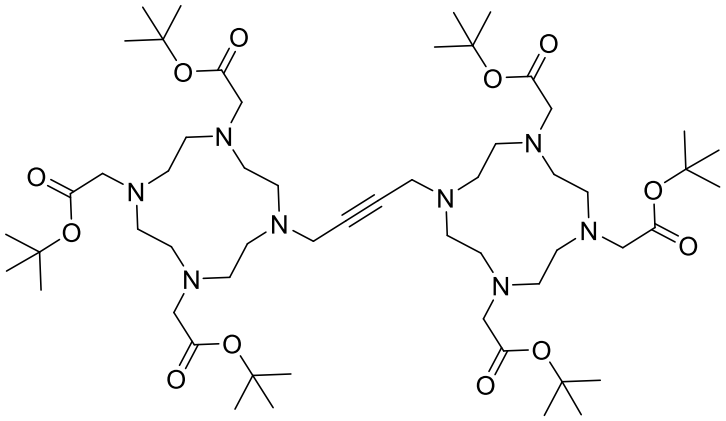

Anhydrous MeCN (60 ml), triester (1.029 g, 2 mmol, 2 Eq.) and caesium carbonate (1.63 g, 4 mmol, 2 Eq.) were left to stir for 30 minutes at 20 ° C. 1,4-dichlorobut-2-yne was added dropwise (100 µl, 1 mmol, 1 Eq.) and the resulting mixture left to stir for 2 days. The caesium carbonate was filtered off and the remaining solution concentrated *in vacuo*. The crude product was purified using alumina flash chromatography where the alumina was soaked in DCM overnight before use. The eluent was 95:5 DCM:MeOH and afforded a pale yellow solid (253 mg, 0.24 mmol, 12 % yield). **^{1}H NMR (400 MHz, $CDCl_3$):** 0.85 (br s, 1H), 1.23 m (m, 7H), 1.45 (m, 44H), 1.81 (s, 10H), 2.23 (br s, 6H), 2.66 (s, 2H), 2.77 (s, 3H), 3.04 (s, 2H), 3.17 (s, 2H), 3.29 (br s, 2H), 3.37 (s, 2H), 3.43 (s, 1H), 3.48 (s, 16H) 3.83 (s, 2H), 4.06 (s, 2H), 4.78 (s, 2H). **LRMS (ESI):** m/z $[M+H]^+$ required 1080.8, found 1081.1.

p2DO3A: 1,4-bis-((1,4,7,10-tetraazacyclododecane-1,4,7-triyl)(triacetatic acid))- but-2-yne. [4]

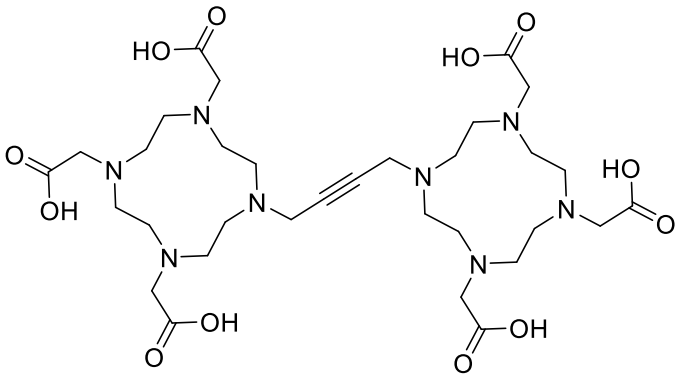

1,4-bis-(tri-tert-butyl 2,2',2"-(1,4,7,10-tetraazacyclododecane-1,4,7-triyl)triacetate)- but-2-yne (446 mg, 0.413 mmol, 1 Eq.) was stirred in 5 ml DCM at 20 ° C and 5 ml of TFA was added dropwise. The resulting solution was stirred for 2 days under nitrogen before being concentrated *in vacuo*. What remained was dissolved in minimum amount of methanol before being triturated using ether. This was repeated and the solid was then dissolved in 2 ml of water before being freeze dried. Chloroform was then added and the mixture was thoroughly stirred before filtering. This afforded the pure product as a pale pink solid (90 mg, 0.12 mmol, 29 %). **^{1}H NMR (400 MHz, D_2O):** 3.78-3.91 (br m, 12 H), 3.67 (br s, 4 H), 3.22-3.36 (m, 32H). **LRMS (ESI):** m/z $[M+H]^+$ required 744.3, found 744.3.

EuEu.p2DO3A [5, 4]

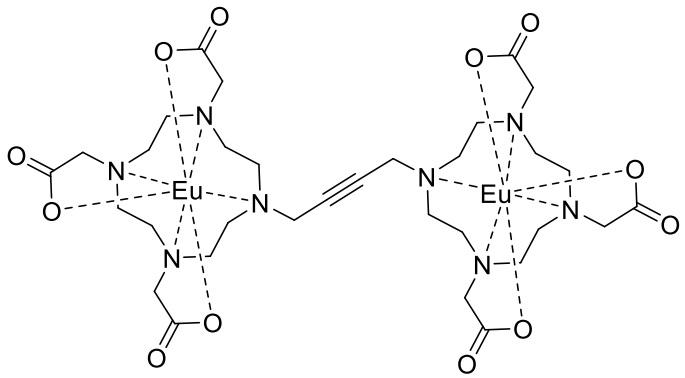

$Eu(OTf)_3$ (41.9 mg, 0.082 mmol, 2 Eq) and p2DO3A (30 mg, 0.041 mmol, 1 Eq) were stirred for 30 minutes at 60 ° C. 1 M NaOH was then added dropwise until a pH of 4 was reached. The reaction stirred at 60 ° C for 3 days with the pH regularly monitored to make sure it remained at about pH 4. The reaction was then cooled and the pH adjusted to 7 before the solvent was removed *in vacuo*. The crude product was then dissolved in 2 ml of distilled water and purified by an Amberlite XAD16N column. The product afforded an pale orange solid (5.0 mg, 0.005 mmol, 12 % yield). **^{1}H NMR (400 MHz, D_2O):** 23.54, 16.88, 14.18, 11.73, -3.41, -5.48, -6.23, - 8.66, -9.04, -10.70, -10.97, -11.97, -12.29, -14.04, -15.38, -17.21, -19.78 ppm. Only peaks that can be resolved are recorded. **LCMS:** m/z $[M+H]^+$ expected: 1040.180, found: 1040.474, t_R = 0.529 min.

GdGd.p2DO3A [5, 4]

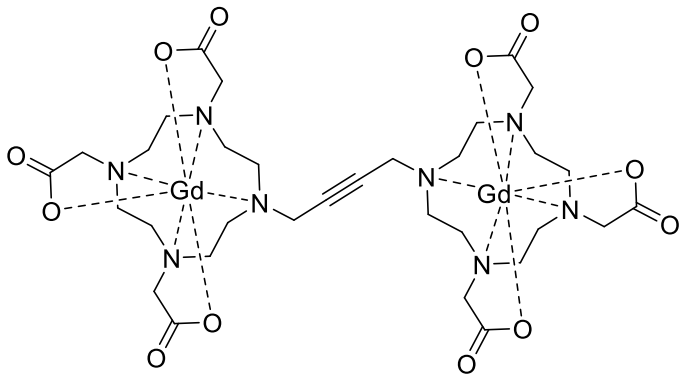

$Gd(OTf)_3$ (49.6 mg, 0.082 mmol, 2 Eq) and p2DO3A (30 mg, 0.041 mmol, 1 Eq) were stirred for 30 minutes at 60 ° C. 1 M NaOH was then added dropwise until a pH of 4 was reached. The reaction stirred at 60 ° C for 3 days with the pH regularly monitored to make sure it remained at about pH 4. The reaction was then cooled and the pH adjusted to 7 before the solvent was removed *in vacuo*. The crude product was then dissolved in 2 ml of distilled water and purified by an Amberlite XAD16N column. The product afforded a white solid (25 mg, 0.023 mmol, 58 % yield). **MALDI-MS:** (α – Dithranol) m/z $[M+H]^+$ required: 1053.196, found: 1053.583.

Amberlite XAD16N

Complexes were desalted on an Amberlite XAD16N column. Amberlite was soaked in water for 10 min, then in MeCN for 10 min. The column was loaded in MeCN and left to settle for a minimum of 30 min, before washing through with water three times the columns volume. The complex was then loaded in water (0.1 mg mL^{-1}). The column was washed multiple times with water (approx. 1 L), and the water tested with Xylenol orange until it was clear for Gd(III). The product was then eluted with 10 - 20 % MeCN.

Xylenol Orange Test

Xylenol Orange was prepared and used in accordance with previous reports. [6] 50 mM acetate buffer at pH 5.8 is prepared by diluting acetic acid (2.87 mL, mmol) in 800 mL water. The pH is adjusted to 5.8 with 1 M NaOH and the buffer made up to 1 L with water. Xylenol Orange (3 mg, 4.5 μmol) is dissolved in 250 mL acetate buffer to give an 18 μM solution. Aliquots of the solution were frozen immediately for storage and defrosted for use as required. Gd(III) complexes were tested for free Gd(III) as follows: 10 μL of 11 mM Gd(III) complex was added to 100 μL xylenol orange solution to give a final concentration of 1 mM Gd(III) complex, and the results determined by eye.

7.3 Luminescence Titration

7.3.1 Methodology of Titrations

Stock solutions of the lanthanide complex in deionised water were made prior to the titration experiments, and a separate concentrated stock solution of the ligand. To form the titrant solution an aliquot of the anion solution was added to stock solution to yield a concentration at least 100 times that of the complex. Both the stock solution and the titrant solution were diluted to the final concentration with deionised water, to give equivalent concentrations of the complex and prevent dilution during the titration. The stock solution of complex (2 mL) was added to a quartz fluorescence cuvette and small increments of the titrant added with the emission spectra recorded at each point.

7.3.2 Dynafit® Scripting

The integrals of the peak intensity were calculated for the $\Delta J = 1$ (560–600 nm) and $\Delta J = 2$ (600–640 nm) transition, as a function of increasing benzylamine concentration. These values were globally fitted using Dynafit® software and associated binding constant determined. [7]

7.3.3 Example of Dynafit Script

```
[task]
  task = fit  ;
  data = equilibria  ;
[mechanism]
  Eu + Benzylamine <==> complex1 : K1 assoc
[constants]
  K1 =  500000??
[concentrations]
  Eu = 0.0000002
[responses]
  intensive
[data]
```

variable Benzylamine

file
C:\Users\SFGroup\Desktop\Katie_Fisher\KATIE_FISHER_TRANSFERED_FILES\Titrations\trial1J2pdo3a.txt | response Eu = 5000000?, complex1 = 0.00000003? ;

[output]

directory
C:\Users\SFGroup\Desktop\Katie_Fisher\KATIE_FISHER_TRANSFERED_FILES\Titrations\pDO3A

[end]

7.4 References

[1] V. Lagostina, L. Leone, F. Carniato, G. Digilio, L. Tei and M. Botta, *Inorganics*, vol. 7, pp. 43, 2019.

[2] M. Jauregui, W. S. Perry, C. Allain, L. R. Vidler, M. C. Willis, A. M. Kenwright, J. S. Snaith, G. J. Stasiuk, M. P. Lowe and S. Faulkner, *Dalton Trans,* vol. 0, pp. 6283-6285, 2009.

[3] L. Tear, "DPhil Thesis," University of Oxford, 2018.

[4] G. M. O'Maille, "Personnal communication," University of Oxford, 2015.

[5] A. Barge, G. Cravotto, E. Gianolio and F. Fedeli, *Contrast Media Mol. Imaging,* vol. 1, pp. 184-188, 2006.

[6] P. Kuzmic, *Methods Enzymol.*, vol. 467, pp. 247-280, 2009.